Università
Ca’Foscari
Venezia

Master’s Degree

in Science and Technology of Bio and Nanomaterials

Final Thesis

Biomorphous porous oxide ceramics, A review

Supervisors
Prof. Claudia Crestini
Prof. Robert C. Pullar

Graduand
Davide Redolfi Bristol
Matricolation number
856842

Academic Year
2019 / 2020

INDEX

1. Introduction

Porous ceramics are an interesting class of materials which gained increasing attention since the beginning of the 1970s. They are composed of heat-resistant materials, usually metal oxides, with porosity that ranges from 20% to 95%, of their total volume. Porous ceramics are usually divided in two groups: foam ceramics and reticulate ceramics (Figure 1). [1] The former ones are generally produced through a blowing process in which foaming agent creates bubbles that, during the subsequent calcination step, will lead to the formation of closed and open pores within the continuous ceramic matrix. The second ones are usually obtained after infiltration and condensation of the precursor material on a porous sacrificial template, followed by heat treatments to create the final reticular (net-like) ceramic structure. The template, often a polymer, burns out during heating, leaving a ceramic with the same form. The obtained material presents a unique 3D structure in which open pores are highly connected and arranged in all directions. [2]

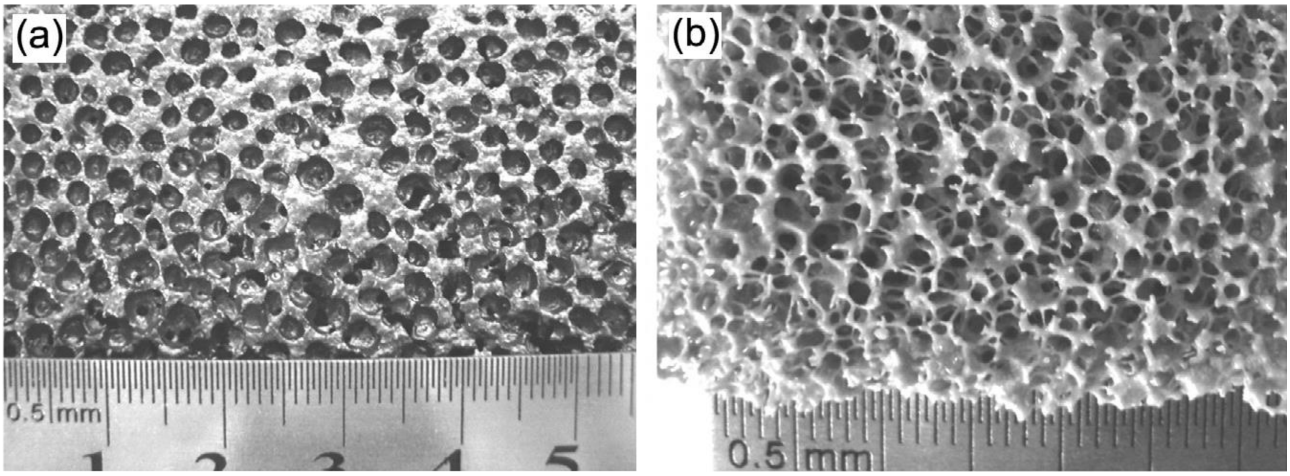

Figure 1 *– Comparison images between a) foam ceramic and b) reticulate ceramic [1]*

Properties such as low density, low weight, low thermal conductivity, high surface area, high gas permeability, and high temperature and chemical stability depend upon the chemical composition and porosity of the ceramic, and make them widely investigated for applications such as filtration, light-weight structural materials, absorption, thermally insulating materials, sensors, membrane supports, catalyst carriers, bioscaffolds in the biomedical field, etc. [3-5] In particular, the pore characteristics play a key role in the final behaviour of the manufactured object and, consequently, on its applications. For example, while micro- (<2 nm) and meso- (2–50 nm) pores generally provide high surface area and, therefore, determine the related performance of the material, pores larger than 50 nm are able to enhance properties like mass and heat transfer. Graded porosity and large interconnection are desired when the component needs to be used as bioscaffold, to improve cell seeding and subsequent cell growth, biological cells requiring macropores of >100 μm to proliferate. [6]. As a result, the research of new manufacturing techniques and the study of the products that can be obtained are of great importance for widening the fields of application of these materials.

Highly porous ceramics have found interesting applications in several industrial fields, directing the researchers' attention towards identification and development of innovative processing routes that would enable their production, with larger ranges of morphologies and characteristics. Indeed, synthetic strategies with well-defined and diversified pathways play one of the main roles for the production of porous ceramic elements, and thus innovation in this area is always required. [2]

In recent years, the development of novel ceramic structures by mimicking the cellular anatomy of natural lignocellulosic forms has gained increasing interest. The highly anisotropic structural composition of lignocellulosic biomass could serve as a hierarchical template to design innovative ceramics with a macro, meso- and micro-structure comparable to the initial porous skeleton, ranging from millimeters to nanometers. [7] These innovative types of ceramics are generally referred as environmentally conscious ceramics or ecoceramics, and possess peculiar characteristics which differentiate them from the common ceramic materials obtained with the usual production techniques. To be truly sustainable ecoceramics, their biomass source should also be sustainable, e.g. agricultural or forestry wastes, sawdust, etc.

Until now, large efforts have been performed in the fabrication of biomimetic carbide ceramics, such as SiC, TiC and ZrC, exploiting pyrolysis and infiltration of silicon/metallic precursors into carbon templates. [8] Several reviews and articles about the production of these materials using various synthetic approaches and different wood templates have been published, also thanks to the promising applications that they can show in aeronautics, electronic, thermal, and transportation industries. [9-25] Less attention, however, has been paid to biomorphous oxide ceramics (such as TiO_2, Al_2O_3, CeO_2 etc.) and, above all, no review has ever been dedicated to their total description.

In this work the state of the art of biomimetic oxide ceramics will be presented, focusing the attention on their production using lignocellulosic materials as starting templates. Further, applications of the materials obtained will be discussed, and possible new investigation areas will be considered.

2. Lignocellulosic biomass

Lignocellulose, also called lignocellulosic biomass, refers to dry plant matter which can be obtained from trees, bushes and agricultural crops (Figure 2). It is formed by plants through the conversion of carbon dioxide to an organic mass mainly composed of elements like C, O, H and N. Being the main non-food component of biomass, it represents an almost unlimited source of carbon that does not interfere with food demand; moreover, because of its great abundance, it has a very low market price and is considered as the most important carbon supply on the planet. [26]

Among the various resources that can be exploited as organic biomass, wood and its derivatives are one of the most important components. Wood has been used by humans for thousands of years as tools, weapons, structures and many other applications. Nowadays, increase in the demand for energy and the continuous decrease in fossil carbon reserves has led researchers to focus their attention on the use of wood and plant biomass as a potential replacement for fossil resources for energy production. [27] Besides its useful application as possible fuel, wood possesses other interesting characteristics that make it suitable in several industrial fields. Two of these features are the hierarchic porous morphology of its internal structure, and the diversified arrangement of the inner pores which make it a suitable biotemplating material for the preparation of products with greater added value. The porous cells in wood, used for the transport of fluids within the plant, are often in a highly regular, 3-DOM (3-dimensionally ordred macroporous) structure. The words biomorphic and biomimetic are used interchangeably to describe such biotemplated materials.

Another lignocellulosic biomass fraction which shows the possibility to be used as a biomimicking structure are green leaves. Natural leaves are the important component of trees and bushes developed to convert light through the photosynthesis process into chemical compounds, necessary for the survival of virtually all higher life-forms. To enhance photosynthesis, the hierarchical structure of green leaves has been perfected by nature as an optimal machine for light harvesting. Several plant species present peculiar cells capable of acting as lenses, focusing the light on the leaf’s inner parts through a refraction mechanism, and creating spots in which irradiation is considerably higher than those present under the ambient light environment. Moreover, the microscopic composition of veins and inlets in leaves causes the phenomenon of internal light scattering to trap light inside the structure, enhancing light harvesting and photosynthesis. Exploiting the complex architecture of green leaves as template, it could be possible to create efficient light collecting materials that could be used in photochemical energy production. [28]

A further interesting component which belongs to lignocellulosic biomass is natural fibers such as hemp, sisal, bamboo and many others. Natural fibers are gaining attention each year due to their low cost and characteristic of being an optimal renewable resource. Even for fibers, several studies have been performed on their use as templates to produce inorganic 2D materials such as porous metal oxides. For example, jute has been exploited for the creation of biomorphic TiO_2 fibers with increased photocatalytic activity as compared to commercially available photocatalysts. [29, 30]

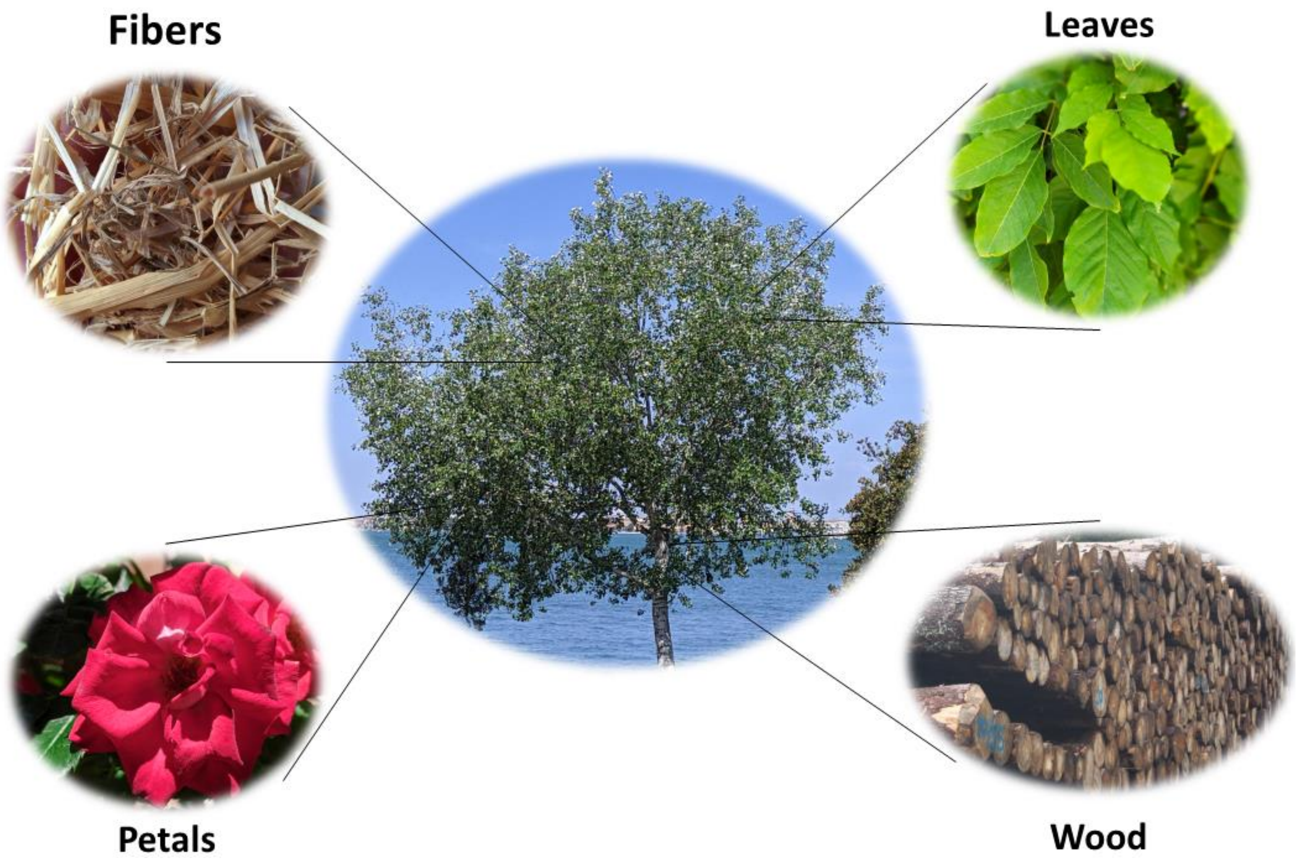

Figure 2 *– Some components of the lignocellulosic biomass*

2.1 Characteristics of wood and its derivatives

2.1.1 Chemical composition of wood

Dry wood is a mixture of components, mainly made up of three different fractions (Figure 3): cellulose (about 30-50% by weight), hemicellulose (20-40% by weight) and lignin (15-25% by weight).

Cellulose is a long-chain, non-branched homopolymer made up of β-D-glucose units linked by β-1,4-glycosidic bonds. It is linear and contains amorphous and crystalline portions, with large networks of intramolecular and intermolecular hydrogen bonds, thanks to the presence of three free hydroxyl groups on each monomeric unit. Because of this hydrogen bond network, and due to the restricted rotation around the polymeric 1,4-β-linkage, polymer chains are generally arranged parallel to each other forming crystalline structures which are very long and difficult to dissolve, called microfibrils. As a consequence, cellulose is not digestible by humans, due to the absence of enzymes suitable for the hydrolysis of the β-1,4-glycosidic bonds.

Hemicellulose is a highly branched heteropolymer of pentose sugars (xylose and arabinose), hexose sugars (glucose, galactose and mannose) or small quantities of other saccharides. Its average degree of polymerization is much lower than cellulose, but its morphological structure is vastly different. [31]

Lignin is the most complex fraction of wood biomass. It is an amorphous and highly irregular aromatic polymer consisting of phenylpropanol units, this making it one of the few renewable resources from which to draw to obtain aromatic compounds. Lignin is placed inside the cell wall where it fills the empty spaces left by the network of threads formed by cellulose and hemicellulose, giving rigidity to the wall. This structure makes cellulose and hemicellulose poorly accessible, unless a specific chemical or physical pre-treatment for its removal is implemented. Unlike cellulose and hemicellulose, lignin cannot be hydrolysed in its structural units, which makes it more difficult to process, but it is an interesting raw material for many other purposes such as chemical extraction or energy generation. For many years lignin has found application in the pulp and paper industry as solid fuel, providing energy during operation of paper mills, thanks to its excellent calorific value, higher even than that of wood. However, new technologies have shown that its depolymerization can generate precious aromatic compounds, such as vanillin (used in the confectionery sector), or important precursors for the synthesis of monomeric or oligomeric products useful as starting chemicals for further processes in industrial field. [32]

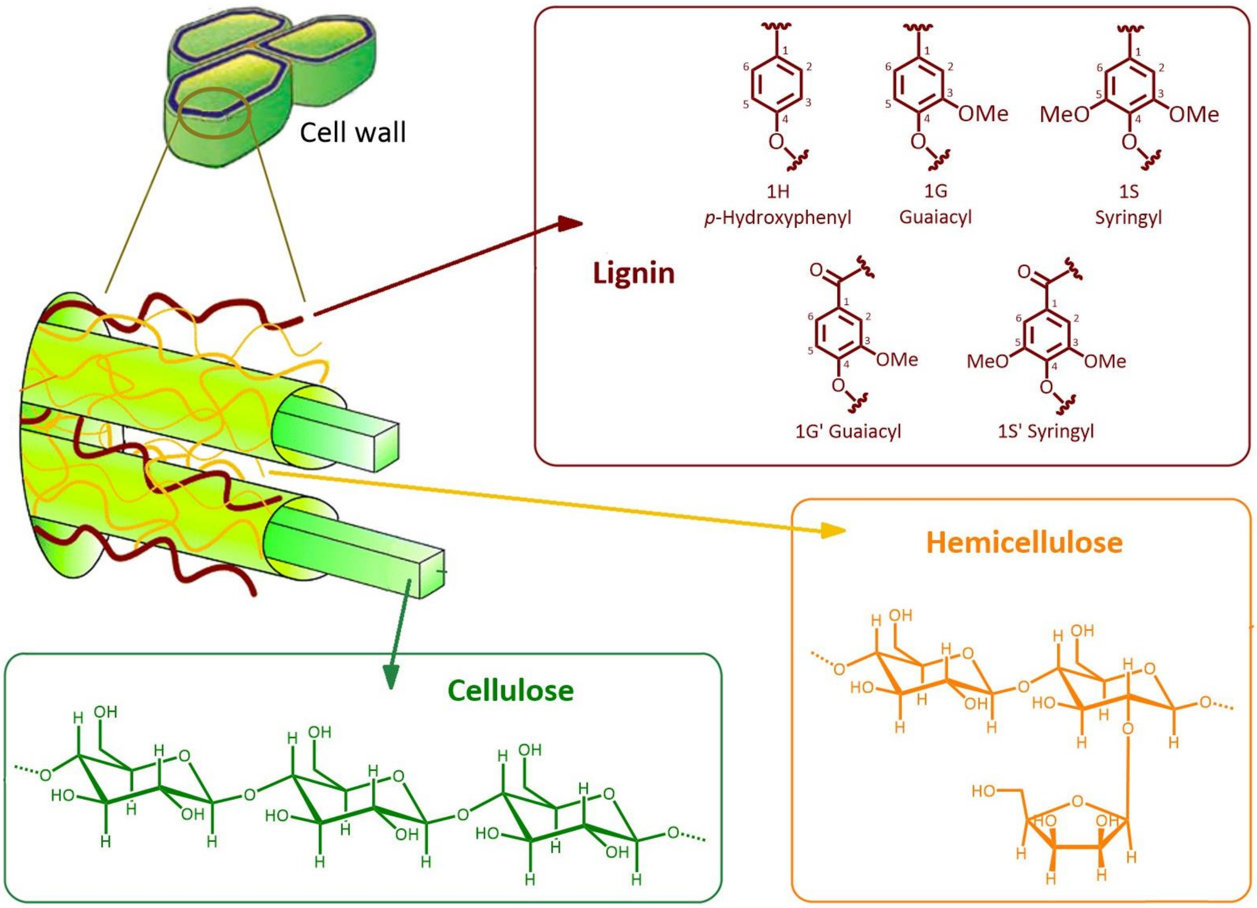

Figure 3 *– Schematic illustration of chemical composition of lignocellulosic biomass with representation of most important repeating units of lignin. Modified image from ref. [33]*

2.1.2 Anatomy of wood

Wood is a natural grown composite with a complex hierarchical cellular structure perfected by time and evolution. It is the component of trees which provides mechanical strength, as well as liquid transport and nutrition storage. [34] The wood cell wall is composed usually of three concentric layers (middle lamella, primary cell wall and secondary cell wall) surrounding an empty porous space called lumen (Figure 4). [4] The middle lamella is the thin external component which contains the highest concentration of lignin and connects the wood cells. The primary cell wall is the subsequent layer composed mainly of cellulose, hemicellulose and pectin. [35] Finally, the secondary cell wall is the most internal part, and can be further divided into three sections (S_1, S_2, S_3) based on the composition and arrangement of the biopolymers present. Generally, the S_1 layer has the highest concentration of lignin, while S_3 has the lowest. The S_2 layer, besides being the thickest fraction, possess the largest amount of cellulose and hemicellulose. In the secondary cell wall, cellulose chains are linked together by hydrogen bonds to form parallel sheets that create the microfibril structure. [36]

While the chemical composition of the cell wall is relatively consistent, anatomical differences in overall cellular structure between different kinds of wood can be very large. The constituent basic blocks of wood are tubular structures aligned in the direction of the growth of the tree, and from their characteristics and location it is possible to distinguish two categories of wood: hardwoods, which come from angiosperm trees which lose their leaves annually, and softwoods, which come from gymnosperm trees (usually evergreen conifers).

Apart from sharing the presence of hierarchical elongated tubular cells aligned with the axis of the tree trunk, hardwoods present vessel elements, also called “pores”, which are absent in softwoods (Figure 4). These vessels’ shape can vary from circular to ellipsoidal, and they can be present as solitary pores or be disposed in chains, clusters, or multiples. A chain-like structure is made of adjacent solitary pores arranged in a line, while clusters are formed by an irregular disposition of neighbouring pores. Multiples are somewhere in between chain and clusters - in fact, they are composed of adjoining pores but flattened along the lines of contact, thus appearing as subdivisions of a single large pore. The size of vessel members varies widely among species and inside a single tree. They tend to be short with length that ranges between 0.2 and 1.3 mm, with a diameter spanning from 0.005 to 0.5 mm.

Other cell types in hardwoods differ from softwoods, in particular: ray parenchyma (small, thin-walled storage and food transport cells), axial parenchyma (food storage cells elongated vertically the tree stem) and fibers. These latter cells have the function of providing mechanical support to the living tree; however, they may also participate in transport. Fibers are long narrow cells with lengths of 1–2 mm and diameters of 0.01–0.05 mm. They have closed ends, mostly pointed, but sometimes equipped with dentations. The fiber walls may be thick or thin and lumen narrow or large. These differences in morphology, size and distribution vary significantly among species of wood, as well as among trees of a given species and age and within a single tree. [7, 37]

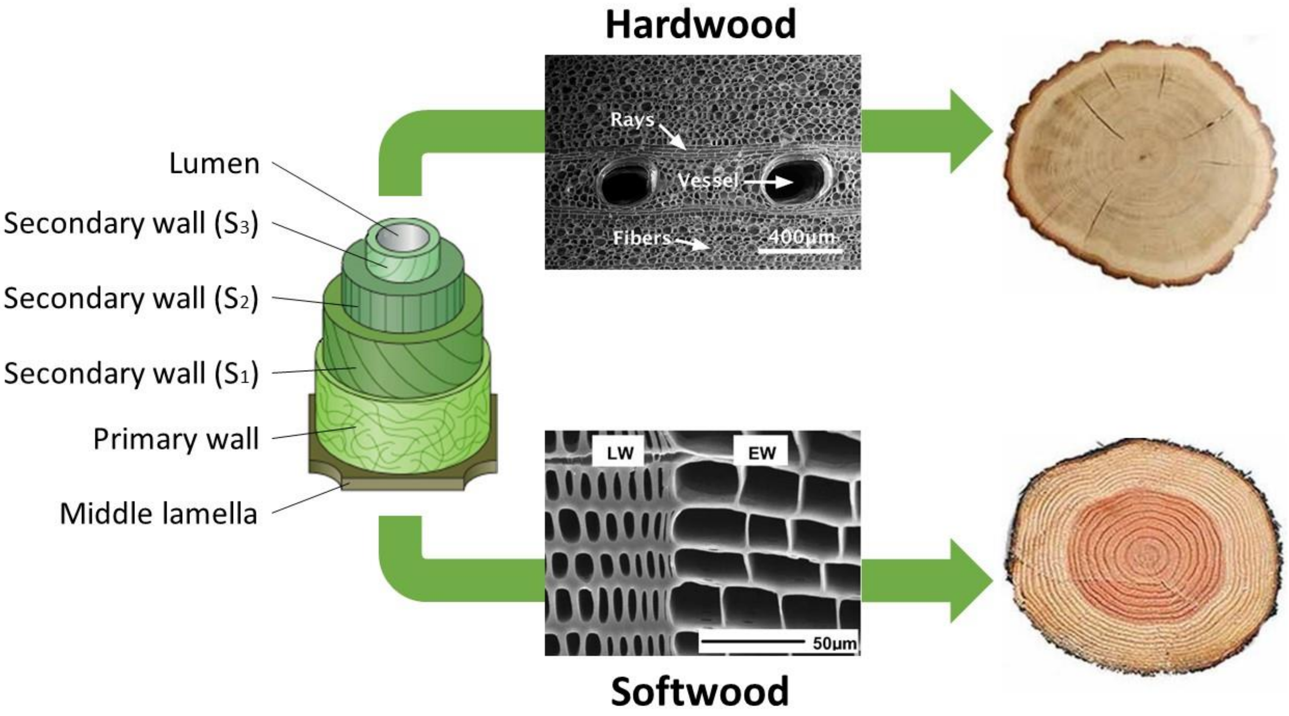

Figure 4 *– Schematic structure of the wood cell wall [38], scanning electron microscopy (SEM) images showing the presence of pores in hardwoods [39] and their absence in softwoods [40] and section of hardwoods and softwoods trees [41]*

Softwoods are less complex structurally than hardwoods because they possess a reduced number of cell types with fewer differences in dimension and arrangement. They do not present the vessel units and a single cell kind, the longitudinal tracheid, represents more than 90% of the total volume of most species of softwood. These longitudinal tracheids are noticeably longer than their counterpart in hardwoods, 3-5 mm against 0.1-0.8 mm, but shows a reduced diameter of 30-45 mm against that of 10-400 mm in hardwoods. Softwoods also contain ray cells, channels having thicker walls and smaller pore diameters than the tracheids. Ray cells occur between the tracheid cells and are oriented perpendicular to them (i.e., from the center of the tree to the bark). The diameter of these channels is approximately 20−50 µm, and the wall thicknesses are between 1 and 10 µm. Also important is the presence of pits, which are circular holes that link the channel walls, serving as interconnections between the channels. [42] Moreover, softwoods can be classified by the presence or absence of resin canals and the macrostructure characterized by the annual growth ring patterns, with rings of a few mm in the radial direction, formed by earlywood (EW) and latewood (LW) regions (Figure 4). [14, 40]

2.1.3 Cork wood

Cork is an interesting wood material that is primarily harvested from evergreen *Quercus suber*, also named cork oak. Although oaks generally belong to hardwoods, cork has unique chemical components and a peculiar porous 3-DOM microstructure which make it exceptional. Cork wood is mostly composed of suberin and lignin, which respectively represents the 45% and 27% of the wood. The minor fraction is formed by cellulose (~12%), waxes (~6%) and tannins (~6%). [42] Suberin is a lipophilic polyester biopolymer, composed of long chain fatty acids combined with glycerol, and its presence determines the main characteristics of cork. It is composed of lamellae around the cavities left empty by the dead cells, and can be found in many other parts of the plant body. Inside the bark, the lipophilic nature and the lamellar arrangement of suberin make cork an elastic material impermeable to gases and liquids, insulating towards sounds and heat, and resistant to the action of enzymes.

Cork's microstructure differs from any other lignocellulosic woods thanks to its hollow polyhedral prismatic cells. When viewed from the radial direction, cells have hexagonal honeycomb shape with average diameter of 15–20 µm, while, when viewed from the transverse directions, they possess a rectangular brick-like form of around 45 µm length (Figure 5b, c). [43, 44] The cell wall's thickness is 1-2 µm and this determines the presence of around 200 million cells per cm^3. [45] Due to this structure, cork exhibits a very low density of 0.12-0.24 $g \cdot cm^{-3}$ and exceptional characteristics which make it a good thermal, acoustic and vibrational insulator. [46]

The unique composition and structure are not the only features that make cork an interesting product. Cork is in fact a fully sustainable material since the bark from which it derives is periodically harvested every 9–13 years without harming the tree (Figure 5d). In order to regenerate its bark, a harvested cork oak tree will absorb large amount of CO_2, making cork forests one of the best examples of carbon storage sequestering up to 5.7 T CO_2/ha/yr. [47]. Not only does native cork represent a good model of an environmentally friendly material, but also its derived products like wine stoppers and byproducts like powder can be considered as such. For example, recycled cork wine stoppers may be used as precursors for electromagnetic interference (EMI) shielding applications while cork powder could be exploited as dye adsorbent material, as demonstrated by recent research. [48, 49]

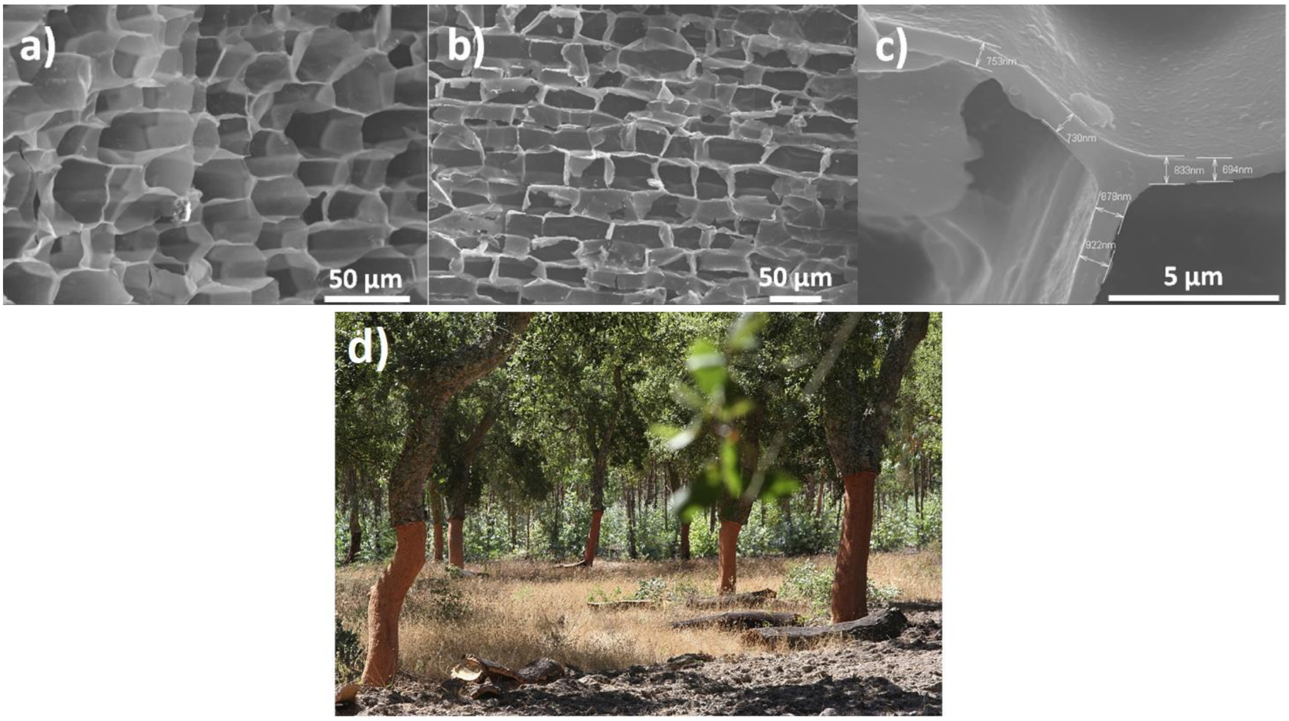

Figure 5 *– SEM micrograph of cork viewed from a) radial and b) transverse direction; c) High magnification micrograph of the cell walls [50]; d) Cork oaks after harvest [44]*

2.1.4 Cotton, pollen and leaves

Tree trunks are not the only component of lignocellulosic biomass that possess interesting micro and macro structure. Fractions such as cotton, pollen, leaves and petals can be exploited as templates to obtain peculiar products by mimicking their morphology.

Cotton is a soft fiber that grows around the seeds of the cotton plant. The length of different kinds of cotton fibre varies from 22 to 50 mm, and the diameter from 18 to 25 µm. The fibers have a multi-layered structure that resemble microfibrils in trees. An outer surface layer, the cuticle, surrounds a primary wall, a secondary wall and a lumen (Figure 6). The cuticle is a thin film of mostly fats, proteins and waxes. The primary wall comprises non-cellulosic materials and amorphous cellulose in which the fibrils are arranged in a criss-cross pattern. The secondary wall is composed only of highly ordered crystalline cellulose, in such a way as to form a compact structure in which cellulose fibrils lies parallel to one another. [51] Once traces of wax, protein, etc. are removed, the remainder is a natural polymer of pure cellulose. This cellulose is arranged in a way that gives cotton unique properties of strength, durability, and absorbency. Each fiber is made up of twenty to thirty layers of cellulose coiled in a neat series of natural springs. When the cotton boll (seed case) is opened, the fibers dry into flat, twisted, ribbon-like shapes and become kinked together and interlocked. This interlocked form is ideal for spinning into a fine yarn.

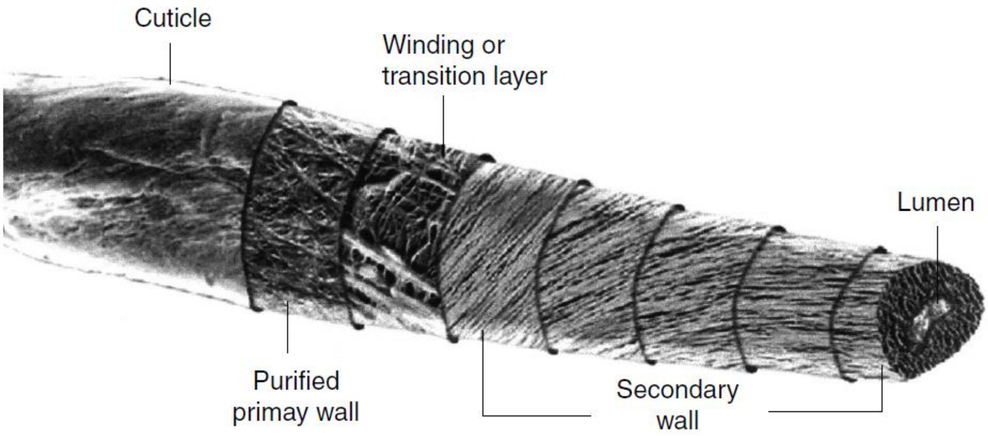

Figure 6 *- Morphological model of cotton fibre [51]*

Pollen grains are abundant, inexpensive and environmentally-friendly natural products with a high degree of species-specific morphological complexity, which show various architectures among species but uniform size, shape and morphology within one (Figure 7a). [52] The mature pollen grain is a capsule with diameters ranging from 2.5 – 100 µm, depending on the species. It is composed of a double wall encapsulating vegetative and generative cells of the plant. The inner layer is a thin delicate wall of unaltered cellulose, called the endospore or intine. The outer layer, on the other hand, is a tough resistant barrier composed largely of sporopollenin called the exospore or exine (Figure 7b). The exine often bears spines or warts, or is variously sculptured, and the character of the markings is often of value for identifying genus, species, or even cultivar or individual.

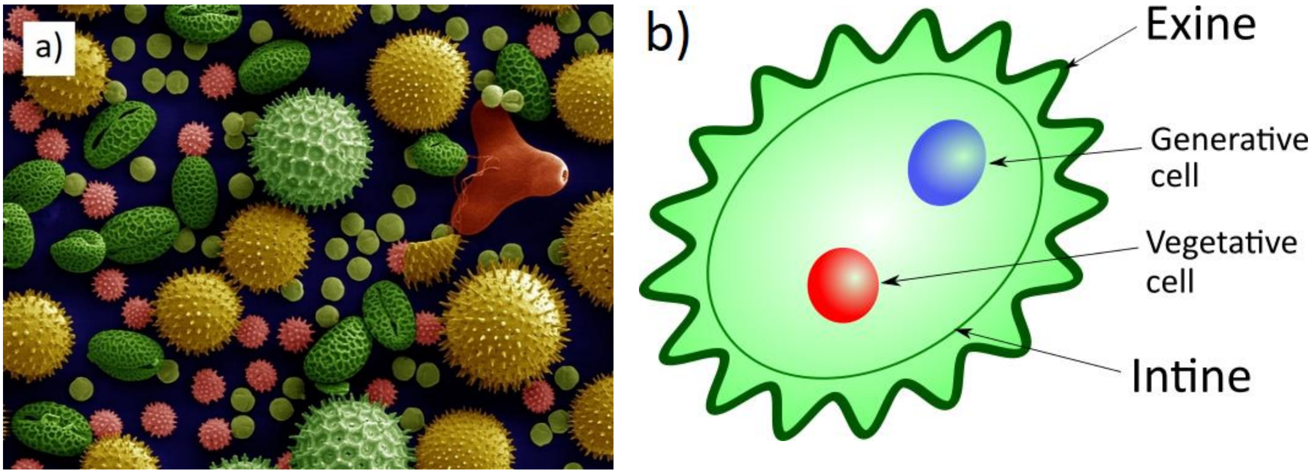

Figure 7 *– a) Coloured SEM image of various architectures of pollen grains [53]; b) Schematic structure of pollen grains*

Using their leaves, plants combine sunlight, carbon dioxide and water to produce glucose and oxygen through a process called photosynthesis. The top of a leaf is exposed to the most sunlight, and here cells specialised for trapping light are present (Figure 8a). These cells are called palisade mesophyll cells (30-40 µm length), and have high concentrations of chlorophyll (Figure 8d), the compound used by plants to absorb light, inside peculiar structures called thylakoids. Thylakoids are cylindrical interconnected nanolayers possessing unique morphology and high surface area, useful to harvest incoming sunlight (Figure 8c). These structures are found inside organelles called chloroplasts, flat disks with a diameter of 2-10 µm and about 1 µm thick (Figure 8b). The bottom of the leaf presents little pores, called stomata which, when opened, allow CO_2 to diffuse into the leaf. The stomata are controlled by 'sausage shaped' guard cells, which open up to let carbon dioxide in. Moreover, these guard cells can also close the stomata, to stop other molecules from escaping, such as water.

The carbon dioxide comes in from the stomata, and then makes its way up through the leaf, through the gaps in the spongy mesophyll layer in the bottom part of the leaf, and heads up to the palisade cells where photosynthesis occurs. The final reactant needed for photosynthesis is water. Water comes into the plant through the roots, moves up the stem and enters the leaf through the vascular bundle. The vascular bundle contains a hollow tube specifically for water movement called the xylem. The veins on a leaf are the vascular bundle, allowing water to spread out through the leaf.

To prevent undesired organisms like bacteria getting inside, or reactants like glucose getting out before being used, at the top and bottom of the leaf there are epidermis cells (Figure 8a). These cells produce a protective waxy cuticle layer which seals up the leaf so that the only accessible gateways are stomata, which are regulated by the guard cells.

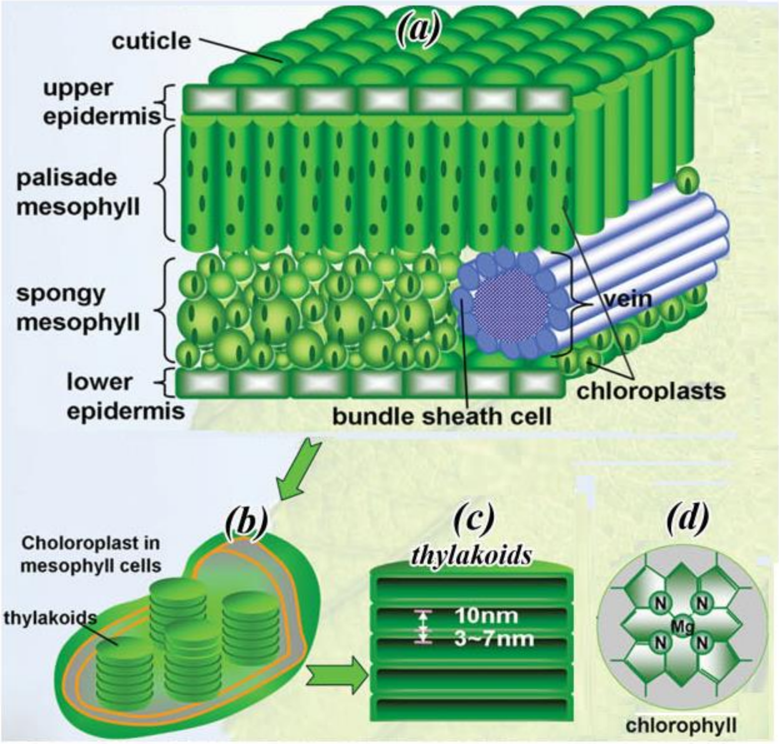

Figure 8 *– Internal structure of leaves: a) section of a leaf, b) section of a chloroplast, c) section of a thylakoid, d) scheme of a chlorophyll molecule [54]*

2.2 Lignocellulosic biomass processing

Identifying the best pathway to convert the lignocellulosic biomass into new products with additional value can be a hard task. In order to optimize the transformation process, it is essential to have a deep understanding of the required steps, and a wide access to different technological options, including mechano-physical, chemical, biological or thermochemical methods, or a combination of them. In Figure 9 is represented a scheme of the processes that lignocellulose can undergo.

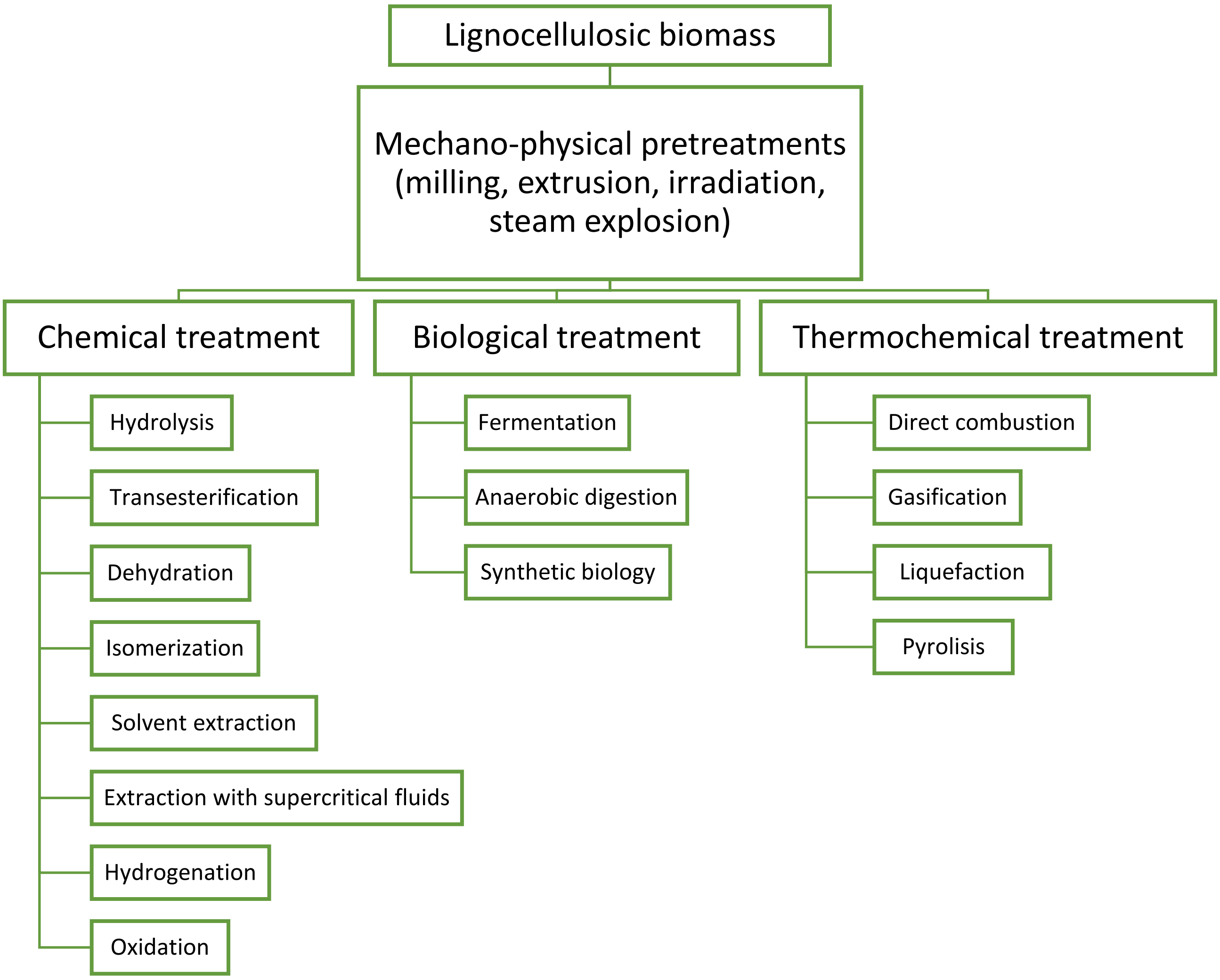

Figure 9 *– Possible processes that can be applied to lignocellulosic biomass*

Mechano-physical processes such as milling, extrusion, steam treatment, and irradiation with gamma rays or with electron or microwave beams are often used to reduce the size or separate the substrate into its main components, without changing its status or composition. [55]

Chemical treatments refer to processes such as hydrolysis, transesterification, dehydration, isomerization, extraction with solvents, extraction with supercritical fluids, hydrogenation and oxidation, which directly convert biomass into chemicals, changing the structure of the substrate, at relatively mild temperatures or pressures and in the presence of a catalyst. [56] These transformations can be involved both in the pre-treatment of the biomass and in the downstream processing phases, to convert the chemical intermediates, obtained through thermochemical or biological processes, into final products. Hydrolysis, for example, uses acids or enzymes to split the glycosidic bonds and depolymerize the polysaccharides into simpler monomeric sugars, as happens for the production of glucose from cellulose.

Biological treatments, such as anaerobic digestion and fermentation, have been recognized as being among the most ecologically benign technologies, since they involve the use of enzymes or living organisms to catalyse the transformation of biomass into chemical substances. [57] In recent decades, bioprocesses have found applications in the production of high value compounds such as pharmaceutical products (and their intermediates) and, in more recent years, they have also been used in the production of fuels. [58] For example, the use of enzymes such as cellulases and hemicellulases to hydrolyse cellulose into monomeric sugars has nowadays become a consolidated process to produce ethanol. [59]

Thermochemical treatments include direct combustion, gasification, liquefaction or pyrolysis, which are processes involving the conversion of the biomass at more severe temperatures and/or pressures of the usual pathways. [60] Direct combustion of biomass in an oxygen rich environment is mainly used for the production of heat, while gasification, which consists of treating biomass with low oxygen levels at high temperature (> 700 ° C), is used to produce mixtures of H_2, CO, CO_2 and CH_4, so-called syngas, which can be used directly as a biofuel, or as an intermediate chemical for the production of fuels or other compounds. [61]

2.2.1 Conversion of wood into ceramics

Conversion of lignocellulosic biomass into ceramics can be performed both on native wood pieces and on pre-treated products, such as sawdust, paper, cardboard, etc. The former one will give rise to the fabrication of more heterogeneous structures on the macro-, meso- and microscale, since after treatment the final material will follow the natural structure of the original sample. The conversion of pre-treated lignocellulosic biomass, however, is easier because the processes previously carried out, removed the majority of hemicellulose and lignin leaving only cellulose intact. At the end, the wood fibers can remain preferentially oriented based on the procedure they underwent.

The reactive transformation of wood materials into carbide or oxide ceramics can be performed in two different procedures, namely transformation and substitution (Figure 10) [8, 34]:

- Transformation: the starting lignocellulosic sample is pyrolyzed at high temperature and inert atmosphere to give rise to a porous carbon replica which subsequently is placed to react with liquid or gaseous metallic or organometallic precursor to produce carbide ceramics.
- Substitution: wood template, previously pyrolyzed or in its native form, is infiltrated with suitable precursor and a successive oxidative reaction is performed to remove the carbon residue creating the substitutive oxide ceramics.

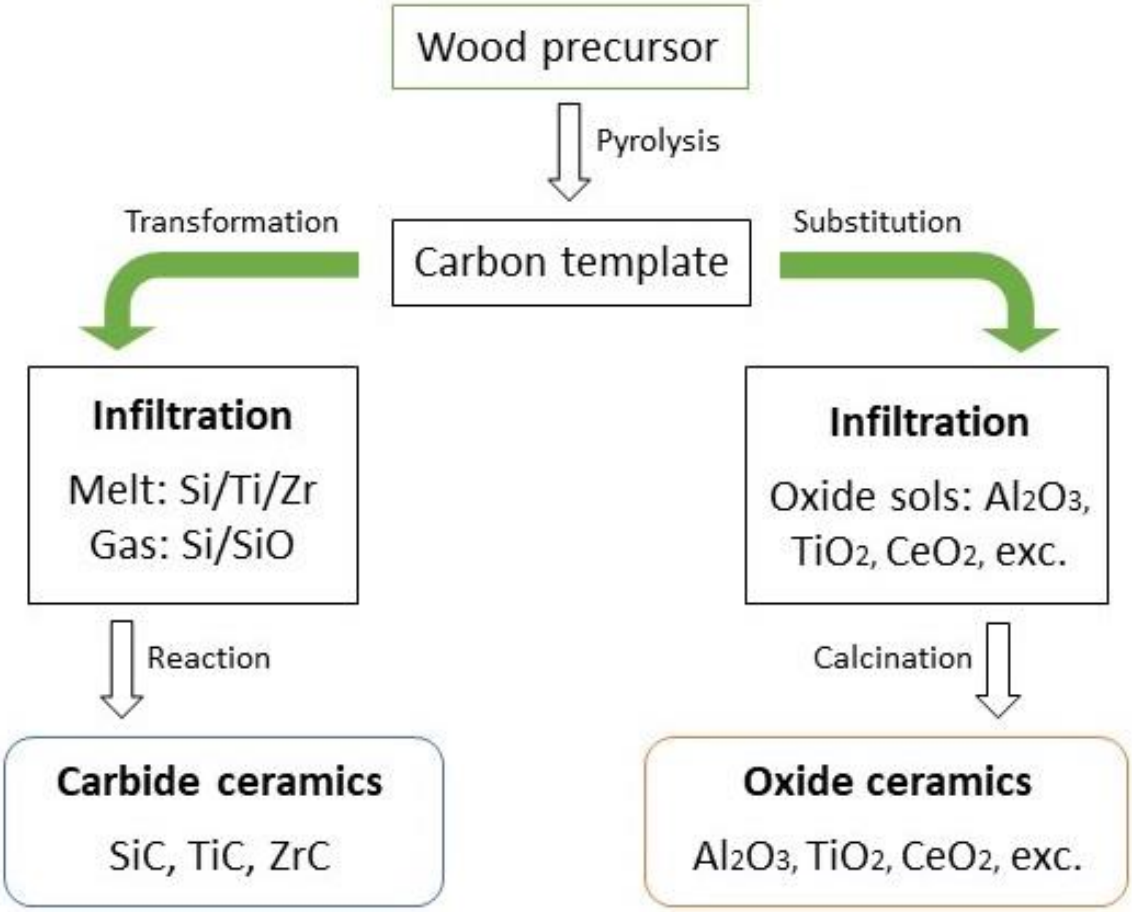

Figure 10 *– Processes to convert wood materials into carbide or oxide ceramics*

Pyrolysis is the important step for the conversion of wood into carbon and is based on a series of complex reactions which are influenced by many factors such as heating rate, atmosphere, temperature and composition of biomass material. The series of steps involved in pyrolysis start at 150 °C with the desorption of adsorbed water from the surface. Then, between 150 °C and 240 °C, the subsequent splitting of the cellulose structure from water occurs, and immediately afterwards the depolymerization reactions and breaking of C-O and C-C bonds of hemicellulose, cellulose, and lignin begins [62]. These three compounds show different thermal degradation behaviours because of their different chemical composition and structure: hemicellulose decomposes first at 200-260 °C, cellulose next at 240-450 °C, showing a higher thermal resistance with a wider degradation range, and lastly between 280 °C and 500 °C the lignin bonds break happens. [63] However, degradation temperatures may vary among lignocellulosic biomass type. For example, in case of cork wood the total conversion of biological materials into carbonaceous structure is dependent also by suberin degradation, which start at 250°C and can end also at temperatures higher than that of lignin. [43] Eventually, increasing the temperature up to 800 °C will provide the release of hydrogen and the occurrence of decomposition and rearrangement reactions that will give rise to the final carbon template structure. [14]

During pyrolysis, a significant weight loss in the range of 70–80% and a shrinkage between 20 and 40% is observed, depending on the composition and molecular structure of the wood tissue. [15] However, despite the weight loss and contraction during carbonisation, the microstructure of the initial wood material is maintained. Moreover, the use of pre-treated lignocellulosic samples, as well as the infiltration with carbon-containing liquids, can reduce the anisotropy and the amount of the shrinkage [13]. The successive conversion into ceramics by infiltration with liquid or gaseous metal-based precursors does not involve significant geometrical variations, and can be viewed as a form of template shape manufacturing [64].

It is important not to confuse the production of ecoceramics with that of “woodceramics”. Although the latter are also wood-derived products, they can not be properly defined as ceramics since are formed only by organic hydrocarbon materials filled with a phenolic resin, without the presence of any other metallic or non-metallic element. After being impregnated with resin, wood material is carbonized in vacuum atmosphere giving rise to amorphous and glassy carbon, maintaining the original hierarchically porous arrangement of the template. [65] The resulting structure is light, hard, porous, corrosion resistant, heat resistant, and electrically conductive which makes it a promising material for applications such as electromagnetic shielding. [66]

2.2.1.1 Biomorphous carbide ceramics production

After pyrolysis, transformation of the obtained carbon template into carbide ceramics can be performed by infiltration and reaction with liquid or gaseous silicon-containing precursors, in the case of silicon carbide (SiC). The most investigated element for this is silicon, whose compounds are infiltrated into the porous biocarbon char at temperatures between 1400 °C and 1600 °C, undergoing the reaction reported in Scheme 1 [14]:

$$C_{Bio} + Si\ (l\ or\ g) \longrightarrow SiC$$

Scheme 1 *– Reaction for SiC formation*

Liquid infiltration is performed under vacuum conditions, typically using a silicon alkoxide such tetra-ethyl-*ortho*-silicate (TEOS, $Si(OCH_2CH_3)_4$). In this method, TEOS, usually dissolved in an acidic alcohol/water solution to form a silica sol, is impregnated in the template while it is placed under vacuum. After that, the sample is dried and subsequently heated at high temperatures (1400-1600°C) in an inert atmosphere, resulting in the biomimetic SiC ceramic with the porous cellular structure of the original wood (Figure 11). The treatment procedure of infiltration and drying, namely the infiltration cycle, can be repeated several times, to increase the silica content in the composites. [67, 68]

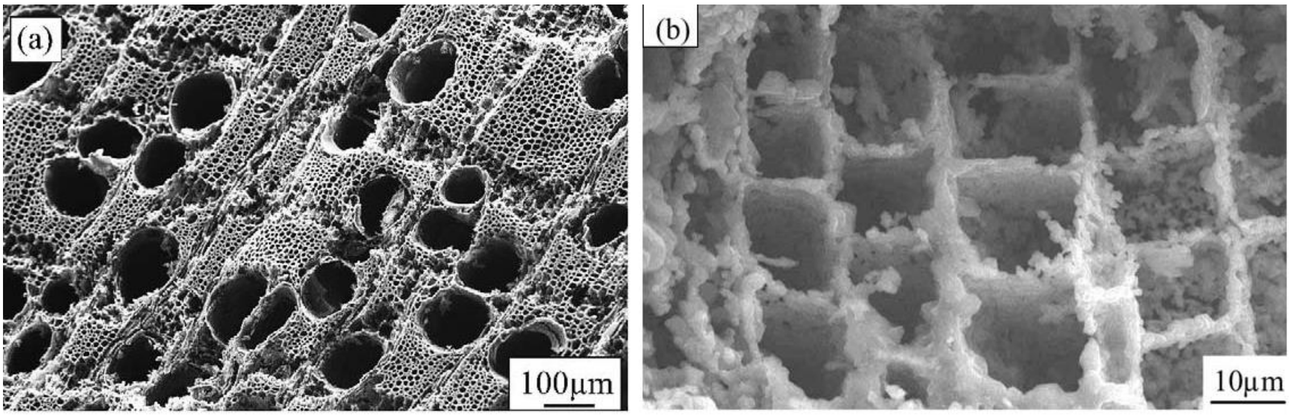

Figure 11 *- SEM micrographs of biomorphous SiC ceramics obtained through vacuum liquid infiltration from a) oak wood [67], and b) Tilia amurensis wood after 5 cycles of infiltration [68]*

An alternative approach is that the carbonaceous template is put in a thermally resistant crucible and covered with silicon powder, the temperature then increased above the Si melting temperature (1410 °C), thus allowing liquid silicon to penetrate inside the pores. Using higher temperatures reduces the time to complete infiltration, since the viscosity of the Si fluid is decreased. [14, 15] At 1550 °C, the Si permeates the template by capillarity in seconds, filling the macroporous cells of the wood, typically varying in size between 5 and 100 μm in diameter. [14] At this temperature, nearly 30 min of reaction time is necessary to achieve complete conversion and stable carbide ceramics, demonstrating how the SiC formation reaction is the rate limiting step of the process. [14, 69] Excess silicon content is crucial to make sure of a complete carbon reaction, therefore, the Si/C ratio usually surpasses that determined by the stoichiometry by a factor that spans between 1.2 and 2, depending on the porosity of the sample. The additional silicon will undergo a sintering process filling the pores of the template and resulting in structures like in Figure 12a. This method with melted Si powder fills in the porous cells of the wood, forming an inverse templated structure of cell-sized silion carbide grains. Any excess of Si content in the ceramic can be subsequently removed by using wet chemical leaching processes such as mixture of HF/HNO_3. [18]

In contrast to liquid infiltration with melted silica, no elemental silicon was observed in the biomorphous SiC ceramics obtained with the Si-vapor phase technique (Figure 12b). [70] In this method, silicon vapour is generated by melting the silicon precursor powder at a temperature of 1600 °C for a period of time that ranges between 1 and 8 h in an inert atmosphere. The formed gas penetrates the pyrolyzed wood template, and reacts with the carbon to form single-phase, highly porous, biomorphous SiC-ceramics which mimic the structure of the wood, without trace of residual silicon grains.

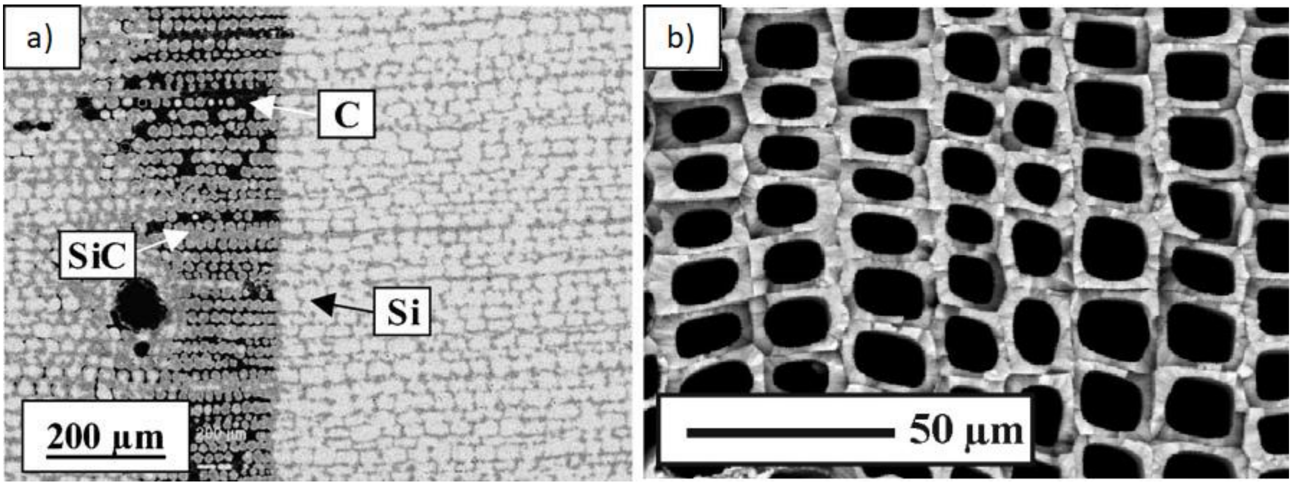

Figure 12 *- SEM micrographs of biomorphous SiC ceramics obtained from a) Si-melt infiltration of pine wood at 1550 °C forming and inverse-template wood structure [71], and b) Si-gas infiltration of oak wood at 1600 ◦C forming a biomimetic wood-like porous cellular structure [70]*

Most of the research performed focuses attention on the production of biomimetic SiC ceramics, while much less deals with metallic carbide ceramics, such as TiC or ZrC. TiC has been successfully synthesized using wood materials as a template both with liquid and gaseous techniques. Sun et al. [72] obtained TiC ceramics through melt infiltration with a higher surface specific area and porosity than the starting carbon preform, via the conversion of a tetrabutyl titanate precursor firstly into the anatase form of TiO_2, then into rutile, and finally into the carbide during a heating process under vacuum. Chemical vapor infiltration and reaction were used to produce biomorphic cellular TiC ceramics from paper, using $TiCl_4$ as a titanium source and H_2 as gas carrier and reductive agent. [73] A liquid based carbothermal reduction (Scheme 2) of TiO_2 and ZrO_2 sols was used to manufacture TiC and ZrC ceramics employing pyrolyzed pine as carbon source. [22] After the infiltration of the metal oxide colloidal solutions into the carbonaceous template, the samples were annealed at temperatures up to 1600 °C for 1 h in an argon atmosphere to convert them fully to oxides, and then to promote the subsequent reaction between carbon and the metal oxide with the loss of oxygen as CO.

$$\mathrm{MeO_2} + 3\mathrm{C} \longrightarrow \mathrm{MeC} + 2\mathrm{CO}$$

Scheme 2 *- Carbothermal reduction of metal ("Me" represents a general metallic element)*

3. Production of oxide ceramics

Since the properties and behaviour of ceramics highly depend on their size, shape, composition and morphology, a great amount of attention is given to their production methods. In addition, in order to be good competitors in the market and to not worsen the already grave environmental crisis, the synthesis of ceramics should be economically inexpensive and ecologically reliable. Some of the various procedures that have been developed for these purposes are:

- *Sol-gel method*: the sol–gel process is one of the well-established synthetic approaches to prepare high-quality oxide ceramics as well as mixed oxide composites. The main advantages of this method are excellent control over the texture and the surface properties of the materials. In general, the sol–gel method can be described in five key steps: hydrolysis, condensation, aging, drying and thermal treatment. [74]
- *Chemical vapour deposition*: chemical vapour deposition (CVD) is a technique in which gaseous reactants are deposited onto a template surface to obtain a final structure mimicking the starting one. CDV is employed thanks to its flexible chemistry and the possibility of obtaining replicas with near-net shaping to the original template. [29]
- *Hydrothermal method*: hydrothermal synthesis refers to heterogeneous reactions in aqueous media above 100°C and 1 bar. Hydrothermal chemistry has established itself as the principal method for the synthesis of microporous materials containing an organized pore structure with pores in the size range 4–20 Å, like zeolites. [75]
- *Co-precipitation method*: co-precipitation is one of the successful techniques for synthesizing ultrafine ceramic powders with narrow particle size distribution. Conventional method involves mixing of a solution of mother salts and a precipitant to obtain, after the heating process, a ceramic final product. [76]
- *Supercritical fluid (SCF) deposition method*: SCF deposition technique exploits the unique features of supercritical fluids such as low viscosity, high diffusivity and zero surface tension, to act as solvent carriers impregnating the template with the precursors. After subsequent aging and heating treatments the final desired product can be obtained. SCF deposition method has been applied to prepare materials with special structures, which are difficult and/or impossible to obtain with traditional procedures. [77]

3.1 Sol-gel process

One of the most commonly used liquid phase procedures for the production of oxide ceramics is the sol-gel process. The sol-gel method is a synthetic strategy that operates in mild conditions of temperature and pressure, and allows one to obtain pure and homogeneous ceramic materials exploiting polymerization reactions induced by water. The benefits derived from preparing ceramics by the sol-gel process are high purity, homogeneity and a large variety of forms that the final product can assume. [78]

The sol-gel process starts with the preparation of the so-called sol: it consists of a solution in which a solid phase, made by microscopically dispersed insoluble particles, is suspended throughout a liquid solvent and does not agglomerate or sediment; this system is also called colloidal solution. In the case of metal oxides, the sol particles are usually hydrolysed metal hydroxides or metal oxy-hydroxides, partially polymerized.

Further processing of the sol enables one to make ceramic materials in different forms. When the sol is dried or evaporated, possibly in a mould, its hydrolysed compounds start to bind to each other forming oligomeric particles that act as nucleation centers in a condensation reaction; the 3-dimensional structure formed in this way is called *gel*. Additional drying and heating treatments performed on the gel can convert it into different ceramic materials. If the liquid in a wet gel is removed under supercritical conditions, a highly porous and extremely low-density material called an aerogel is obtained. [79] Ceramic fibres can be obtained by adjusting the viscosity of a sol within a certain range. [80] Moreover, ultra-fine and uniform ceramic powders can be formed by precipitation [81], spray hydrolysis [82] or emulsion techniques. [83] The various steps of the sol-gel process and the possible products obtained can be summarized in the flow-chart below (Figure 13):

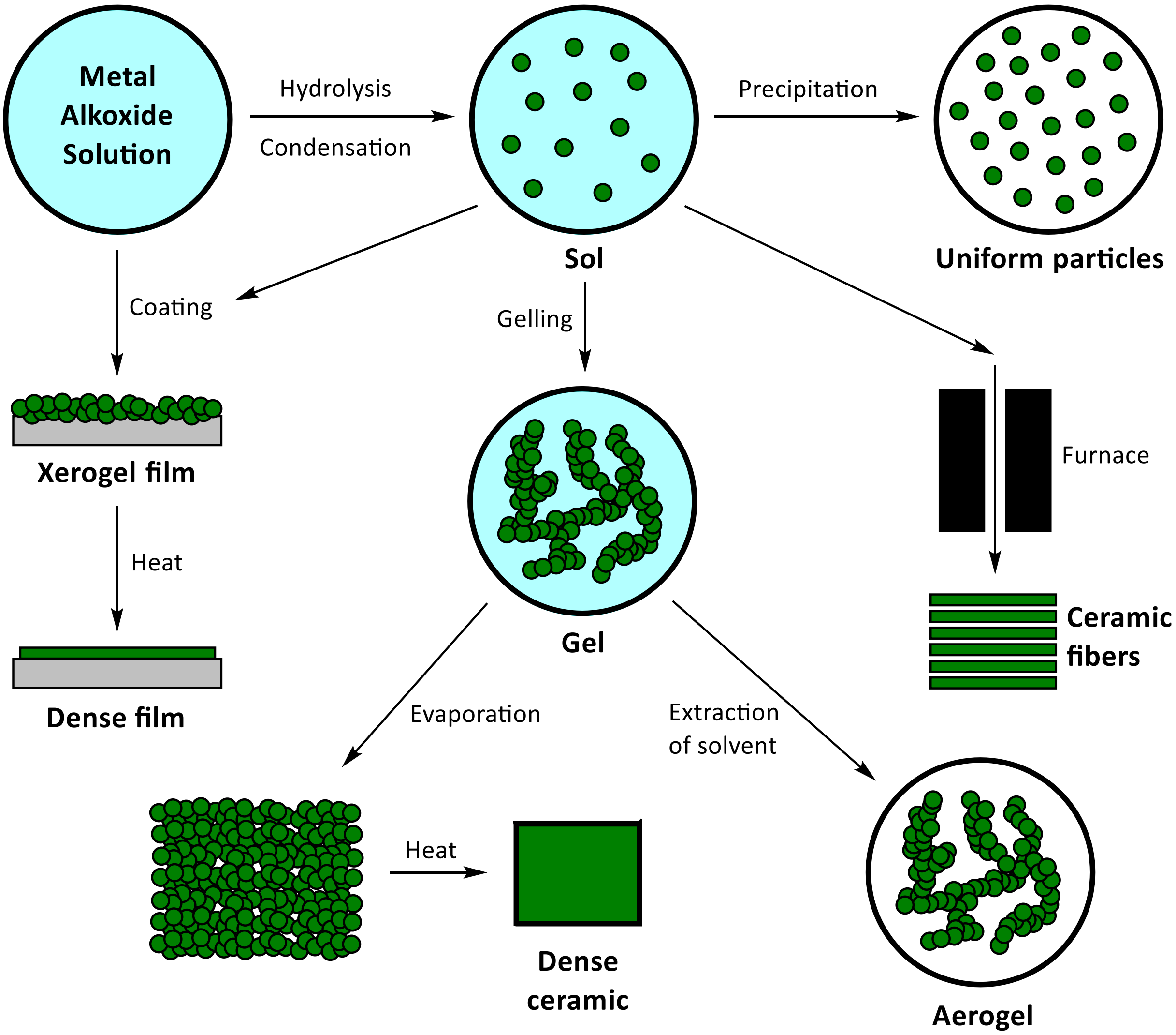

Figure 13 *– Products obtainable by Sol-Gel process*

The potential applications of sol-gel processing can be used in various fields, from the production of thin films and coatings useful for optoelectronic purposes, to the creation of porous gels and membranes with high surface area and useful applications such as filtration, separation and catalysis. This large variety of uses derives from the abovementioned advantages that sol-gel method presents over the conventional melting of glass, or standard thermal reaction of oxide and/or carbonate powders (calcination). However, some disadvantages are still present, and they include the cost of the raw materials, the shrinkage that accompanies drying steps and the long processing times. [84]

3.1.1 Mechanism of the sol-gel process

The sol-gel process proceeds in two different ways, according to the nature of the precursor. Generally, precursors used can be inorganic metal salts like nitrates, sulphates, chlorides, etc., organic metal salts such as citrates, acetates, etc., or metal organic compounds such as alkoxides, $M(OR)_x$. Both inorganic and organic metal salts are usually soluble in water, enabling a whole aqueous process to be used. With metal salts more complex hydrolysis and condensation steps are involved, and the formation of the final product highly depends also on the temperature and the adjusted pH of the solution. Furthermore, the role of counter ion of the salt is not exactly known, and can greatly affect the morphology and chemical composition of the ceramics, with additional difficult treatments sometimes necessary for its removal. Many of these drawbacks in using metal salts for sol-gel oxide preparation can be avoided by using alkoxide precursors, due to their easy purification, high solubility in organic solvents, high volatility and extremely facile hydrolyzability. [85] However, alkoxides are also generally more expensive, and they are also often air and moisture sensitive compounds, requiring the use of dried (completely water-free) solvents, glove boxes and air-free atmospheres during preparation and reaction, greatly increasing the complexity and cost of synthesis. Often no water at all can be present before the hydrolysis and condensation reactions are begun, otherwise the alkoxide will instantly precipitate. Some metals are not easily available in the form of soluble salts, and alkoxides can be the only viable alternative.

3.1.1.1 Sol gel method using metal salts as precursor

When metal salts (chlorides, nitrates, sulphates, acetates etc.) are dispersed in aqueous medium, they form hydrated species via coordination of electrons to vacant *d*-orbitals of the metal ion, and thus generating hydrated metal cations. In turn, the partial charge on the hydrogen increases, making the water molecule more acidic and causing the formation of hydroxy species. Depending on the acidity of the solution, the following hydrolysis equilibria are established (Scheme 3) [84]:

$$M[(OH_2)]^{z+} \rightleftharpoons [M\text{-}OH]^{(z-1)+} + H^+ \rightleftharpoons [M{=}O]^{(z-2)+} + 2H^+$$

Scheme 3 *– Equilibrium reaction of metal salts in aqueous solution*

In these conditions, hydrated metal cations act as Lewis acids and undergo complex polymeric reactions (condensation or peptization), that will lead to the ultimate formation of oxide ceramics. The reactions that takes place in aqueous medium are olation, which is the formation of metal-hydroxy-metal bonds (M-OH-O), and oxolation, which represents metal-oxy-metal bond (M-O-M) development. However they rarely proceed smoothly, and the final products in sols present generally heterogeneous characteristics – although often referred to as purely metal hydroxide or oxide sols, they are usually mixed oxy-hydroxide sols. If the metal salt is highly reactive, the hydrolysis rate will be very high, but in the case of less active precursors, the velocity can be tuned by changing the pH of the environment. In acidic solution, hydrolysis can either facilitate or prevent the hydroxyl complex formation, while in basic solution the reaction moves in the forward direction giving rise to oxo-bridged complexes. [85]

The problem of using metal salts as precursors is that, usually, their aqueous solutions are very stable and do not show the typical gel composition. They need to be precipitated first as hydroxides (typically with a base), and then peptised/condensed with added counterions, usually acids, to form stable sol particles. Moreover, drying and heating steps do not always lead to the production of homogeneous ceramic oxides, but can lead only to the formation of irregular particles or the reformation of the original metal salts. To prevent this from happening, small molecules are sometimes added to the solution, such as chelating agents or gelators, capable of forming stable linked complexes with metal ions, and thus creating homogeneous mixtures with gel-like structure. These small molecules can be of various categories: from the well known ethylenediaminetetraacetic acid (EDTA), citric acid, glycolic acid and tartaric acid, to synthetic or natural polymers such as starch, dextran and chitosan. For example, citric acid, the most common, low cost and easily available gelator, is frequently added in these procedures, especially when metal precursors are nitrates. The subsequent removal of the solvent and organic material from the solution by drying and heating treatment will result in the production of the desired oxide ceramic material and, in the case of nitrate precursors with organic compounds present, with porous and spongy nature due to the large amount of released nitrous gases in an exothermal combustion process. [85]

3.1.1.2 Sol-gel method using metal alkoxide as precursor

Metal alkoxides are widely employed as molecular precursors to glasses and ceramics thanks to the presence of highly electronegative OR groups, which makes the central metal very susceptible to nucleophilic attack. Most of the alkoxide precursors in sol-gel processes involve the presence of early p-block elements (i.e. Al, Si) or early transition metals (i.e. Ti, Zr). However, many other alkoxides can be used for this purpose, [86] and alkoxides can be formed of group II metals which have poorly soluble salts (i.e., barium). The lower electronegativity of the transition elements with respect to silicon (the most frequently used non-metallic alkoxide precursor in sol-gel methods) causes them to be more electrophilic and, therefore, less stable toward hydrolysis, condensation and other nucleophilic reactions. This fact makes transition metals processing more difficult compared to $Si(OR)_4$ and, moreover, requires stricter control of the sol-gel parameters in order to obtain homogeneous gels instead of precipitates. [84]

The main steps involved in sol-gel methods using metal alkoxides as precursors are two competitive reactions: hydrolysis (Scheme 4) and condensation (Scheme 5). Hydrolysis occurs through the nucleophilic attack of water's oxygen on the metallic atom of the precursor. This equilibrium reaction leads to the breaking of the metal alkoxide's OR bonds, and the formation of M-OH groups on the metallic atom.

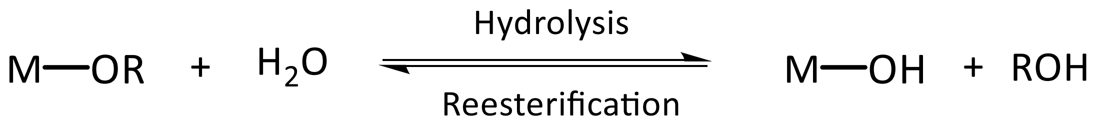

***Scheme 4** – Hydrolysis and reesterification*

Condensation, on the other hand, is the step in which M-O-M bonds are formed by the reaction between two M-OH groups (oxolation) or between M-OH and alkoxy groups (alkoxylation) of different molecules, as shown in the Scheme 5. These bonds will constitute the skeleton of the three-dimensional structure of the inorganic polymer gel.

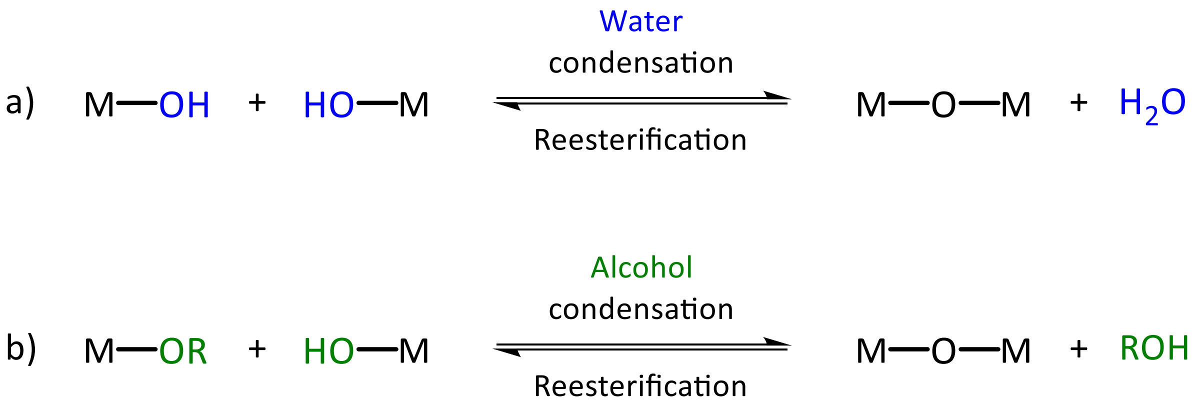

***Scheme 5** - Formation of M-O-M bonds through a) oxolation or b) alkoxylation*

The final structure and properties of metal oxides are strongly dependent on hydrolysis and condensation reactions, which themselves are affected by different parameters such as the pH of the solution, the nature of the OR group (i.e. inductive effects), the water to alkoxide molar ratio (R_w), the solvent and the temperature.

In case of silica sol-gel chemistry, the most extensively studied due to its smoother reactivity, an acidic or basic catalyst is required, since the natural reaction is very slow. The type of catalyst, however, highly influences the final structure of the product, due to the relative variations of hydrolysis and condensation rate. In case of acid catalysis, the protonation of the OR group by hydrogen ions causes a reduction of electron density in the silicon and, thus, an increased electrophilicity. In this condition, the silicon atom is more reactive and can be more easily hydrolysed (Scheme 6a). During basic catalysis, instead, the attack of the OH^- ion on the central Si atom makes it less electropositive and, therefore, less susceptible to subsequent nucleophilic attack by water (Scheme 6b). With these considerations, the basic catalysed hydrolysis will initially proceed with lower velocity compared to the acid catalysed mechanism. The rate of each hydrolysis step will, however, be increased or decreased depending on the number of OH and OR groups present on the silicon atom, reflecting their relative electron withdrawing or donating power. The result is that successive hydrolysis steps get progressively slower under acidic conditions and faster under basic conditions. [78, 87] Similar processes can occur with metal atoms in the place of silicon.

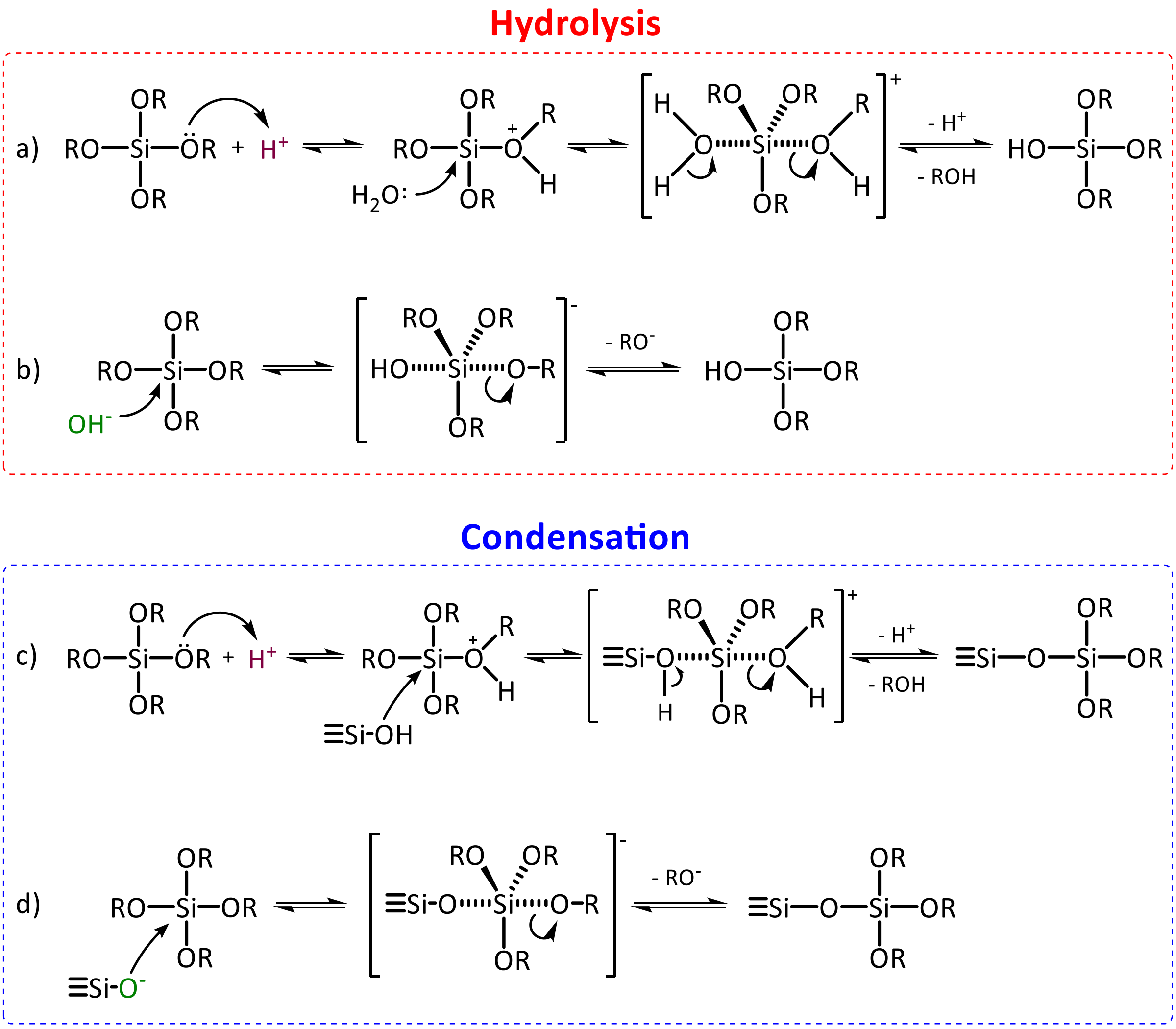

***Scheme 6** – a) acid and b) basic catalysed hydrolysis and c) acid and d) basic catalysed condensation*

Condensation follows a similar pattern, being catalysed by either acid (Scheme 6c) or base (Scheme 6d) and resulting in the formation of siloxane bonds (or metaloxane bonds for metals). Also, the progression of condensation is influenced by the type of catalyst used, and by the number of OR and OH groups that are present on the silicon center. [87] During acid catalysis, the ease of alkoxy group protonation in a partially growing structure increases with the number of OR groups still bound to the metal, reflecting their electron-providing power. Therefore, the silicon atoms in Figure 14 that will preferentially undergo condensation reactions are, in order, D >> A > C >> B. Acid-catalysed condensation is hence directed toward the end of the polymer, rather than the center, resulting in a less branched chain-like structure. On the contrary, in alkaline conditions, the order of reaction is inverted, and the nucleophilic attack will preferentially occur in the middle part of the molecule, giving rise to more compact and spherical particles. [84]

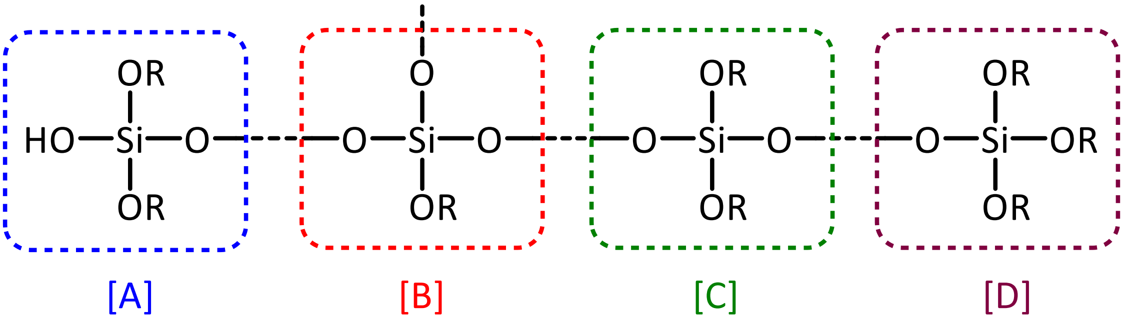

Figure 14 *– Partially growing* SiO_2 *particle*

The nature of the alkoxy groups on the silicon atom is also an influencing factor on the hydrolysis and condensation rate. In general, due to inductive effects, the bulkier the OR group, the slower the kinetic of the reaction. However, to accelerate the speed using the same starting precursors, it is possible to increase the reaction temperature, since it is proved that higher temperature reduces the completion time. Furthermore, the solvent plays a fundamental role because most alkoxides, such as TEOS, are not water soluble. This means that characteristic such as polarity and proticity of the solvent must be taken into account during sol-gel synthesis, according to the compounds involved. [78]

The water to alkoxide molar ratio (R_w) has an important part in controlling the hydrolysis reaction and in the formation and growth of nucleation sites. It is possible to divide the reaction mechanisms based on three different values of R_w (Scheme 7). When $R_w < 2$ (Scheme 7a), the hydrolysis between metal alkoxides and water is incomplete, hence condensation reactions occur between monomers causing the formation of particles with irregular shape and low surface area. [88] When $2 < R_w \leq 4$ (Scheme 7b), a stronger nucleophilic reaction between water and alkoxide monomers occurs, and a three-dimensional network with varying textures can be formed. Further calcination treatment will lead to the synthesis of particles with a high specific surface area, due to residual voids in the network structures. When R_w is used over a critical value (i.e., the value corresponding to the maximum specific surface area) (Scheme 7c), the hydrolysis is complete and more alkoxides convert to the corresponding metal hydrates, $M(OH)_x$. Then, the monomers of $M(OH)_x$ react with each other to form particle-like polymers. The specific surface areas of these materials after heat treatment are low since the hydrogen bonding between the particles makes them pack more efficiently. [89]

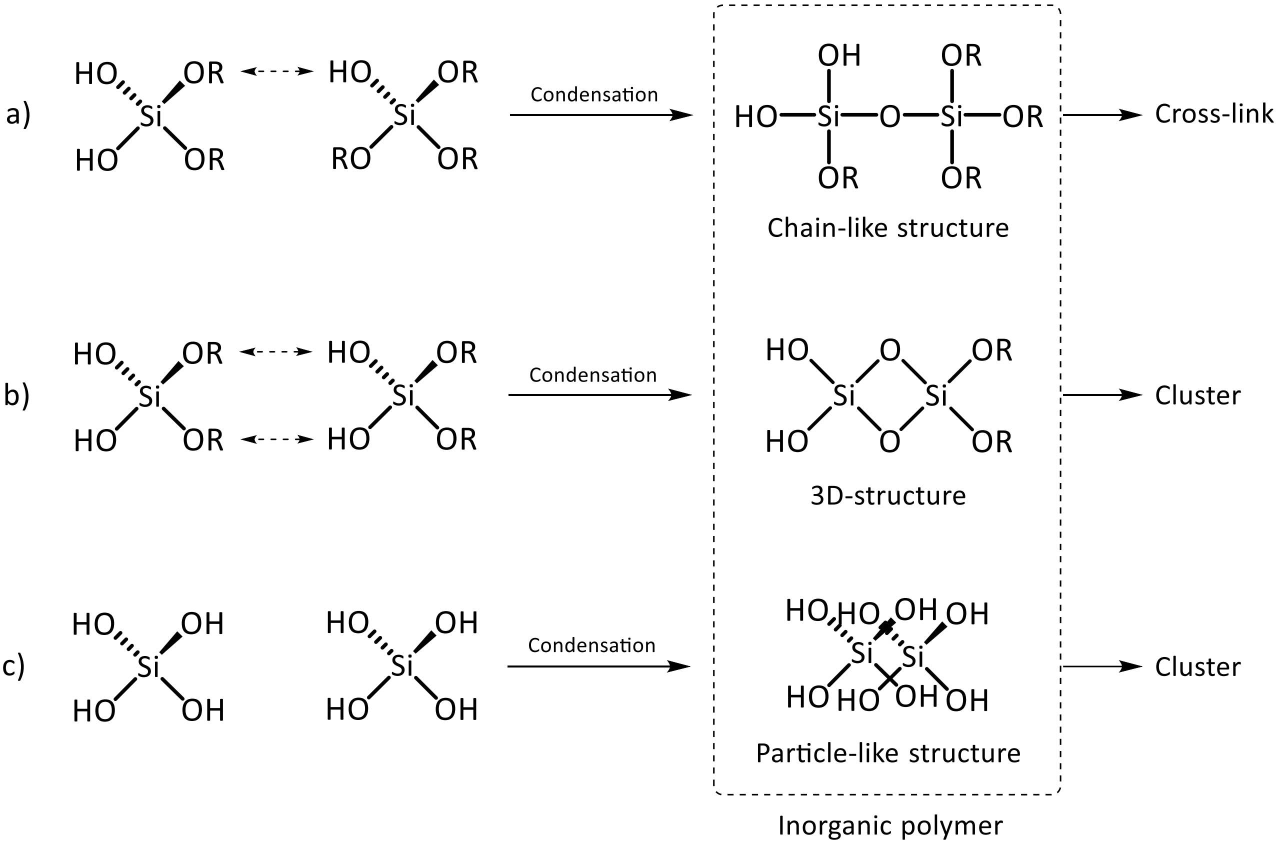

Scheme 7 *- Diagrams of sol-gel process at different water contents: a)* $R_w < 2$*, b)* $2 < R_w \leq 4$*, c)* $R_w >$ *critical value*

4. Biomorphous oxide ceramics

Biomorphous hierarchical porous ceramics are an interesting class of material which presents peculiar properties such as high surface area, large porosity and low density, which makes them suitable in many areas of application. Although a large amount of research has been performed on the production of carbide ecoceramics, less attention has been given to oxide ones.

In this thesis the state of the art of the biomorphous oxide ceramics derived from lignocellulosic templates is discussed, mainly wood, pollen, fibers and petals. The hierarchical porous structure that the final products exhibit, and the positive consequences that this derives in their various fields of application, is also described. Biomimicking oxide materials have gained increasing attention thanks to their outstanding performance both in environmental and energy fields. They can be used as materials for photodegradation of pollutants both in air and water, energy conversion and storage, gas sensing, adsorption, photocatalysis, EM radiation shielding, biomedical applications and many others.

This thesis consists of seven chapters in which the most investigated oxides are described, and their most interesting applications are presented. Comparison analysis between results is performed and the possible explanation regarding the mechanisms and the enhanced performance is reviewed. Individual chapters illustrate TiO_2, CeO_2 and ZnO ecoceramics due to the large amount of research that has been carried out on these materials. Following this, the remaining biomorphous oxides derived from transition metals (vanadium, V; chromium, Cr; manganese, Mn; iron, Fe; cobalt, Co; nickel, Ni; copper, Cu; yttrium, Y; zirconium, Zr; tungsten, W) are described. The class of post-transition metals is presented in the subsequent section, focusing the attention on biomimicking ceramics of aluminium (Al), indium (In) and tin (Sn). Alkaline earth metal oxides, such as calcium oxide (CaO) and magnesium oxide (MgO), are treated in a separate chapter, while biotemplated ceramics derived from the metalloids (only silicon) are examined in the last part. Among all considered oxides, those presenting doping elements, both self-incorporated from the starting template and/or added in the precursor solution, are included in the various chapters based on the major component of the material.

In this thesis, future research directions for biomorphic porous materials are discussed in the different sections, trying to provide a comprehensive description of hierarchical porous ceramics and help to open new avenues towards the exploration and refinement of these products.

4.1 Biomorphous TiO_2-ceramics

Titanium oxide (TiO_2), also known as titania, belongs to the family of transition metal oxides and is one of the most heavily investigated materials able to catalyse reactions in presence of light, hence being considered a potential solution for energy production and environmental pollution. Thanks to its favourable electronic (it is a wide band gap semiconductor) and opto-electrochemical properties, it has been widely used in various applications such as pigments in paints and cosmetics, photocatalysts, sensor materials and electrodes of solar cells and lithium ion battery. [90] Its wide use is also favoured by its characteristics such as chemical stability, high reactivity under UV light irradiation, low cost and non-toxicity which makes it a suitable material also as a binder in many medicines. It has been shown to be effective in the destruction of micro-organisms such as bacteria and viruses, the photosplitting of water to yield hydrogen gas, clean-up of oil spills and control of odors, which makes it suitable for applications as an environmentally benign photocatalyst. [91-97]

Titania can be found in many different crystalline structures, but it is generally described as having three different polymorphs (Figure 15): rutile (tetragonal), anatase (tetragonal), and brookite (orthorhombic). [98] In all polymorphs, titanium cations are coordinated to six oxygen anions forming distorted TiO_6 octahedra which, in turn, are joined together by sharing edges or corners. Rutile is the more thermodynamically stable form of bulk titania but generally requires higher temperatures to form, while anatase and brookite are more stable at lower temperatures or when the crystal is nano-sized, due to their smaller surface energy. Comparison studies between equal sized particles showed that anatase, brookite, and rutile are stable when the size is less than 11 nm, from 11 nm to 35 nm, and greater than 35 nm respectively. [99] Often two or three forms of titania coexist in the same material.

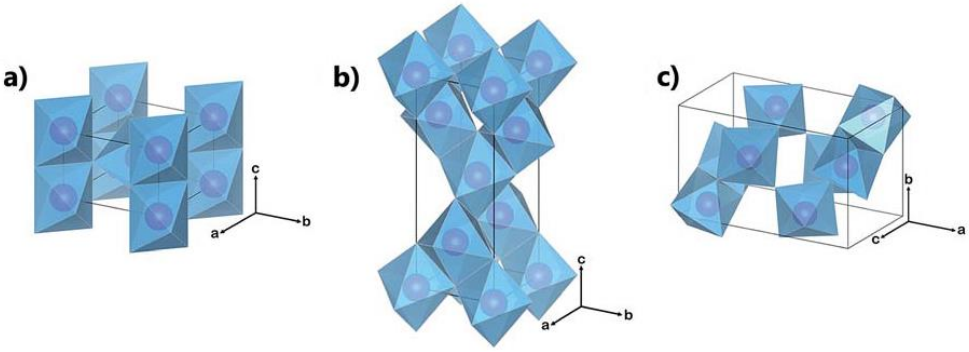

Figure 15 *- Polymorphs of titanuim dioxide: a) rutile, b) anatase, c) brookite [96]*

Heat treatment plays an important role for the optimal characteristics of titania. This process affects morphology and crystallinity of the final product, and causes a decrease in surface area, loss of surface hydroxyl groups and induces phase transformation of the TiO_2. The anatase-to-rutile transformation usually occurs irreversibly and exothermically in the range of 400–1200 °C depending on different parameters such as the atmosphere in the reaction chamber, method of preparation, grain size, morphology, degree of agglomeration of particles and the amount and nature of impurities. [100, 101] Impurities can have an accelerating or inhibiting action toward the conversion of anatase to rutile depending on their ability to enter the TiO_2 lattice. Their presence inside the crystal structure of titania can create oxygen vacancies or interstitial Ti^{3+} ions which tend to promote or retard the transformation, respectively. Tungsten and sodium ions, for example, have a pronounced inhibition ability whereas Sb, Ni, Fe, Co and Mn are capable to accelerate the transformation. [102-106] Another important parameter that affects phase transition temperature is the ionic radii of the impurities' cations: if the dopant possesses an ionic radius greater than, or similar to, the titanium atom, the anatase phase will be destabilized, while, on the contrary, when the impurity ion size is smaller than that of titanium, anatase will be stabilized. [107]

Table 1- Properties of TiO_2 in its different phases

Crystal structure	**Crystal system**	**Band Gap (eV)**	**Density (g/mL)**
Rutile	Tetragonal	3.02	4.13
Anatase	Tetragonal	3.20	3.79
Brookite	Orthorhombic	2.96	3.99

TiO_2 is a wide band semiconductor, with band gaps of 3.02 eV for rutile (visible light), 3.2 eV (UV range) for anatase and 2.96 eV (UV range) for brookite phase (Table 1). [108] Thanks to these ideal values, this material in known as the most efficient and environmental-friendly common photocatalyst. The principles behind its photocatalytic properties are as follows. [92, 96, 109] After the absorption of a photon with energy higher than the band gap of TiO_2, electrons are excited from the valence band to the conduction band, creating electron-hole (e-/h+) pairs (Figure 16a and Reaction 1). Thanks to the dissimilar parity between orbitals of conduction and valence band, these e-/h+ pairs do not recombine immediately and have enough time to migrate to the surface and react with the chemicals adsorbed there. In these conditions, electrons and holes possess the right potential to catalyse different important redox reactions (Figure 16b). Indeed, excited electrons in the conduction band have a potential equal to -0.52 V, which is negative enough to reduce oxygen to superoxide (Reaction 2). On the contrary, the holes in the valence band possess a redox potential of +2.53 V, which is sufficiently positive to form $OH^\bullet$ radicals through oxidation of adsorbed organic molecules or hydroxyl ions (Reaction 3). These latter are present in the environment from the natural dissociation of water (Reaction 4). It is also possible that electron-hole pairs will react with different adsorbed species depending on the environment. For example, if there is a high amount of adsorbed water, it is possible that more radical hydroxyls will form through the reaction of hydrogen peroxide as shown in reaction 5 and 6. Radical hydroxyls and superoxides are strong oxidants that can react with inorganic pollutants like NO_x and many organic molecules leading to the conversion these compounds into less harmful ones like CO_2, H_2O and mineral acids. [110]

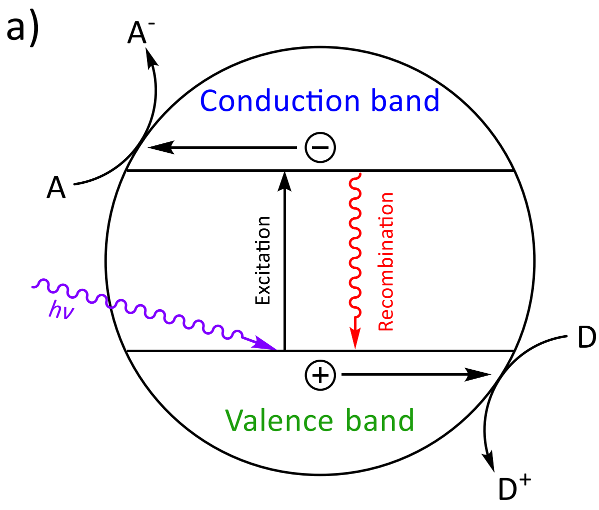

b)

1) $TiO_2 + \text{light} \longrightarrow TiO_2 + e- + h+$

2) $O_2 + e- \longrightarrow O_2^-$

3) $OH^- + h+ \longrightarrow OH^\bullet$

4) $H_2O \longrightarrow OH^- + H^+$

5) $O_2 + 2H_2O + 2e- \longrightarrow 2H_2O_2$

6) $H_2O_2 + e- \longrightarrow OH^- + OH^\bullet$

***Figure 16** – a) Schematic diagram of titania photocatalysis and b) reactions performed by TiO_2 after light exposure; where e− is an excited electron in the conduction band, h+ is a hole in the valance band, $OH^\bullet$ is a radical hydroxyl and O_2^- is a superoxide*

Important parameters affecting the photocatalytic efficiency of TiO_2 materials are crystallinity and specific surface area: the existence of an amorphous phase promotes e-/h+ recombination, thereby decreasing photocatalytic activity, whereas a larger surface area and the presence of anatase and rutile forms increases the reaction rate. [111] Due to this fact, anatase and rutile are the two main forms of titania on which studies are focused. This large interest derives from their peculiar structure and band gap values, which make them photocatalytically active after the absorption of photons with wavelengths smaller than 387 nm in the case of anatase, and smaller than 413 nm in the case of rutile. Although the latter is able to absorb light in the visible range, studies showed that the anatase phase possesses more photocatalytic efficiency. Indeed, e-/h+ pairs formed in the core of the anatase crystal can travel father than in rutile without suffering recombination. This phenomenon leads to more excited electrons and holes reaching the surface, therefore showing a higher photocatalytic activity. The ability of e-/h+ pairs to travel higher distances in anatase is due to the presence of different oxygen vacancies compared to rutile structure. In rutile, oxygen vacancies cause the formation of extra energy levels within the band gap in deep localized positions. On the contrary, in anatase oxygen vacancies give rise to shallow delocalized energy levels in the band gap, in addition to the deep ones. Since anatase has additional superficial energy levels, it has a higher e^- conductivity and the e-/h+ pairs have longer lifetimes than in rutile, as they are less trapped in the deep levels where the chance of recombination is higher (Figure 17). [112-114] The least photocatalytically efficient form of titania is the amorphous one. [115] The main reason for this low efficiency is because amorphous titanium dioxide has the greatest e-/h+ recombination capacity. The large number of defects present in the amorphous phase favour the recombination of electron-hole pairs, thus preventing the possibility of them reaching the surface of the titania. Moreover, conductivity in amorphous materials is very low since energy levels in this phase are much more localized. The high recombination rate and low conductivity means that only superficial electrons of TiO_2 manage to be excited by incoming electromagnetic radiation and take part in the photocatalytic activity in amorphous titania (Figure 17).

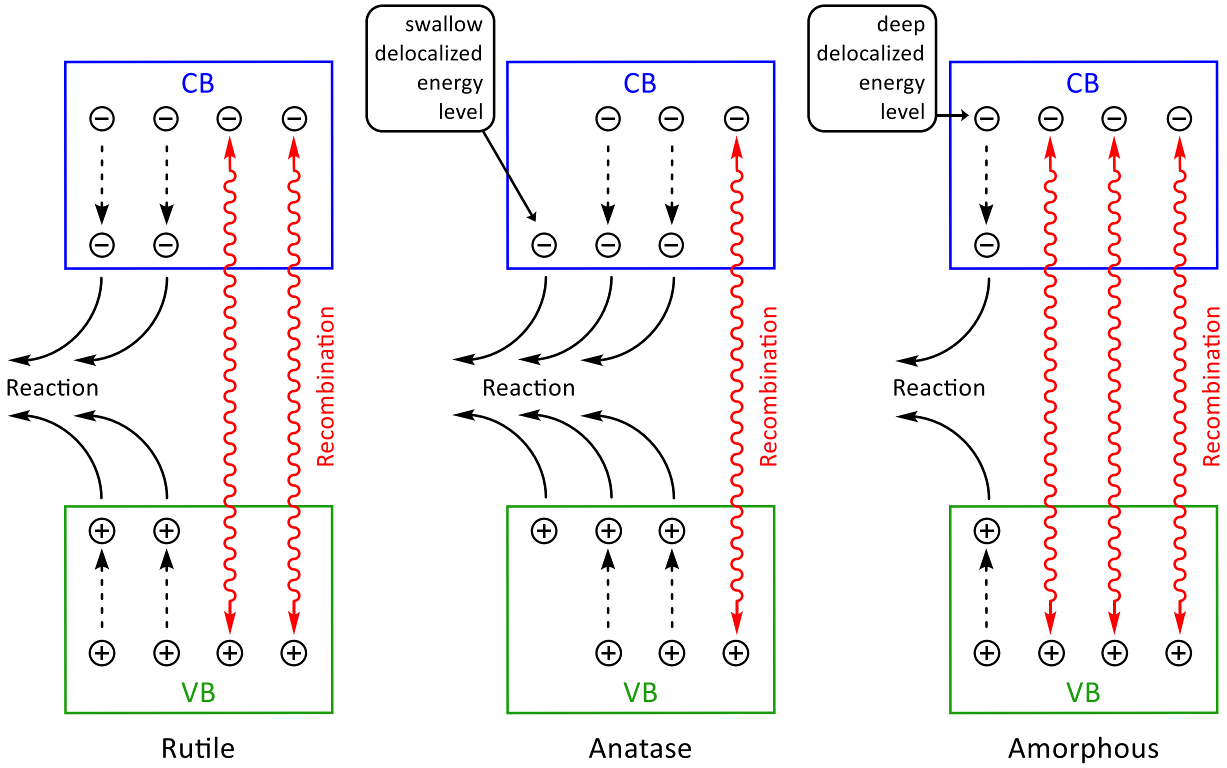

Figure 17 *– Schematic representation of e-/h+ recombination in different titania phases*

Studies have showed that titanium dioxide materials containing both rutile and anatase phases possess higher photocatalytic efficiency compared to only anatase form. Degussa P25 nanoparticles, which are commercial titania nanoparticles (NPs) made of around 20% rutile and 80% anatase and are often used as a benchmark material, have being greatly studied to understand their highly photocatalytic activity. [116] The conduction band of anatase has been measured to start at a lower energy level than that of rutile, even though its band gap is larger. Since electrons always go to the lower accessible energy state, when titania is composed of both phases, excited electrons from the conduction band of rutile will flow to the conduction band of anatase. On the contrary, holes, whose behaviour can be imagined as the opposite of electrons, will go from valence the band of anatase to the valance band of rutile because its edge is above the energy level of the valence band of anatase (Figure 18). Because excited electrons moves from rutile to anatase and holes from anatase to rutile, the recombination chance is reduced and a difference in electron density is produced at the interface between the two polymorphs, causing an increase in lifetimes and conductivity for the e-/h+ pairs, resulting in a higher photocatalytic activity. [117]

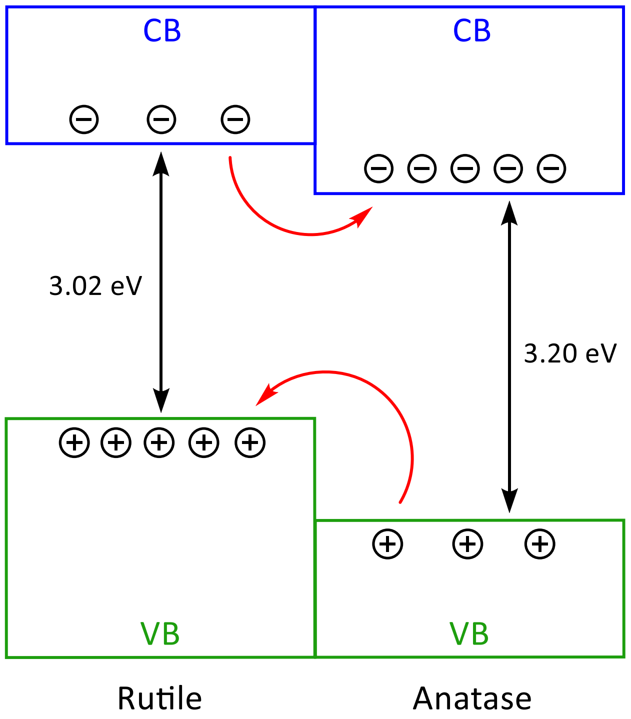

***Figure 18** – Schematic diagram for explanation of decreased electron-holes recombination in materials containing both rutile and anatase phases: excited electrons moves from rutile to anatase and holes from anatase to rutile*

An important class of titanium dioxide products are porous ceramics which are widely exploited thanks to their properties such as high specific surface area, biocompatibility and thermal insulation. Biomorphous titanium dioxide can be considered as a subcategory of such materials, since it usually exhibits these characteristics. In recent years, large efforts have been performed to convert natural templates into titania ceramics. Wood pieces, pollen grains and leaves have been used to produce hollow microspheres, open nanotubes and other porous materials showing optimal efficiencies in applications such as photodegradation of pollutants, catalytic oxidation reactions, hydrogen production, microwave absorption, enzyme immobilization and bactericidal applications (Table 2).

Table 2 – TiO_2-ceramics obtained using lignocellulosic-template biomimetic synthesis

Material	**Biotemplate**	**Morphology**	**Property**	**Ref**
TiO_2	Wood (Pine)	Highly porous	/	[118]
TiO_2	Wood (Pine, rattan)	Highly porous	/	[119]
TiO_2	Wood (Beech, mongoy, cherry)	Highly porous	/	[120]
TiO_2	Wood (Various)	/	/	[121]
TiO_2	Wood (Rattan)	Highly porous	/	[122]

Table 2 – Continued

Material	**Biotemplate**	**Morphology**	**Property**	**Ref**
TiO_2	Wood (Brich lumber)	Highly porous	Photodegradation of pollutants	[123]
TiO_2	Wood (Cedar)	Highly porous	Photodegradation of pollutants	[124]
WO_3/TiO_2	Wood (Poplar)	/	Photodegradation of pollutants	[125]
$CdS/Au/TiO_2$	Wood (Various)	/	Photocatalytic water splitting	[126]
$CdS/Ag/TiO_2$	Wood (Various)	/	Photocatalytic water splitting	[126]
$CdS/Pd/TiO_2$	Wood (Various)	/	Photocatalytic water splitting	[126]
$CdS/Pt/TiO_2$	Wood (Various)	/	Photocatalytic water splitting	[126]
TiO_2	Wood pulp sheets (cellulose)	Microfiber	Photodegradation of pollutants	[30]
TiO_2	Fibers (Bamboo)	Microfiber	Photodegradation of pollutants	[127]
TiO_2	Fibers (Jute)	Microfiber	/	[128]
TiO_2	Fibers (Cotton)	Hollow microfiber	/	[77]
TiO_2	Fibers (Cotton)	Hollow microfiber	Photodegradation of pollutants	[129]
$B+Ce/TiO_2$	Fibers (Cotton)	Hollow microfiber	Photodegradation of pollutants	[130]
TiO_2	Pollen (Sinicus)	Hollow microsphere	Photodegradation of pollutants	[131]
TiO_2	Pollen (Ambrosia trifida)	Hollow microsphere	Photodegradation of pollutants, oxidative storage of NOx	[132]
TiO_2	Pollen (Dandelion)	Hollow microsphere	Photodegradation of pollutants	[133]
TiO_2	Pollen (Rape)	Hollow microsphere	Photodegradation of pollutants	[134]
TiO_2	Pollen (Brassica oleracea)	Hollow microsphere	/	[76]
SnO_2/TiO_2	Pollen (Galla chinensis)	Nanoparticle, nanosheet, nanobelt	Photocatalytic reduction of Cr(VI)	[135]
Cu/TiO_2	Pollen (Rape)	Hollow microsphere	Photodegradation of pollutants	[136]
Pr/TiO_2	Pollen (Lotus)	Hollow microsphere	Photodegradation of pollutants	[137]
Gd/TiO_2	Pollen (Lotus)	Hollow microsphere	Photodegradation of pollutants	[137]

Table 2 – Continued

Material	Biotemplate	Morphology	Property	Ref
La/TiO_2	Pollen (Lotus)	Hollow microsphere	Photodegradation of pollutants	[137]
Pr + La/TiO_2	Pollen (Lotus)	Hollow microsphere	Photodegradation of pollutants	[137]
Pr + Gd/TiO_2	Pollen (Lotus)	Hollow microsphere	Photodegradation of pollutants	[137]
Gd + La/TiO_2	Pollen (Lotus)	Hollow microsphere	Photodegradation of pollutants	[137]
Pr + Gd + La/TiO_2	Pollen (Lotus)	Hollow microsphere	Photodegradation of pollutants	[137]
TiO_2	Leaves (Various)	/	/	[138]
N/TiO_2	Leaves (Various)	/	Photodegradation of pollutants	[139]
Pt + N/TiO_2	Leaves (Anemone vitifolia)	/	Photocatalytic water splitting	[53]
TiO_2	Petals (Rose)	Nanosheet	Photodegradation of pollutants	[140]
TiO_2	Petals (Rose)	Highly porous	Photodegradation of pollutants	[141]
TiO_2	Petals (Magnolia grandiflora)	Highly porous	Enzyme immobilization, biosensing	[142]

Nowadays, air and water pollution have become one of the biggest fears to humans due to the increasing discharge of waste chemicals into the environment. A large number of contaminants are dispersed every year, and, among them, dyes are a class of compounds that reach an annual spillage in waters of between 30,000 and 150,000 tons [143]. Rhodamine B (RhB) is a commonly used fluorescent tracer dye which is extensively employed in various fields and that could become a potential threat for the environment. RhB is in fact harmful to aquatic life with long lasting effects and degradation resistant ability. Therefore, new eco-sustainable and photoactive materials like natural biomimicking titania could be an optimal solution for the removal of this pollutant.

Various groups synthesized and tested the photodegradation ability of biomorphous TiO_2 obtained from different lignocellulosic templates (Table 3). Erdogan and Ozensoy [132] and He et al. [134] produced TiO_2 microspheres using two different pollen grains as the starting material: *Ambrosia trifida* pollens and rape pollens, respectively. Pollen grains are excellent candidates to be used as biotemplates because of the presence of more a resistant exine outer layer, which prevents excessive particle shrinkage and consequent breakage during thermal removal of the scaffold. Both the resulting particles showed a hollow structure that faithfully reproduced the original template even at micro and nano scale (Figure 19a), but with different specific surface areas which varies according to the calcination temperature that has been used. In fact, while the microspheres of He et al. calcined at 450 °C possessed a surface area of 96.2 $m^2 \cdot g^{-1}$, the particles in Erdogan and Ozensoy's study calcined at 800 °C, which obtained the slightly better photodegradation efficiency, had a surface area around 7-8 $m^2 \cdot g^{-1}$. This fact confirms that higher heating temperatures increase grain growth reducing the specific surface area. In addition, high temperatures enhanced anatase-to-rutile transformation. This fact was proved by the presence of only anatase phase in the former particles, while the latter exhibited a mixture of anatase and rutile (94.9% anatase and 5.1% rutile). These combined features explain the large photodegradation performances for both materials assessed at 95% and 100% against an RhB water solution after 120 minutes, respectively for He et al. (under UV irradiation provided by a medium-pressure 300W mercury lamp) and Erdogan and Ozensoy (under UVA irradiation provided by a 8W Sylvania UVA-lamp) microspheres (Table 3).

Extremely high photodegradation efficiency was obtained also in work of Kochkina et al. [30] with the use of wood pulp cellulose sheets as templates. In this study, TiO_2 samples were composed of mixtures of anatase and rutile with a ratio of 72% to 28%, respectively. The resulting degradation of RhB was assessed to be around 99% after only 15 minutes under UV irradiation provided by a high-pressure 250W mercury lamp, which correspond to extremely reduced times compared to previous works (Table 3). This fact shows how the anatase to rutile ratio largely affects the photodegradation activity, maybe even more than specific surface area. Moreover, Kochkina et al. hypothesize that the unique oblong-shaped morphology of their particles may act as nano-antennas by absorbing light quanta in the visible region more efficiently and, therefore, increasing the light harvesting process. Particle structure should hence be an important feature to be taken in consideration for the production of photocatalytic materials, together with crystal phases and specific surface area.

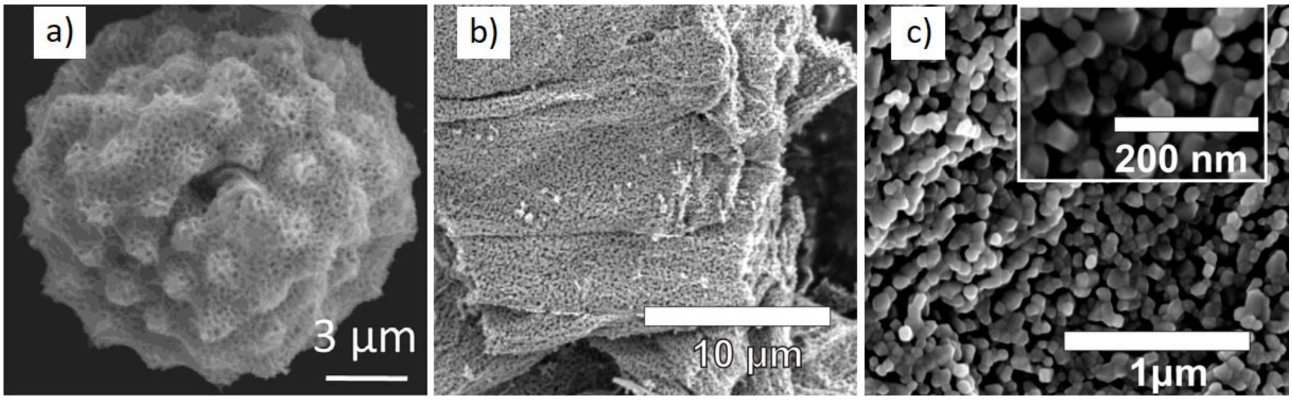

Figure 19 *– SEM images of a) Ambrosia trifida pollens-based TiO_2 microspheres [132] and b, c) wood pulp sheets-based TiO_2 particles [30]*

Outstanding performance against RhB pollutants have also been assessed with the use of doped titania nanoparticles, as in case of Gao et al. work. [125] In their study, the degradation of rhodamine B dye was performed with hetero-structured WO_3/TiO_2 catalysts obtained from poplar wood fibers through a two-step hydrothermal method and a calcination process. The resulting material possessed a composite structure made of WO_3 flowers deposited on the surfaces of pure anatase spherical particles (Figure 20). The presence of tungsten oxide led to a modification of the typical e-/h+ behaviour of TiO_2, expanding its light absorption ability in the visible region and reducing the electron-hole recombination. When the material was illuminated with appropriate light, electron-hole pairs were generated in both TiO_2 and WO_3. If the photons possess greater energy than titania's band gap (3.2 eV), the excited electrons that are formed in the valence band (VB) flow to the conduction band (CB) of TiO_2. Since the CB of WO_3 has a lower potential than the CB of TiO_2, electrons in the CB of titania transfer to the CB of WO_3. On the other hand, holes formed in the VB of WO_3 move to the VB of TiO_2, because of the higher potential that titanium oxide's VB has with respect to that of WO_3. If the incoming photon has a lower energy than titania's band gap but enough energy to overcome that of tungsten oxide (2.95 eV), a similar process occurs, with holes from the VB of WO_3 moving to the VB of TiO_2. The charge separation that arises in both cases reduces the possibility of e-/h+ recombination, thus increasing the photocatalytic activity of the material. In fact, this peculiar configuration, together with a relatively high specific surface area, led to the remarkable removal of 99.8% of RhB (under UV irradiation provided by a 500W ultraviolet lamp) after only 30 min, as reported in Table 3.

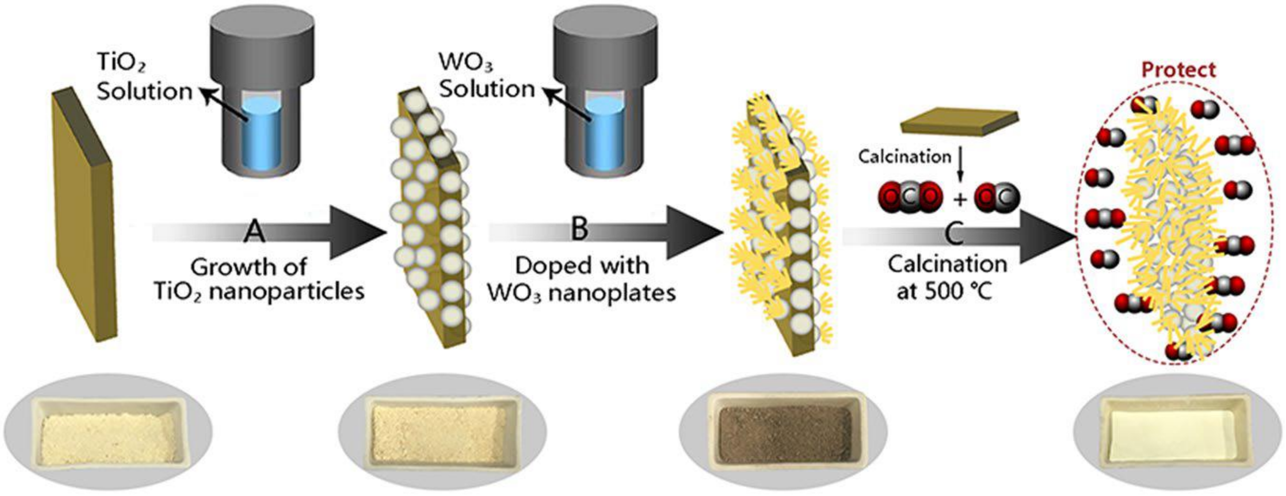

Figure 20 *– Preparation scheme of the WO_3/TiO_2 wood-derived fibers [125]*

Other titania ecoceramics have been tested against Rhodamine B showing good photocatalytic efficiency (Table 3). Li et al. [141] obtained a highly porous ceramic starting from rose petals, while Sun et al. [123] produced them using birch lumber wood as the initial support. Both compounds were synthesized through calcination at temperatures lower than 550 °C, and consequently obtaining only anatase as the crystalline phase. In the case of Li et al.'s study, TiO_2 flakes showed degradation of 73.2% of Rhb in 120 min (under UV irradiation provided by a 250W mercury lamp), while for the wood-derived titania it was found to be around 70% (under UV irradiation provided by a 100W ultraviolet lamp), as reported in Table 3. Even though both products strictly reproduced the template morphology, their degradation efficiency is lower than those presented before, confirming the hypothesis that the anatase to rutile ratio and multifaceted hierarchic structure are extremely important parameters for titanium dioxide materials operating in photocatalytic activities.

Table 3 – Photodegradation efficiency against RhB of TiO_2 ecoceramics under UV light irradiation

Biotemplate	Crystal structure	BET surface area ($m^2 \cdot g^{-1}$)	Removal efficiency (after 120 min)	Ref
Ambrosia trifida pollen	Anatase (94.9%) and rutile (5.1%)	7-8	100%	[132]
Poplar wood fibers	WO_3-doped TiO_2 (anatase)	92.95	99.8% (after 30 min)	[125]
Wood pulp sheets	Anatase (72%) and rutile (28%)	57.6	~99% (after 15 min)	[30]
Rape pollen	Anatase	96.2	95%	[134]
Rose petals	Anatase	125.91	73.2%	[141]
Birch lumber wood	Anatase	/	~70%	[123]

Degradation of a pollutant is not the only process which titania is capable of upon irradiation with an appropriate wavelength. A promising and environmentally friendly application of TiO_2 is the conversion of solar energy into chemical energy through the photocatalytic production of hydrogen. Hydrogen is gaining attention due to the possibility to be used as a clean and renewable fuel capable of resolving energy and environmental issues. [144] H_2 can produced by the splitting of water into its elemental components through the reaction reported in Scheme 8:

$$2H_2O \longrightarrow 2H_2 + O_2$$

***Scheme 8** – Water splitting reaction*

Pt/N-doped TiO_2 ceramics have been synthesized by the group of Zhou et al. [54] with outstanding performance in photocatalytic water splitting application starting from *Anemone vitifolia* leaves. In their work, authors reached to reproduce leaf morphology up to nanometer scale, obtaining artificial leaves capable to faithfully mimic the light harvesting behaviour of the internal architecture of leaf (Figure 21).

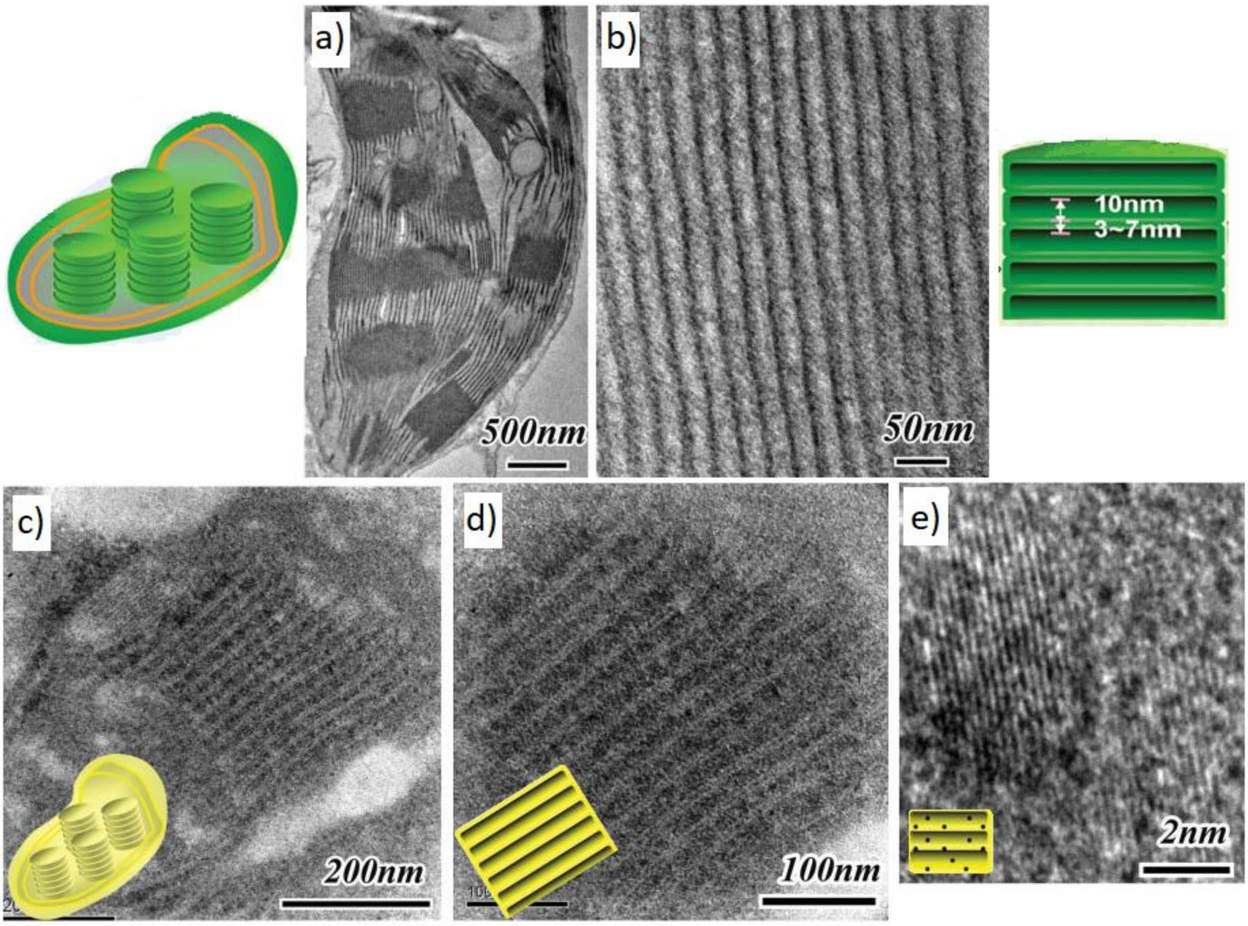

Figure 21 *– TEM images of a) a natural chloroplast, b) a natural thylakoid, c) an artificial TiO_2 chloroplast, d) an artificial TiO_2 thylakoid and e) a HRTEM image of Pt nanoparticles deposited on an artificial TiO_2 [54]*

Nitrogen self-incorporation and platinum doping lead to an increased photocatalytic activity in the overall splitting process (Figure 22a). Nitrogen presence generated an additional localized state beyond the valence band, inducing red shift of the bandgap absorption and thus expanding light capture even in the visible range. On the other hand, Pt, a noble metal, is well known to act as co-catalyst promoting charge transfer and creating hydrogen desorption sites which lead to higher photocatalytic activity for H_2 production. [145] When 2 wt% of platinum nanoparticles were directly formed onto the biomorphous TiO_2 leaves, the hydrogen evolution rate reached 1401.70 $\mu mol \cdot h^{-1}$ under UV-visible irradiation with xenon lamp in presence of 20% of methanol in the aqueous solution. Photocatalytic water splitting can in fact be enhanced in presence of methanol thanks to its sacrificial electron donor nature (Figure 22a). [146] Results obtained by Pt/N-doped TiO_2 biomimicking leaves were around 10 times higher than only N-doped artificial titania particles, and much more than 10 greater with respect to Degussa P25 (Figure 22b).

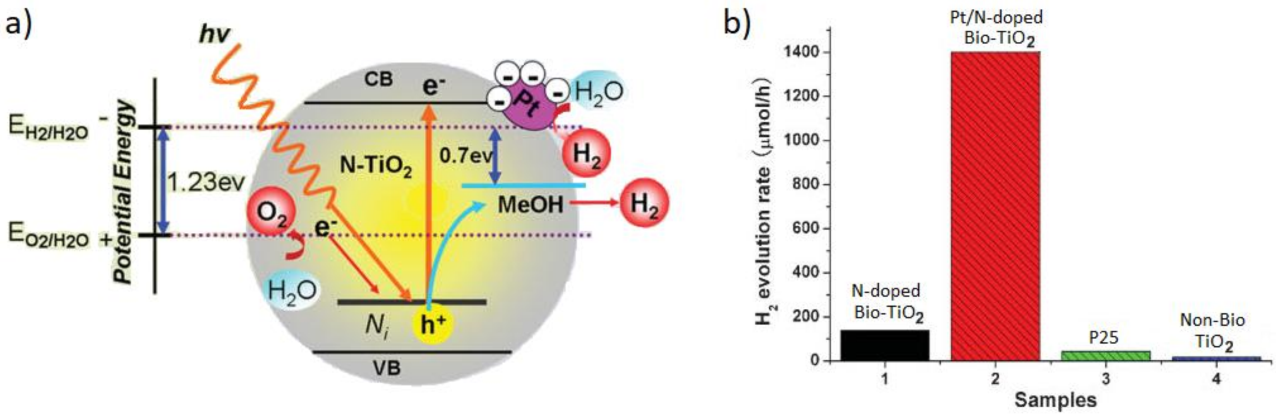

Figure 22 *– a) Schematic diagram of Pt/N-doped* TiO_2 *photocatalysis and b)* H_2 *evolution rates of tested samples [54]*

In another work of Zhou et al. group the photocatalytic hydrogen production was accomplished through the use of wood-derived hierarchical porous TiO_2 ceramics, on which have been deposited shell/core nanoparticles of CdS/M (M = Au, Ag, Pt or Pd). [126] After a typical substitutional process in which five different types of wood (softwoods: Fir, Ash and White Pine; hardwoods: Lauan and Shiraki) were converted into pure titanium dioxide ecoceramics, the photodeposition of 5 nm sized particles made of noble metals (Au, Ag, Pt or Pd) was performed, giving rise to M/TiO_2 products. For the photogeneration of CdS shells around a M core, initial S_8 preferential affinity to noble metal has been exploited. Subsequent electron accumulation on M nanoparticles led to a reduction of elemental S into S^{2-} ions, which in turn attracted Cd^{2+} ions and led to the formation of the final CdS shell *via* an ionic route (Figure 23e). Final CdS/M/TiO_2 production was confirmed by HRTEM images (Figure 23a-d).

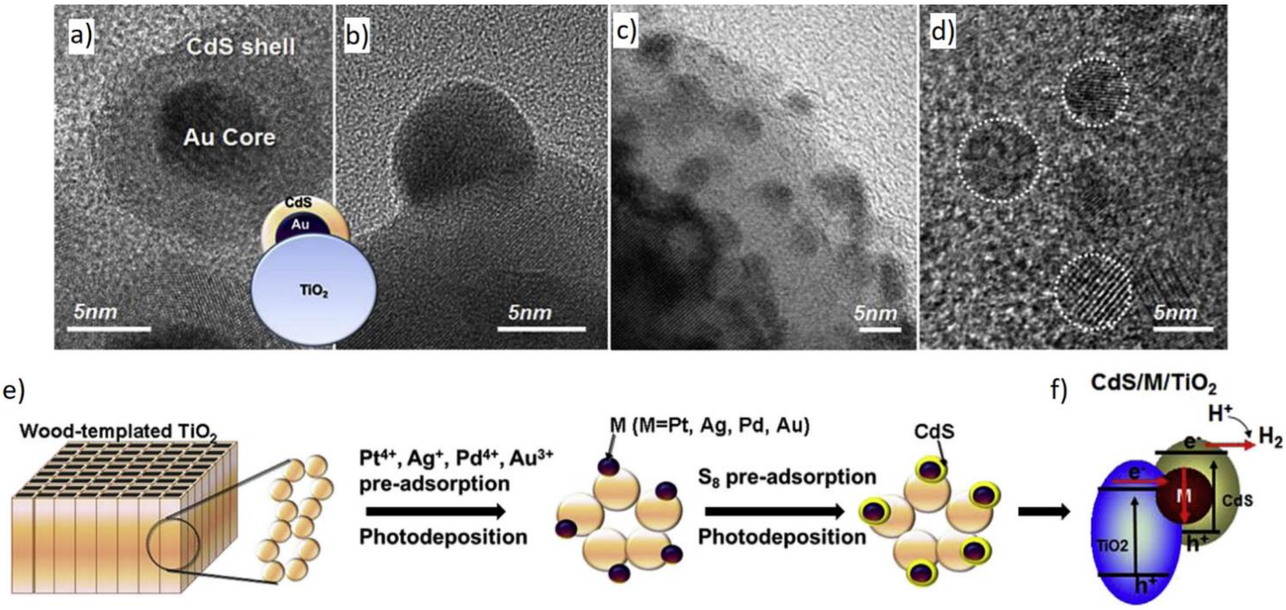

Figure 23 *– HRTEM images of a) CdS/Au/*TiO_2 *structure b) Ag/*TiO_2 *structure c) Pt/*TiO_2 *structure d) Pd/*TiO_2 *structure; e) Schematic illustration of a CdS/M/*TiO_2 *through a two-step photodeposition process; f) CdS/M/*TiO_2 *photocatalytic process [126]*

Photocatalytic water splitting for H_2 evolution was tested under UV-visible irradiation provided by a 750W xenon arc lamp, in the presence of methanol or Na_2S (0.25 M)-Na_2SO_3 (0.35 M) as the sacrificial agents. The authors found that the photocatalytic activity of wood-derived pure titania was already 1.5-7 times higher than that obtained using non-templated titania. This fact confirmed how the hierarchical porous structure can offer more absorption and reaction sites for the photocatalytic splitting. Moreover, since the pore size is comparable to the wavelength of the incident radiation (200-800 nm), the light could be scattered strongly along the forward direction (Mie's scattering) highly promoting its utilization and increasing the photoactivity. [147] Among all types of wood tested, hardwoods showed higher photocatalytic activity with respect to softwoods, even though their surface areas were comparable. This suggests that graded pores with wider distribution in size may be more favourable for reactant diffusion, thus promoting the efficiency. [126]

Photocatalytic tests performed with $CdS/M/TiO_2$ compounds resulted in an increase of the hydrogen evolution rate to around 700 times higher with respect to the best performing wood-derived pure TiO_2 ecoceramic ($CdS/Pd/TiO_2$: $\sim$325 $\mu mol \cdot h^{-1} g^{-1}$ against Shiraki-TiO_2: $\sim$0.45 $\mu mol \cdot h^{-1} g^{-1}$). The doping process allowed a more efficient charge transfer mechanism due to the core/shell structure of the additional nanoparticles (Figure 23f). Photo-generated electrons in the conduction band of titania easily flow into noble metals, while holes left in the valence band become accessible for oxidation reactions. Simultaneously, the holes in the valence band of CdS also move into noble metals recombining with the previously arrived electrons, and the electrons that reached the conduction band of CdS become available for reduction reactions. The resulting system realizes the complete separation of electrons in the conduction band of CdS and holes in the valence band of TiO_2, reducing the possibility of the charge carrier's recombination and resulting in higher photocatalytic activity. [148]

The hydrogen evolution rate of wood-derived $CdS/M/TiO_2$ products was, however, lower than that previously obtained using leaf-derived Pt/N-doped TiO_2 ceramics. This could be due to the intrinsic structure of the leaves which makes them more prone to harvesting light and for the higher specific surface area possessed by the leaf-derived titania with respect to that of the wood-derived products (83.25 $m^2 \cdot g^{-1}$ and 7.9-28.3 $m^2 \cdot g^{-1}$, respectively). Further research could be performed in order to assess if CdS doping onto Pt particles of leaf-derived TiO_2 materials could be feasible and possibly enhance the photocatalytic water splitting efficiency.

The complex morphology of leaves can similarly be found in plant petals and, hence, be used as a suitable template material. In the work of Xu et al. [142] magnolia grandiflora petals were exploited to prepare hierarchical porous titanium dioxide for the immobilization of horseradish peroxidase (HRP) enzyme. The use of this petal was ideal thanks to its peculiar superficial morphology, which allowed the production of lamellar titania nanoparticles with large surface area (60.5 $m^2 \cdot g^{-1}$) and exhibiting mesopores of average size around 10 nm. This pore diameter was calculated to be optimal for the accommodation of HRP molecules since its dimension in a neutral pH buffer was predicted to be around 6 nm. [149] UV-visible spectroscopy, FT-IR spectra and scanning electron microscopy analysis confirmed the correct incorporation of the enzyme in TiO_2 cavities without compromising its essential features (Figure 24). In fact, thanks to the pores' protective microenvironment, proteins did not undergo unfolding or conformational changing processes, thus maintaining their stability and activity. In addition to this, the authors demonstrated the possibility of preparing modified glassy carbon electrodes with HRP immobilized biomorphous-TiO_2 for the biosensing of hydrogen peroxide. The obtained biosensor showed good performance, displaying a low detection limit (0.87 µM), small Michaelis–Menten constant (223 µM), and wide linear range (1.0-524 µM). These results were an improvement compared to the performance of others H_2O_2 biosensors which employ different TiO_2 nanomaterials as an immobilization substrate. [150-154] The enhanced efficiency of the titania-based biosensor can be attributed to the unique structure derived from the template. More notably, in the confined space of the hierarchical porous structure, an increased chance of effective collisions between substrate and enzyme was present and the nanoparticles composing the pore walls could act as electron-transmitting wires, facilitating electron communication between the active site of HRP and the electrode. [155]

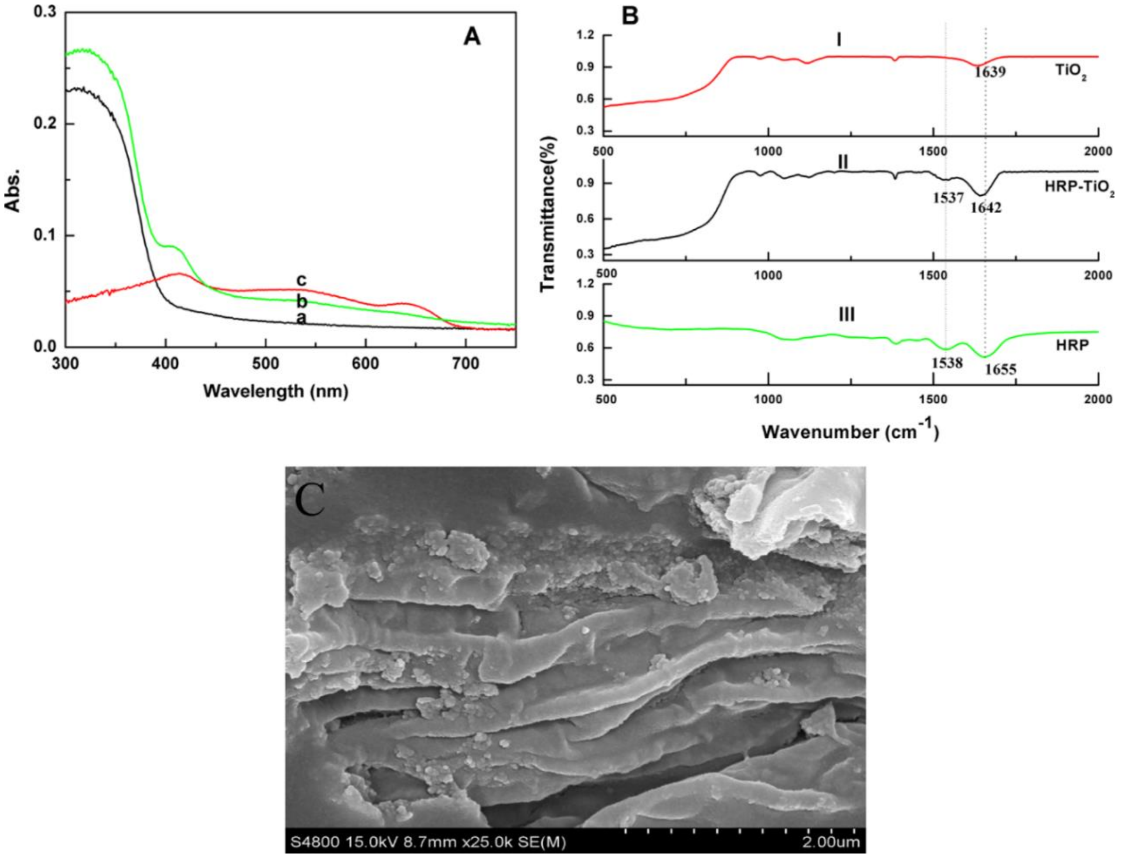

Figure 24 *– A) UV-visible spectra of a) bio-*TiO_2*, b) HRP immobilized on bio-*TiO_2*, c) HRP; B) FT-IR spectra of i) bio-*TiO_2*, ii) HRP immobilized on bio-*TiO_2*, iii) HRP; C) SEM of HRP immobilized on bio-*TiO_2 *[142]*

4.2 Biomorphous CeO_2-ceramics

Cerium oxide (ceria, CeO_2) has attracted vast attention thanks to its excellent redox properties [155] and interesting oxygen storage/release capacity [156]. The electron configuration of cerium is [Xe] $4f^2 6s^2$ with two common valence states: cerium (III) and cerium (IV). The high mobility of the oxygen species, the partial reduction of Ce^{4+} to Ce^{3+} and the unique fluorite-type configuration leads to the formation of many oxygen vacancies in the structure of CeO_2. These abundant oxygen vacancies result in the establishment of a new donor level below the cerium oxide's conduction band which narrows the bandgap and leads to a higher photocatalytic activity. [157] These characteristics make ceria a widely used material in applications like catalysis, [158] sensing, [159] electrolytes for solid fuel cells, [160] etc. Moreover, the recent possibility of using CeO_2 for thermochemical fuel production (TCFP), for example to split water and produce hydrogen or convert CO_2 into CO, has further increased the interest in this attractive compound. [42].

The physico-chemical properties of cerium oxides are strongly dependent on their microstructure, including size, morphology and specific surface area. Increased nanostructure of ceria leads to increased oxygen vacancies and higher catalytic activity, while its surface oxygens are found to be the active species that mostly contribute to the great performance of ceria. [161, 162] Large specific surface area and widely interconnected structures are thus desired to achieve good results in photocatalysis and thermal applications in environmental and energy-related fields. Natural biomimicking CeO_2 can possesses the peculiar highly porous structure which fulfils these characteristics. Biomorphic cerias have profiles showing surface oxygen reduction as the main reduction process, indicating enhanced surface oxygen activity. Moreover, their hierarchic porous structure raises the specific surface area of the ceramic material providing more surface sites for reduction of Ce^{4+} to Ce^{3+}, while at the same time facilitatating mass transfer, increasing the chemical activity of ceria. [163]

Table 4 - CeO_2-ceramics obtained using lignocellulosic-template biomimetic synthesis

Material	**Biotemplate**	**Morphology**	**Property**	**Ref**
CeO_2	Wood (Pine)	Highly porous	Thermochemical CO_2 splitting	[42]
CeO_2	Wood (Cork)	Monolithic 3-DOM	/	[164]
CeO_2	Wood (Cork)	3-DOM	Thermochemical CO_2 splitting	[165]
CeO_2	Wood (Cork)	Monolithic 3-DOM	/	[50]
$Ce_{0.9}Sr_{0.1}O_{2-\delta}$	Wood (Linden)	Highly porous	Radioactive ^{90}Sr storage	[166]
$Ce_{0.5}Zr_{0.5}O_2$	Wood (Spruce)	Highly porous	/	[167]
$Ce_{0.8}Zr_{0.2}O_2$	Wood (Pine sawdust)	Highly porous	CO oxidation	[168]

Table 4 - Continued

Material	Biotemplate	Morphology	Property	Ref
$Cu/Ce_{0.8}Zr_{0.2}O_2$	Wood (Pine sawdust)	Highly porous	CO oxidation	[168]
CeO_2	Fibers (Cotton)	Hollow microfiber	CO oxidation	[169]
CeO_2	Fibers (Cotton)	Hollow microfiber	Disel soot oxidation	[170]
Co_3O_4/CeO_2	Fibers (Cotton)	Hollow microfiber	Disel soot oxidation	[170]
CeO_2	Pollen (Lotus)	Hollow microsphere	Photodegradation of pollutant	[171]
Co_3O_4/CeO_2	Pollen (Lotus)	Hollow microsphere	Photodegradation of pollutant	[171]
N/CeO_2	Pollen (Lotus)	Hollow microsphere	Photodegradation of pollutant	[172]
N/CeO_2	Pollen (Hemerocallis)	Hollow microsphere	Photocatalytic water splitting	[173]
CeO_2	Leaves (Camphor and oleander)	Highly porous	/	[163]
$Ce_{1-x}Zr_xO_2$	Leaves (Tabacco)	Nanoparticle	CO oxidation	[174]
CeO_2	Petals (China rose)	Nanosheet	/	[175]
N/CeO_2	Petals (Field poppy)	Nanosheet	Photocatalytic water splitting	[157]

Various biotemplates have been exploited to produce cerium oxide materials and the resulting products have been tested in different fields of applications. Malonzo et al. [42] reported the production of porous CeO_2 starting from white pine wood pieces of dimensions 0.5 cm × 0.5 cm × 4 cm. White pine belongs to the softwood class, with a cellular structure composed mainly of long parallel channels forming the tracheid cells. These cells run along the direction of the tree trunk and branches, presenting diameters around 20−50 µm and wall thicknesses between 1 and 10 µm. The resulting ceramics, obtained after infiltration and heating treatment between 450 °C and 1500 °C, retained the original feature dimensions of the wood template at any calcination temperature, showing closure of only the smaller micro and mesopores but maintaining the inner open network (Figure 25a). Slight shrinkage in the pore diameter at sintering temperature of 1400 °C occured (typical pore diameter in the 15-20 µm range), while a total collapse in the channel structure at 1500 °C happened (albeit keeping the open cell composition). Increased heating temperature also led to larger grain growth, up to 5 µm in CeO_2 calcinated at 1400 °C and approaching the wall dimensions in the 1500 °C case. As a consequence, grain growth was accompanied by a reduction of the active surface area from 74.0 $m^2 \cdot g^{-1}$ of wood treated at 450 °C to values lower than 0.05 $m^2 \cdot g^{-1}$ for the sample treated at 1500 °C.

Thermochemical redox cycles for the production of CO have been tested for these materials. CO_2-splitting cycles consist of two separate thermochemical reactions: a high-temperature (endothermic) reduction (Scheme 9a) and a low-temperature (exothermic) oxidation (Scheme 9b). Reduction proceeds through the formation of oxygen vacancies and the release of gaseous O_2, causing a stoichiometry alteration of cerium oxide (CeO_{2-x}). Oxidation occurs with CO_2 action, through the release of CO and the reincorporation of oxygen into the lattice. During all these cycles, the number of oxygen vacancies created in the first step is directly related to the yield of fuel production that can be achieved. [176].

$$\text{a)}\ CeO_2 \longrightarrow CeO_{2-x} + \frac{x}{2} O_2$$

$$\text{b)}\ CeO_{2-x} + x\,CO_2 \longrightarrow CeO_2 + x\,CO$$

$$\text{Net reaction:}\ x\,CO_2 \longrightarrow x\,CO + \frac{x}{2} O_2$$

Scheme 9 *– CO_2 splitting reaction*

In the Malonzo et al study [42] the cycling behaviour of the biomorphous CeO_2 was steady over 21 reduction/oxidation cycles for all tests, without any observable changes in sample morphology of the heat-treated materials after cycling. Total CO production increased with reduction temperature, reaching 2.1 $mL{\cdot}g^{-1}$ (~85 $\mu mol{\cdot}g^{-1}$) after reduction at 1400 °C and 2.5 $mL{\cdot}g^{-1}$ (~102 $\mu mol{\cdot}g^{-1}$) after reduction at 1500 °C. These results were respectively four times, and nearly twice, those obtained using nonporous ceria cycled under the same conditions. Despite the good results obtained by Malonzo et al., the final ecoceramic still presented a fragile composition with performance lower than other materials reported in the literature [177].

In this context, another research that showed promising results in thermochemical CO_2 splitting through the use of cork templated biomorphic ceria ecoceramics was that of Oliveira et al. [165] CeO_2 compounds were synthesized starting from cork wood and cycled in a high-temperature indirectly-irradiated solar tubular reactor under real and temporally-variable solar irradiation conditions using a temperature-swing process. Samples were typically reduced at 1400 °C using concentrated solar power as a heating source and subsequently oxidised with CO_2 between 1000–1200 °C.

Natural cork has similar internal configuration to pine wood used by Malonzo et al. [42] with elongated hexagonal cells of 40–50 µm length and 20 µm in diameter. Cell wall thickness is around 1 µm, smaller than that of white pine, and cork presents a more regular 3-DOM (three-dimensionally ordered macroporous) microstructure, and hence appears to be a more suitable template material. Cork-template based-ceria granules were produced through a typical substitution process, in which previously pyrolyzed wood was infiltrated with cerium nitrate solution and heated in air up to 1600 °C for 30 min to remove the carbon and leave the substitutive cerium oxide ceramic (Figure 25b).

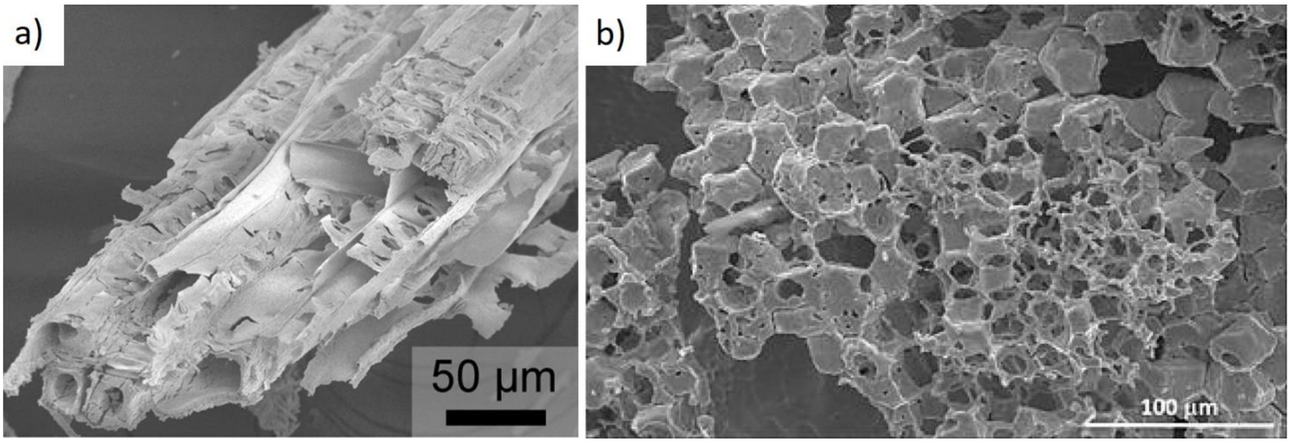

Figure 25 *- SEM images of a) white pine-derived* CeO_2 *[42] b) Cork-derived* CeO_2 *[165]*

The amounts of CO produced during the CO_2-splitting step using bio-based ceria were as high as ∼200 $\mu mol \cdot g^{-1}$ and the CO production stability was maintained during cycling. Although appreciable grain growth occurred during thermal cycling, its effect on the reaction kinetics, fuel productivity and cyclical stability was negligible over the 11 cycles studied. The CO yield of cork-templated ceria was found to be about twice that of its control ceria foam counterpart, and also twice that calculated by Malonzo et al. for pine-derived CeO_2. [42] Processing of ceria ecoceramics must be optimised to fully replicate the wood structure and develop materials having high surface area based upon interconnected pore network, which must be retained over many thousands of cycles and hours of operation at temperatures over 1400 °C. Moreover, to improve resistance and the usability of these materials over time, investigations made to minimise grain growth are required, for instance through the doping of CeO_2.

A doping process has been performed in various studies to improve the properties of cerium oxide. An example is the photoinduced water-splitting for hydrogen production obtained in the study of Qian et al [157]. For the conversion of H_2O in its molecular component ultra-thin (<5 nm) N-doped CeO_2 nanosheets were fabricated with the assistance of field poppy petals. Figure 26a shows the production process for ceria nanosheets: the conical epidermal cells of the petals were first impregnated with cerium nitrate solution, then the membrane was embossed with Ce^{3+} ions and finally calcination followed by cooling gave rise to separated layers of CeO_2. The nitrogen contained in the plant corpus is self-doped into the nanosheets, thus generating N-doped CeO_2 films faithfully reproducing the biomorphic microstructure of the original template. A possible mechanism for light-driven water reduction to produce H_2 is also illustrated. Under suitable light irradiation (band gap of ceria being 3.19 eV), the photoinduced electrons transfer from valence band to midgaps, which are generated from the shallow donor level below the conduction band (caused by oxygen vacancies) and deeper energy levels (caused by substitutional N atoms). The electrons could then use longer wavelength light to move to the conduction band. This configuration prevents the recombination of the electron-hole pairs and increases the reaction efficiency, also improved by the wider visible light absorption caused by the presence of nitrogen atoms. Eventually, the water molecules could accept electrons from the conduction band and form hydrogen. [157]

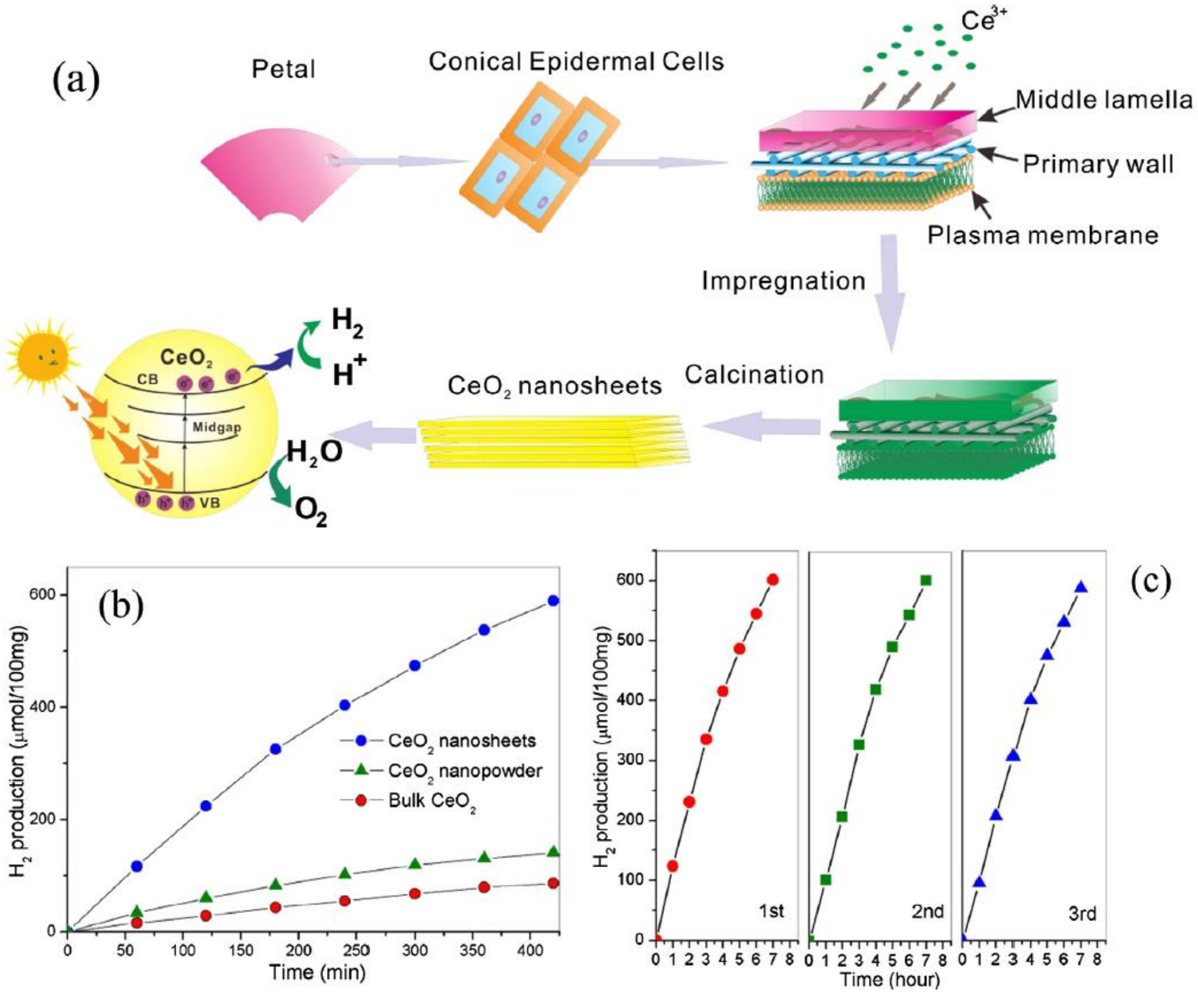

***Figure 26** - a) Proposed mechanism for the formation of CeO_2 nanosheets; b) H_2 production over time; c) Recycled ceria nanosheets tests for hydrogen production [157]*

Figure 26b presents the cumulative H_2 production obtained from biomorphous CeO_2 nanosheets, non-biotemplated CeO_2 nanopowders and bulk ceria, under UV-visible irradiation provided by a 300W xenon lamp and in presence of 20% of methanol in the aqueous solution. Of these three photocatalysts, the highest activity for H_2 evolution has been noted for biomorphic CeO_2 nanosheets at ~842 $\mu mol \cdot h^{-1} \cdot g^{-1}$, which are far superior to the other samples. In addition, recyclability tests were performed to confirm the stability and durability of ceria nanosheets and their result are presented in Figure 26c. During three repeated cycles employing the same biomimicking material, the water-splitting reaction produced approximately similar quantities of H_2, indicating that the as-prepared material is an excellent photocatalyst.

Therefore, the doping process has demonstrated the outstanding possibility to enhance material properties even in the case of bio-templated materials. Another confirmation of this came from the works of Qian et al. [172] and Liu et al. [171]. Both studies synthesized biomorphous ceria nanoparticles using lotus pollen as a starting template, and doping them with nitrogen and cobalt, respectively. In both works, infiltration with a precursor solution and calcination at 550 °C led to the formation of hollowed microspheres retaining the external structure of the pollen grains (Figure 27), but showing smaller dimensions (from an initial 50 µm to 10-15 µm for N-doped CeO_2 and ~25 µm for CeO_2/Co_3O_4), and the formation of pores with different average diameters (5 nm for N-doped CeO_2 and 10 nm for CeO_2/Co_3O_4).

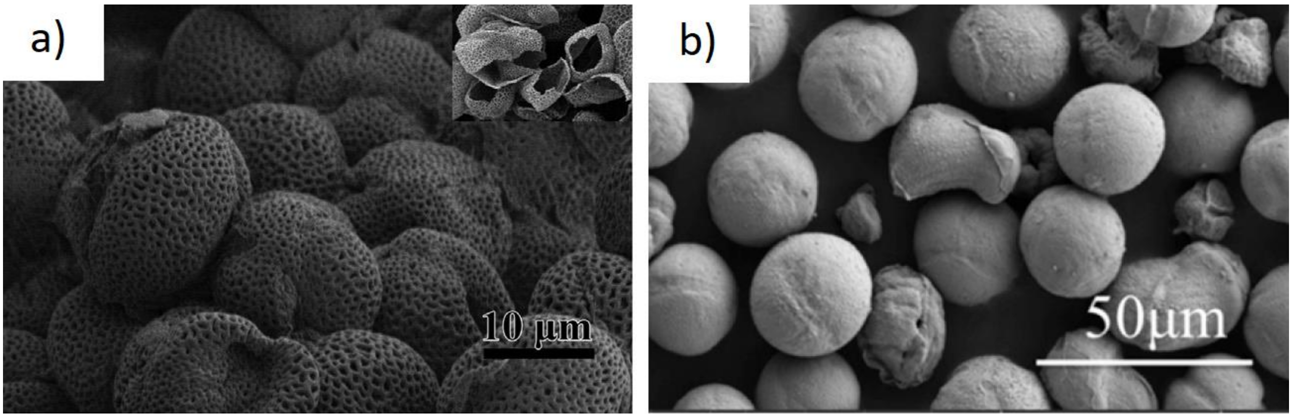

Figure 27 *– SEM images of a) N-doped* CeO_2 *microspheres (the inset image reveals cracked grains) [172] and b)* Co_3O_4*-doped* CeO_2 *nanoparticles [171]*

To assess the new properties of the resulting ecoceramics, their photocatalytic activity was evaluated through the degradation of methylene blue (MB) in water solution. Qian et al. [172] studied batch removal of the dye under direct sunlight irradiation, using 100 mg of photocatalyst uniformly dispersed in 400 mL of a 20 $mg \cdot L^{-1}$ MB aqueous solution and previously stirred in the dark for 60 min to establish adsorption equilibrium. Liu et al. [171] instead investigated the photodegradation process by adding 30 mg of ceria ecoceramic to a 100 ml solution with 20 $mg \cdot L^{-1}$ concentration of MB and using a xenon lamp as simulated light, after keeping it in the dark under stirring for 30 minutes. Thanks to the hierarchical structure of CeO_2, which allows multiple reflections of UV light enhancing light-harvesting and increasing the quantity of photogenerated electrons and holes available to participate in the photocatalytic degradation of methylene blue, both types of nanospheres showed higher photodegradation ability compared to bulk ceria.

In the case of N-doped cerium oxide, the presence of interstitial nitrogen atoms in the CeO_2 lattice and molecular chemisorbed nitrogen on the materials surface induced a red-shift in its ultra-violet absorption curve of more than 30 nm, increasing the absorption in the visible region. This characteristic led to the removal of over 80% of methylene blue within 120 min of visible light irradiation. On the other hand, during the study of photocatalytic activity of biomorphous Co_3O_4-doped CeO_2 microspheres, the doping process with Co enhanced the electron transfer from CeO_2 to Co_3O_4 and increased the overall photocatalytic efficiency. For Co_3O_4/CeO_2 microspheres, the degradation of MB was higher compared to that of pure cerium oxide nanoparticles also produced using a pollen template, reaching rates above 95% within 90 min against that below 50% for pure CeO_2.

It is difficult to truly compare the results obtained from the two abovementioned works, since they were not performed under the same conditions. In fact, even though Co_3O_4-doped CeO_2 nanoparticles presented an increased dye removal performance in less time compared to N-doped CeO_2 microspheres, this test was performed with larger amount of catalyst (30% w/v against 25% w/v) and under more controlled irradiation than the Qian et al. work.

Besides water pollution, air contamination is also considered one of the main concerns of the current environmental crisis. For example, soot emissions constitute one of the main sources of air pollution, diesel engines being the ones that contribute the most. [178] To decrease the concentration of the harmful soot particles the use of diesel particulate filters (DPF) is an effective solution. The application of ceramic ceria fibers in DPF has been demonstrated to be an optimal alternative for soot oxidation, probably due to the highly interconnected network of fibers enhancing the number of contact points of pollutants with the catalyst itself. [179] Stegmayer et al. [170] realized the biomorphic synthesis of CeO_2 and mixed CeO_2-Co_3O_4 microfibers using cotton as biotemplate and employing them as catalysts for the diesel soot oxidation reaction. While the preparation of pure ceria fibers followed the usual impregnation of cotton in cerium nitrate solution and subsequent calcination steps, Co_3O_4/CeO_2 microfibers were produced with two different methods. One proceeds through infiltration of a solution of cerium and cobalt nitrate into the template followed by heating in air. The other involved a wet impregnation method using previously prepared biomorphous ceria fibers as a support (sequential synthesis). To this end, an aqueous solution of the cobalt precursor was prepared and then CeO_2 fibers were added and afterwards calcined. All samples were hollow and micrometer size (~10 µm diameter), formed by bundles of smaller fibers. After the incorporation of cobalt by wet impregnation, the fiber morphology was maintained, but some of them appear broken and with greater heterogeneity than the samples prepared with single infiltration. CeO_2 fibers presented a BET surface area of 16 $m^2 \cdot g^{-1}$, while mixed fibers prepared by the one step method showed lower values of 7 and 11 $m^2 \cdot g^{-1}$ depending on the amount of Co used during synthesis (2% w/w and 12% w/w respectively). Co_3O_4/CeO_2 microfibers prepared by the sequential synthesis showed similar BET surface area values to that obtained for CeO_2 fibers (16 $m^2 \cdot g^{-1}$ for 2% w/w of Co and 18 $m^2 \cdot g^{-1}$ for 12% w/w of Co). Another interesting characteristic that was observed in these materials through X-ray photoelectron spectroscopy (XPS) was the difference in O_β/O_α ratio (Figure 28a). O_β is the chemical absorption related to surface oxygen species whereas O_α is that related to lattice oxygen. Mixed Co_3O_4/CeO_2 fibers resulted in a higher O_β/O_α ratio then pure ceria fibers (0.29-0.35 against 0.26), implying better catalytic performance of the doped material with respect to the pure one. Labile adsorbed oxygen species (O_β) are, in fact, more active than lattice oxygen (O_α) due to their higher mobility. This is the reason why these species always play a key role in catalytic oxidation reactions [180, 181].

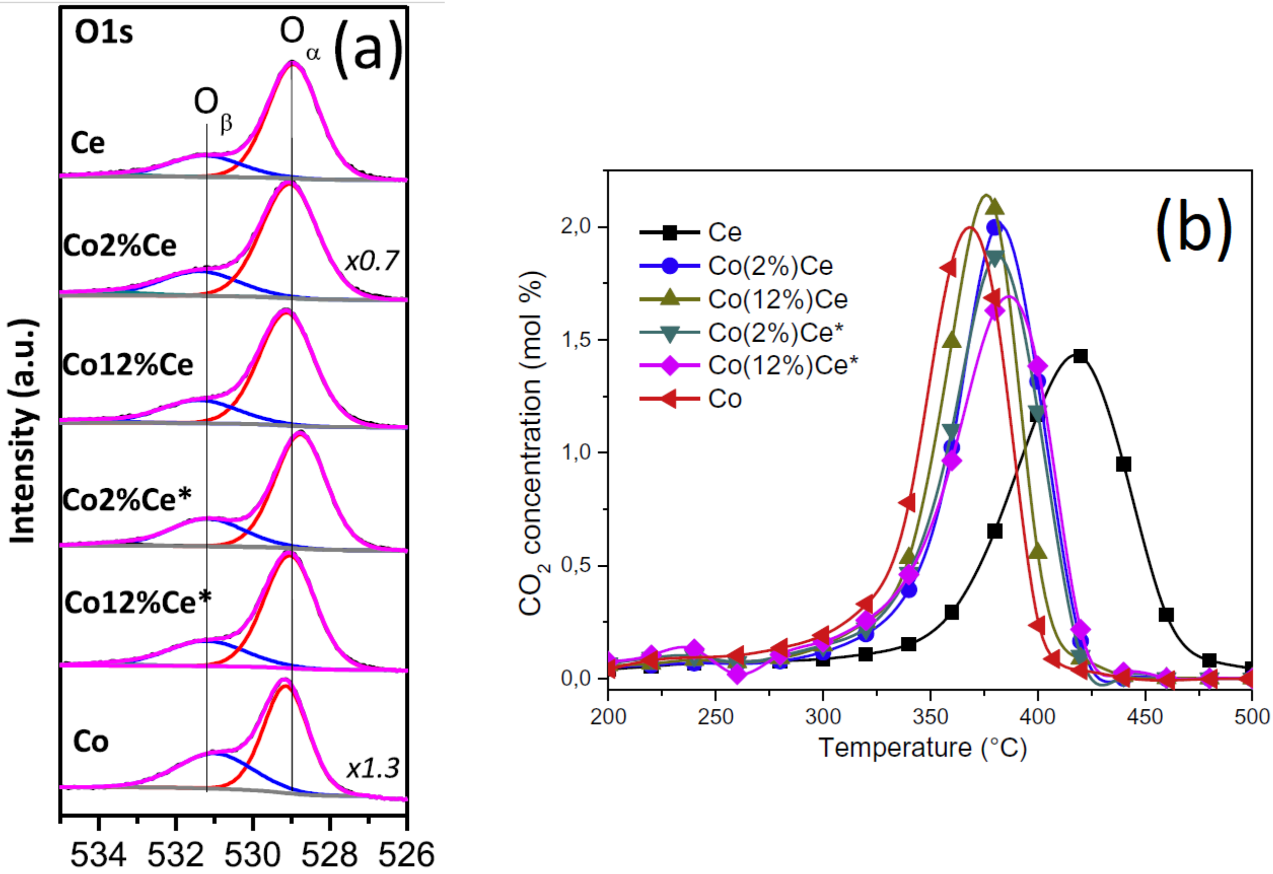

Figure 28 *–a) XPS spectra of oxygen signals in the various CeO_2 and Co_3O_4/CeO_2 biomimicking samples; b) Results of temperature programmed oxidation experiments (the asterisk refers to samples synthesized with one step method) [170]*

Results from temperature programmed oxidation experiments (TPO) confirmed the better efficiency of the Co_3O_4/CeO_2 fibers against ceria ones (Figure 28b). Keeping in mind that the lower the temperature for the maximum combustion rate (T_M), the better the catalytic performance, mixed microfibers showed T_M values at around 380 °C (irrespective of the method of incorporation of cobalt or its content), while pure CeO_2 samples obtained T_M equal to 420 °C. However, these results were still worse than those achieved using pure Co_3O_4 nanofibers prepared with the same method (Figure 28). These fibers, even though they showed the smallest specific surface area (2 $m^2 \cdot g^{-1}$), possessed the highest O_β/O_α ratio (0.55) and presented a T_M value of 365 °C, a temperature among the lowest reported in the literature until now. These facts suggest that the availability of O_β species is even more important than surface area during soot oxidation. Realistic reaction condition tests are required to assess if these materials could maintain their efficiency and stability over time.

4.3 Biomorphous ZnO-ceramics

Zinc oxide (ZnO) is a ceramic material with unique physical and chemical properties such as low cost, high chemical stability, high redox potential, nontoxicity, and environmentally friendly features. [182] It is classified as an *n*-type semiconductor with a band gap of 3.37 eV, which gives it interesting optical, semiconducting and photocatalytic properties. [183] ZnO can absorb a wide fraction of the UV spectrum, making it a great competitor of TiO_2 in photocatalysis. The position of the valence band of zinc oxide is lower than that of titania; therefore, the oxidation potential of hydroxyl radicals generated by ZnO is larger, and thus its potential photocatalytic performance is generally better than that of TiO_2. However, the large bang gap, the fast recombination of photogenerated e-/h+ pairs and the typical photocorrosion that ZnO undergoes in aqueous solution during UV irradiation do not make it such an efficient photocatalyst in real applications, such as wastewater treatment. [184]

The most common structure of zinc oxide that can be found in nature is wurtzite. It is the most thermodynamically stable configuration of all ZnO structures, consisting of hexagonal-close-packed sub-lattices composed of alternating atomic planes of Zn^{2+} ions and O^{2-} ions. This pattern can give rise to intrinsic defects in the crystal structure, creating oxygen vacancies (V_o) which can lead to the variation of the normal stoichiometry and the appearance of n-type conductivity. [185] Oxygen vacancies are of extreme importance in applications like chemical sensing of harmful vapours, making zinc oxide one of the most promising materials in this field.

Because of all these diverse properties, zinc oxide is widely used in many areas that range from tyres to ceramics, from agriculture to electronical industry, and from paint to pharmacology. [186] Indeed, ZnO finds applications as an antibacterial agent, thanks to its high thermal stability, excellent antimicrobial activity and good biocompatibility. The antimicrobial action of ZnO against bacteria is more effective when zinc oxide particles are reduced to nanoscale size. [182] Structures at micro and nano levels are, in fact, mostly investigated to obtain enhanced performances in all kind of technologically advanced applications.

By using natural biological compounds as templates, an astonishing variety of sophisticated micro and nano architectures can be transformed into inorganic ZnO ceramics. These materials take advantage of the hierarchical structure of the original sacrificial guide to exhibit enhanced performances in all their various field of application. Different lignocellulosic templates such as wood, pollen, leaves and cotton have been exploited to synthesize porous and elaborate ZnO ceramics with improved results, mainly in gas sensing and photocatalytic applications (Table 5).

Table 5 - ZnO-ceramics obtained using lignocellulosic-template biomimetic synthesis

Material	Biotemplate	Morphology	Property	Ref
ZnO	Wood (Fir)	Highly porous	Cathodoluminescence properties	[187]
ZnO	Wood (Lauan and Fir)	Highly porous	Gas-sensing	[188]
ZnO	Wood (Cork)	3-DOM	Photodegradation of pollutant	[189]
ZnO	Wood (Larch and Lauan)	3-DOM	/	[190]
ZnO	Fibers (Jute)	Nanoparticle	Photodegradation of pollutant	[191]
ZnO	Fibers (Cotton)	Hollow microfiber	/	[192]
ZnO	Fibers (Cotton)	Hollow microfiber	Photodegradation of pollutant	[193]
ZnO	Fibers (Banana steam fibers)	Nanowire	Photodegradation of pollutant	[194]
CeO_2/ZnO	Fibers (Banana steam fibers)	Nanowire	Photodegradation of pollutant	[194]
In_2O_3/ZnO	Fibers (Cotton)	Hollow microfiber	Gas-sensing	[195]
CeO_2/ZnO	Fibers (Cotton)	Hollow microfiber	Gas-sensing	[196]
$ZnMn_2O_4$	Fibers (Cotton)	Microbelts	Lithium-ion batteries	[197]
ZnO	Pollen (Sunflower)	Hollow microsphere	Gas-sensing	[198]
ZnO	Pollen (Lotus)	Hollow microsphere	Photodegradation of pollutant	[199]
Co_3O_4/ZnO	Pollen (Lotus)	Hollow microsphere	Photodegradation of pollutant	[199]
ZnO	Leaves (Zamioculcas zamiifolia)	Highly porous	Photodegradation of pollutant	[200]
Co/ZnO	Leaves (Zamioculcas zamiifolia)	Highly porous	Photodegradation of pollutant	[200]
Ni/ZnO	Leaves (Zamioculcas zamiifolia)	Highly porous	Photodegradation of pollutant	[200]
Ag-AgCl/ZnO	Leaves (Poplar)	Highly porous	Photodegradation of pollutant	[201]
NiO/ZnO	Leaves (Poplar)	Highly porous	Gas-sensing	[202]
N/ZnO	Leaves (Various)	/	Photodegradation of pollutant	[203]

In recent decades, indoor and outdoor air pollution is becoming a serious problem that requires careful monitoring to not cause harm to both the environment and humans. The most common dangerous gasses of interest are CO, NO_x, H_2S, CO_2 and CH_4, together with other volatile organic compounds (VOCs) such as acetone, ethanol, n-butanol and benzene. [204] The precise detection of these vapours is of extreme importance especially because of the toxicity that some of them can assert, even at parts-per-million (ppm) quantities. Therefore, the production of gas sensors with very high sensitivity and selectivity is of extreme importance.

Gas sensing bases its functioning on the change of resistance that the material undergoes in the presence of different types of gas, when connected in an electric circuit. When pure air flows through the sensor, oxygen molecules absorb onto its surface and, due to the electron-attractive nature of oxygen, a depletion of electrons from the circuit occurs, and a larger resistance is detected (R_a). When, instead, the sensor surface interacts with an oxidising or reducing gas, an increase or decrease in resistance is respectively reported (R_g). This change in the resistance is the sensing signal. The whole process is schematically shown in Figure 29.

The important parameters that characterize the performance of a gas sensor are: sensitivity (S, defined as the ratio of change in sensor signal to the original signal), response and recovery time (τ_{res} and τ_{rec}, defined as the time required to change from original state to the gas ambient state, and vice versa), limit of detection (LOD, defined as the lowest amount of target gas for which the sensor can show a response), optimum working temperature (defined as the temperature at which the sensor gives the best response) and selectivity (determined by how the sensor responds to the target gas compared to other gases). [185]

Porous ZnO has been shown to be a promising material for gas sensing thanks to the presence of a large number of adsorption sites and oxygen vacancies (V_o) in its structure. Indeed, porous products usually present the high specific surface areas which are optimal for the adsorption of gasses. Moreover, various studies performed into the detection of NO_2 suggested that V_o in ZnO composites could serve as active sites for the chemisorption of the target gases, therefore being one of the most important factors enhancing the ZnO gas sensing response. [205]

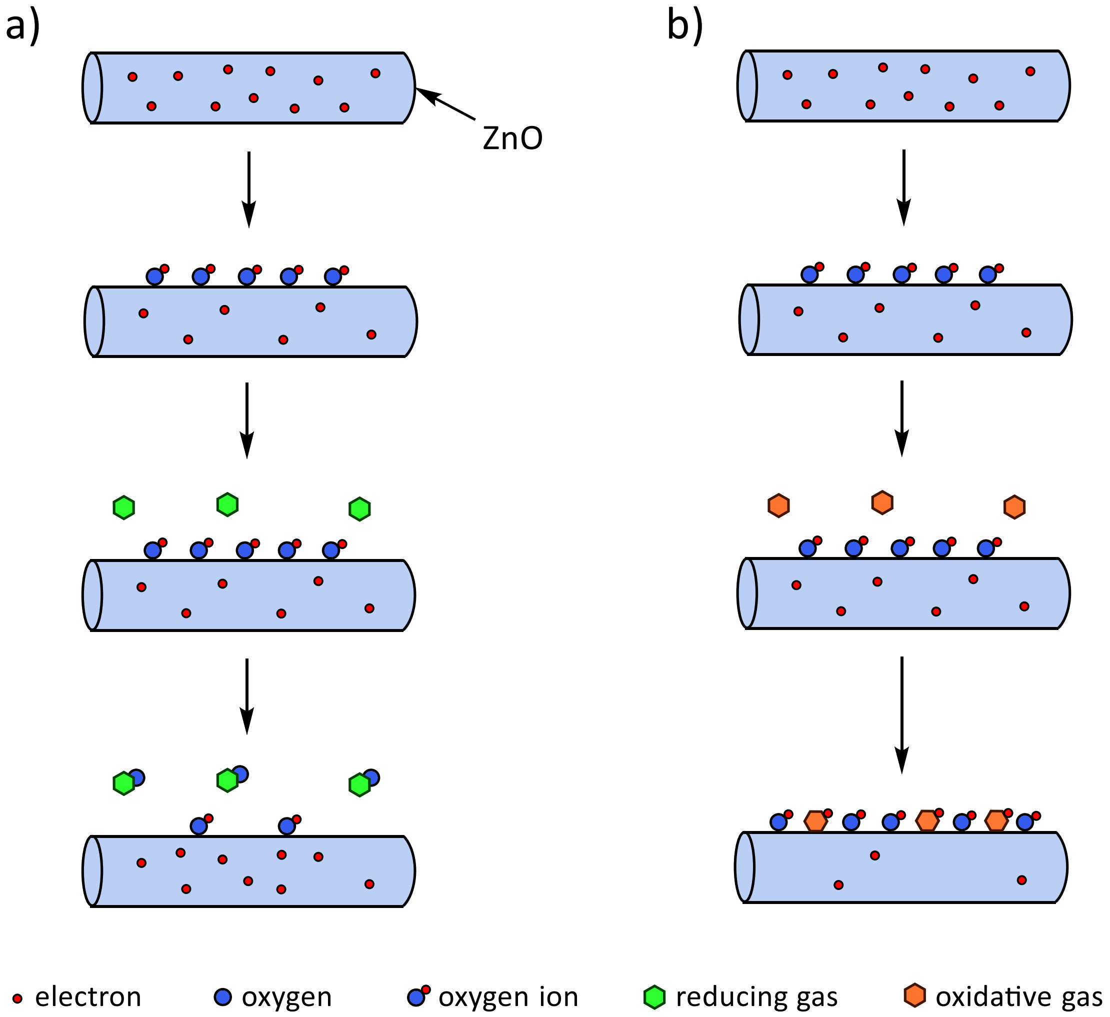

Figure 29 *- Schematic representation of a) reducing and b) oxidative gas sensor*

Various lignocellulosic templates have been used to prepare highly porous zinc oxide ceramics for gas sensing applications. Liu et al. [188] exploited the hierarchical porosity of softwood-fir and hardwood-lauan to synthesize pure ZnO ecoceramics with optimal sensing properties toward H_2S (Table 6). The materials were prepared following the typical pyrolysis-impregnation-calcination process, and in both cases the original wood structure was inherited by the final ceramics (Figure 30a, b). Fir-templated ZnO preserved the regular porous array of the tubular tracheid cells, while lauan-templated ZnO retained the two sizes of fiber cells (5-10 µm and 15-20 µm) that its pyrolyzed form previously displayed. The crystallite size (Fir: 15.6 nm, Lauan: 18.9 nm) and porosity (Fir: 80.29%, Lauan: 79.56%) of the products were respectively smaller and larger than those obtained by non-templated ZnO (crystallite size: 50.3 nm; porosity: 45.35%). This fact greatly improved the gas percolation in the materials, enhancing the sensing performance with respect to the non-templated ceramic. Moreover, the larger surface area of fir-templated ZnO (16.09 $m^2 \cdot g^{-1}$) compared to lauan-templated ZnO (9.71 $m^2 \cdot g^{-1}$) explained the better sensitivity of the former compared to the latter.

In work by Hamrouni et al. [198] pure ZnO ceramics were prepared using sunflower pollen, and applied for the selective sensing of NO_2 (Table 6). The promising performance of the resulting product was due to its unique micro and nano structure. The zinc oxide ecoceramic retained the spherical structure of pollen grains, being composed of agglomerated sphere-shaped nanoparticles of 30–60 nm in diameter and a mean crystallite size of 35.7 nm (Figure 30c, d). The highly porous nature of the product was the basis of the enhanced response to NO_2 with respect to the non-templated ZnO sensor fabricated through a simple sol–gel procedure. Indeed, the preparation of calibration curves demonstrated a very low detection limit of the sensor, capable of detecting nitrogen dioxide concentrations as low as 0.15 ppm.

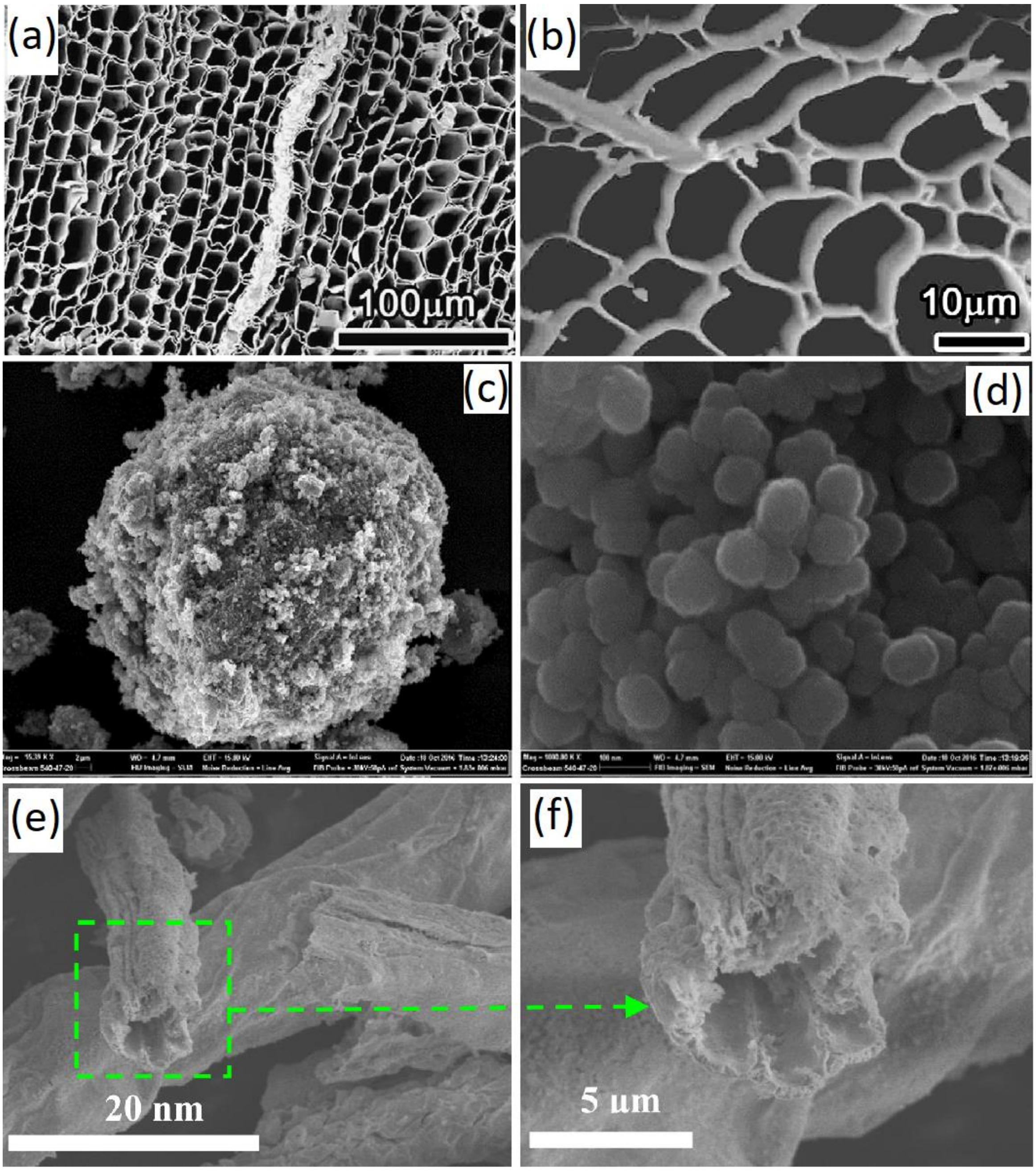

Figure 30 *– SEM images of a) fir-templated ZnO, b) lauan-templated ZnO [188]; c, d) sunflower pollen-templated ZnO [198]; e, f) cotton-templated* CeO_2*/ZnO [196]*

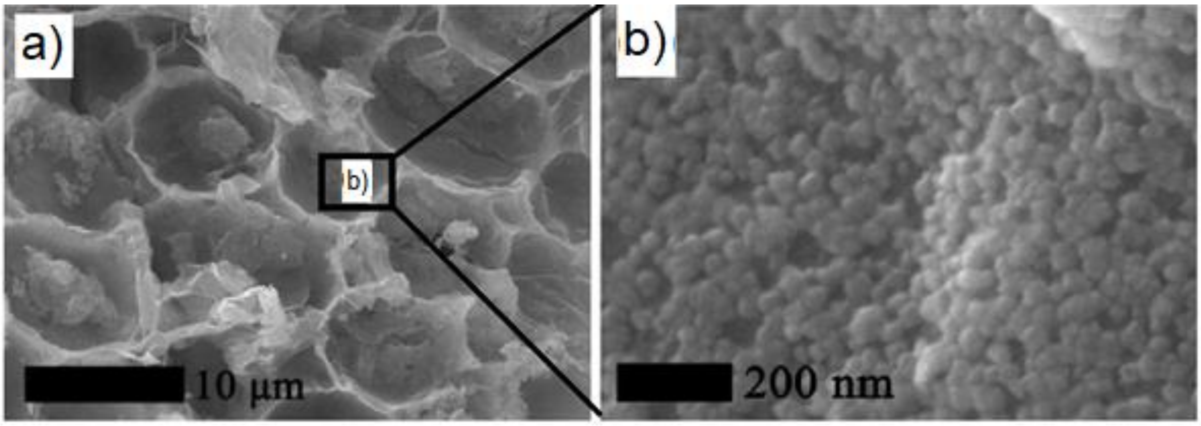

***Figure 31** – a, b) SEM images of poplar leaf-templated NiO/ZnO [202]*

To enhance the sensing response of ZnO ecoceramics the doping process is a valuable choice. Indeed, dopants can induce the formation of smaller nanostructures with a larger number of oxygen vacancies, thus increasing the number of chemisorbed gas molecules and consequently reducing the required working temperature, improving the selectivity, stability, and the fast response towards the target gas. [183, 205] Various works have focused attention on the combination of natural templating and doping methods. Wang et al. [195] exploited cotton fibers to produce hollow microtubes of ZnO doped with In_2O_3 showing promising sensing properties toward acetone (Table 6). The obtained hollow microfibers presented diameters of 6-8 µm, with walls composed of numerous other hollow tubes. This architecture could provide an easy pathway for the penetration of gas molecules, improving the efficiency of the material. Moreover, both inner and outer surfaces of In_2O_3–ZnO hollow microtubules were covered with folds and projections, which further increased the contact surface between the sensor and the transiting gas. The maximum response of the doped ceramic was two-times larger than that of cotton-templated pristine ZnO sensors, confirming the improved gas sensing properties due to the doping procedure.

Other research in which the doping process was used in combination with cotton as a sacrificial scaffold was performed by Yan et al. [196] In their work, Yan et al. prepared biomorphic ZnO ceramics doped with CeO_2 which exhibit a much better sensing response to ethanol compared to pure ZnO ecoceramics. Both pure and doped biomorphous ZnO ceramics were composed of a hollow microtubular structure with many pores on the fiber walls (Figure 30e, f). However, CeO_2/ZnO microtubes showed an average crystallite size of 20.42 nm, while pure ZnO a larger one of 22.29 nm. Moreover, also the specific surface area of the ceria doped sample was lager compared to that of pristine ZnO microfibers (36.39 $m^2 \cdot g^{-1}$ vs 27.98 $m^2 \cdot g^{-1}$), confirming the positive effects that the doping process can have on these parameters. Gas sensing investigations showed that the CeO_2–ZnO sensor possessed a good response at relative low operating temperature of 260 °C, presenting excellent stability and selectivity toward ethanol with respect to other VOCs like acetone, methanol, acetic acid, dimethylformamide and ammonia (Table 6).

Not only cotton was exploited as a template for the preparation of doped ZnO ceramics. In Zeng et al.'s work [202] poplar tree leaves served as a template for the preparation of NiO/ZnO biomorphic nanocomposites showing enhanced gas sensing performance towards the detection of n-butanol. After the typical substitution process, NiO-doped ZnO biomorphous materials maintained the hierarchical and porous sponge-like structure of the superficial tissue of poplar leaves, being composed of nanoparticles with average diameters of 30 nm (Figure 31a, b). Even in this case, the doping procedure effectively decreased the average diameter of the nanoparticles, since pure biomorphic ZnO samples presented NPs with a mean size of 45 nm. Moreover, from XPS and photoluminescent (PL) analysis, it was found that the relative percentage of V_o in the biotemplated NiO/ZnO ceramics was greater in than that in pure biomorphic ZnO NPs. This fact confirmed that the decoration of ZnO with NiO increased the number of oxygen vacancies, which can further react with the reducing gas (n-butanol), producing a larger resistance variation and an improvement of the sensing signal. [206] The good sensitivity at a relative low operating temperature proves that the combination of biotemplating technique and Ni-doping process is an excellent strategy for the synthesis of gas sensors with enhanced performance (Table 6).

Table 6 – Gas sensing properties of biomimetic ZnO ceramics

Material	Biotemplate	BET ($m^2 \cdot g^{-1}$)	Selectivity	Sensitivity (S)	Optimal working temperature	τ_{res} ; τ_{rec}	LOD (ppm)	Ref
ZnO	Fir wood	16.09	H_2S (50 ppm)	~200[a]	332 °C	6 s ; 10 s	/	[188]
ZnO	Lauan wood	9.71	H_2S (50 ppm)	~100[a]	332 °C	3 s ; 16 s	/	[188]
ZnO	Sunflower pollen	14	NO_2 (5.8 ppm)	8[b]	250 °C	150 s ; 180 s	0.15	[198]
In_2O_3/ZnO	Cotton fibers	/	Acetone (100 ppm)	62.5[a]	300 °C	3 s ; 7 s	0.1	[195]
CeO_2/ZnO	Cotton fibers	36.39	Ethanol (200 ppm)	46[a]	260 °C	/	5	[196]
NiO/ZnO	Poplar leaf	/	n-butanol (100 ppm)	106[a]	240 °C	4 s ; 1.6 s	0.41	[202]

[a] S=Ra/Rg, since targeting gas is a reducing gas; [b] S=Rg/Ra since targeting gas is an oxidant gas

As previously mentioned, ZnO is a metal oxide with a similar band gap to that of titania, and which has shown interesting applications as photocatalyst for the removal of contaminants. [184] The principle behind the photocatalytic activity of zinc oxide is similar of that of TiO_2, basing its action on the formation of electron-hole pairs after suitable light irradiation.

Also in the case of ZnO ceramics, to improve the photocatalytic performance, various lignocellulosic templates have been mimicked to prepare complex and efficient nanostructures for the degradation of methylene blue in water solutions (Table 7). Work by Quarta et al. [189] showed the possibility of obtaining zinc oxide ecoceramics using pyrolyzed cork as a starting biological template, and exploiting a new approach of infiltration using an aerosol of a zinc-containing solution. Depending on the Zn precursor used (zinc acetate or zinc nitrate), number of infiltration cycles, and the time and temperature of calcination, ZnO samples with slightly different chemical compositions and morphologies were obtained. Overall, when the calcination temperature was 350 °C, ZnO-graphite composites were produced while, when the heating temperature was raised to 700 °C, the total removal of the template occurred, and pure ZnO ceramic was synthesized. Moreover, the lower temperatures allowed the maintenance of the typical honeycomb structure of cork, while the higher one led to the loss of the 3-DOM morphology. This fact is not in agreement with previous work on other cork-derived ceramics, [165, 207] and may be caused by the use of methanol instead of water as solvent, but more investigations are required in this direction. However, even when the 3D cork structure was not maintained, the resulting materials showed high levels of open porosity and connectivity.

Photocatalytic degradation of MB was applied under artificial sunlight irradiation (using a 150W xenon lamp as UV-visible light source) and demonstrated that the ZnO ecoceramic with the best performance was the one with the largest specific surface area (~80% of MB removal after 30 min; BET: 120.09 $m^2 \cdot g^{-1}$), while the worst was that one with the smallest (~15% of MB removal after 30 min; BET: 7.64 $m^2 \cdot g^{-1}$). The low photoactivity, however, was an optimal starting point for the production of more benign ZnO sunscreen filter. Photocatalytic activity is in fact associated with the production of reactive oxygen species (ROS), which can act as harmful agents and, therefore, be a problem for human skin. For this reason, in Quarta et al.'s research, the lowest photocatalytic performance sample was doped with aluminium, which is a commonly known element able to inhibit ROS formation. [208, 209] The resulting product showed very low degradation activity, but still presented good UV absorption properties, thus making the obtained ZnO ecoceramic a promising candidate to be used as a sunscreen.

On the contrary, to enhance the photocatalytic activity of zinc oxide and improve the pollutant removal efficiency, Zhou et al. synthesized N-doped ZnO ecoceramics using *Cinnamon camphora, Sweetscent Oleander, Zea Mays Linn.* and *Pea Shoot* leaves as templates. [203] After an acid pre-treatment to get rid of Mg, K, Ca, P and S ions, leaves were infiltrated two times in a $Zn(NO_3)_2$ solution and then calcined in air at 550 °C. The process led to the formation of N-doped ZnO artificial leaves which retained the macro, micro and nano structure of the original template (Figure 32). As happened for the Pt/N-doped TiO_2 artificial leaves mentioned in Chapter 4.1 obtained by the same research group, [54] the ZnO ecoceramic even correctly reproduced the porous framework of veins at micro scale and granums at nano scale. This precise replica of the leaves, together with the self-doping of nitrogen, resulted in an improved photodegradation of MB that reached an efficiency up to 99.6% under artificial sunlight irradiation (using a 500W xenon lamp as UV-visible light source) (Table 7).

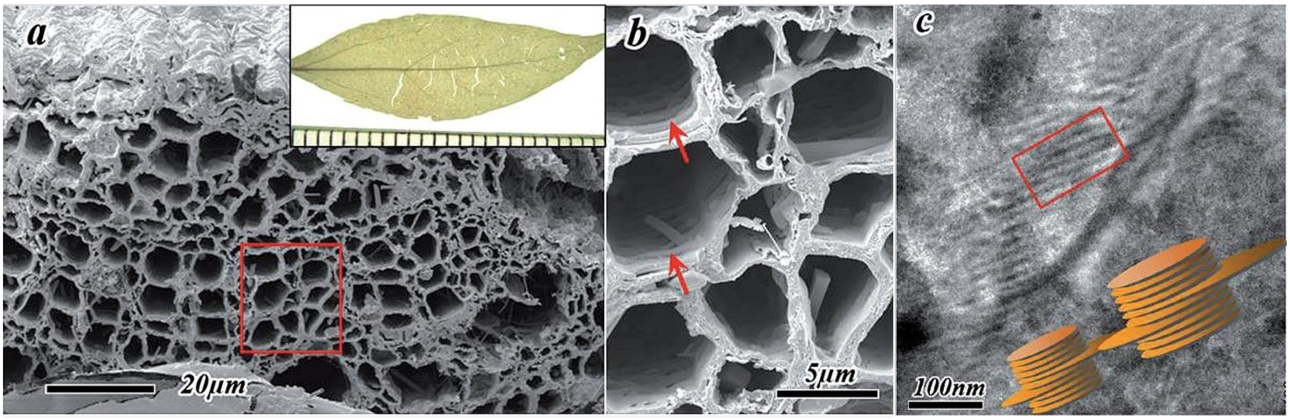

Figure 32 *– a) FESEM image of of the cross-section of Cinnamomum camphora leaf-templated N-doped ZnO ecoceramic (inset: photograph of the product); b) magnified image of the red square of a; c) TEM image of artificial ZnO granum with the illustration of the 3D structure [203]*

A decrease in performance, instead, occurred when cobalt and nickel were inserted into the zinc oxide crystalline structure. In Black et al.'s study [200] on the replication of *Zamioculcas zamiifolia* leaf, combined with the substitution of Zn^{2+} with Co or Ni in the wurtzite structure, resulted in the production of less photocatalytic active ecoceramics. Compared to pure *Zamioculcas zamiifolia* leaf-templated zinc oxide ceramics, Co and Ni doped composites showed lower efficiency in the degradation of MB under UV light generated by a medium-pressure 450W mercury lamp, especially in presence of cobalt (Table 7). This negative effect could be caused to the formation of a too large number of oxygen vacancies that can act as e-/h+ recombination centers and, thus, decrease the general photocatalytic activity. [210] Moreover, Co^{2+} ions in the ZnO lattice are possibly susceptible to oxidation to Co^{3+}, which would affect the hole charge carriers. [200] Another reason for the decreased efficiency could be due to the presence of impurities (e.g. calcite) at the crystallite interfaces, and to the large nanoparticle aggregation at the surface of the material, which may have facilitated the e-/h+ recombination and reduced the photooxidation of the dye.

These low levels of photodegradation of MB are in disagreement with the successive study of Liu et al. [199] performed with the use of a lotus pollen-templated Co_3O_4/ZnO ceramic. In Liu et al.'s work, zinc oxide hollow microspheres doped with Co_3O_4 were prepared by the typical impregnation/calcination method using lotus pollen as a biotemplate. The product had a diameter of 25 μm, a wall thickness of about 2 μm, an average pore size distribution of 17 nm and a specific surface area of 36.94 $m^2 \cdot g^{-1}$ (specific surface area of non-templated Co_3O_4/ZnO NPs: 6.74 $m^2 \cdot g^{-1}$). This Co_3O_4/ZnO ecoceramic showed the degradation of 94.9% of methylene blue in 90 minutes using a xenon lamp as UV-visible light source, with the efficiency that remained stable even after 4 recycle rounds. Unlike the study carried out by Black et al., [200] in this case Co^{2+} did not enter into the wurtzite structure, but it formed distinct nanocrystals of Co_3O_4 near ZnO nanocrystals (Figure 33c). The adjacent position of Co_3O_4 and ZnO was beneficial for the photoactivation process, thanks to the different band potentials that the two materials possess. Indeed, when placed in contact with ZnO, the conduction and valence band of Co_3O_4 are at higher energy levels than their counterparts in zinc oxide. [211] After UV-visible irradiation, both Co_3O_4 and ZnO are excited and the peculiar proximity between the two promotes electron transfer from the CB of Co_3O_4 to the CB of ZnO and hole transfer from the VB of ZnO to the VB of Co_3O_4. [212, 213] This configuration suppresses the possible recombination of photogenerated charges, thus increasing the activity of the material, similar to the effects seen between anatase and rutile titania.

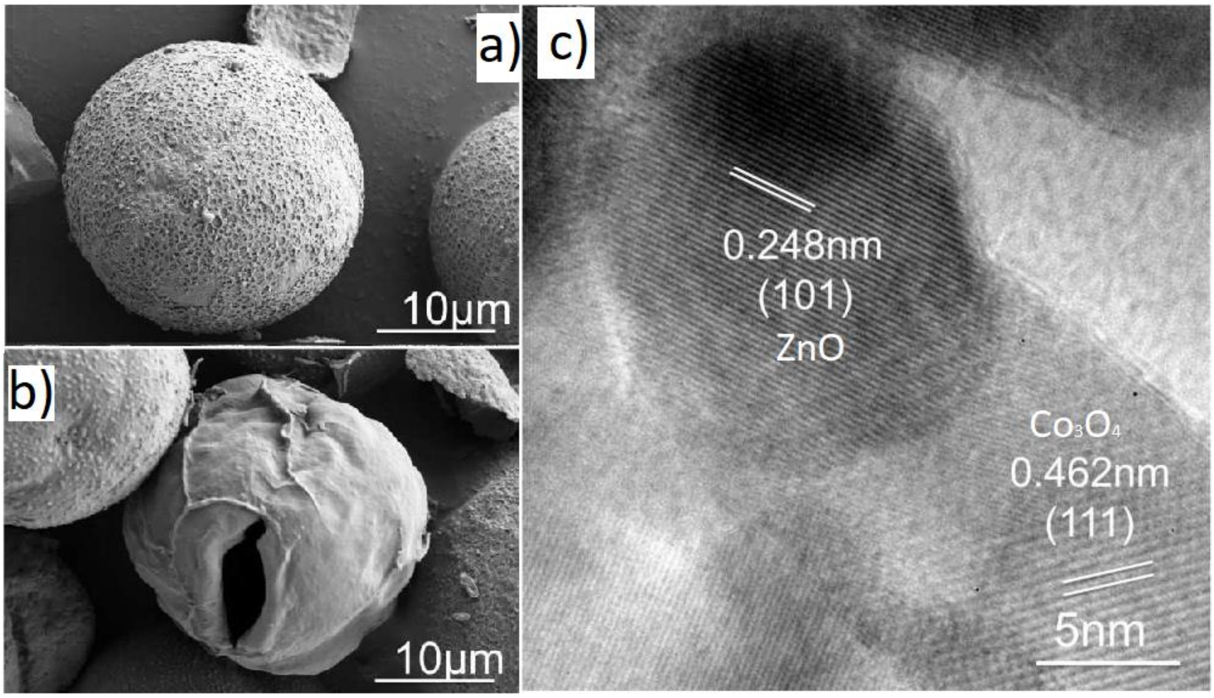

Figure 33 *– a, b) SEM images of pollen-derived Co_3O_4/ZnO ceramic; c) HRTEM image of adjacent Co_3O_4 and ZnO crystals [199]*

Table 7 – Photodegradation efficiency against MB of ZnO ecoceramics

Biotemplate	Material	BET ($m^2 \cdot g^{-1}$)	Irradiation source	Removal efficiency	Ref
Cork wood	ZnO	120.09	Artificial sunlight (Xe lamp)	~80% after 30 min	[189]
Cinnamon camphora leaf	N/ZnO	/	Artificial sunlight (Xe lamp)	99.6% after 90 min	[203]
Zamioculcas zamiifolia leaf	ZnO	11.1	UV light (Hg lamp)	~85% after 30 min	[200]
Zamioculcas zamiifolia leaf	Ni/ZnO	/	UV light (Hg lamp)	~60% after 30 min	[200]

Table 7 – Continued

Biotemplate	Material	BET ($m^2 \cdot g^{-1}$)	Irradiation source	Removal efficiency	Ref
Zamioculcas zamiifolia leaf	Co/ZnO	/	UV light (Hg lamp)	~30% after 60 min	[200]
Lotus pollen	ZnO	/	Artificial sunlight (Xe lamp)	58.2% after 90 min	[199]
Lotus pollen	Co_3O_4/ZnO	36.94	Artificial sunlight (Xe lamp)	94.9% after 90 min	[199]

4.4 Biomorphous oxide ceramics from other transition metals (V, Cr, Mn, Fe, Co, Ni, Cu, Y, Zr, and W)

Transition metals are a large class of elements generally defined as those elements which have a partially filled *d*-shell, or which can give rise to cations with an incomplete *d*-shell. [214]. Besides some exceptions, all transition elements share general common properties [215]:

- They are all metals.
- They are almost all hard, strong, high-melting and high-boiling point materials.
- They efficiently conduct heat and electricity.
- They easily form alloys with one another and with other metallic elements.
- They exhibit variable valence and their compounds are usually colored, due to *d*-*d* electronic transition.

An important category of compounds that characterize transition elements is the transition metal oxides (TMOs). TMOs are materials composed of oxygen atoms bound to transition metals. They have a wide variety of structures and properties which makes them one of the most important classes of solids. Among the interesting features that oxides of *d*-block transition elements exhibit, an outstanding range of electronic and magnetic properties is one of the most noteworthy. The peculiar behaviour of TMOs that distinguish them from metallic elements, alloys, covalent semiconductors and ionic insulators is caused by the unique configuration that electrons assume in these ceramics. Transition metal oxides present slight overlap between the metal *d* and the oxygen *p* orbitals, thus giving rise to narrow electronic bands. [216] Due to this characteristic, TMOs are gaining attention for their possible applications in the field of electrochemical capacitors (ECs) and lithium-ion batteries (LIBs). In recent years MnOx, CoOx, NiO, and other oxides have been extensively investigated as promising electrode materials. These oxides, in fact, present higher specific capacitance thanks to reversible faradaic redox reactions, which make them better performing than carbonaceous materials. [217]

Other interesting applications that oxides of *d*-block transition elements have shown are catalytic conversion of toxic compounds into unharmful products, solid state gas sensing, electromagnetic interference (EMI) shielding, and adsorption and photodegradation of dyes and pollutants. Most of these applications rely for their performance on the micro and nanostructure that TMOs can possess. Indeed, porous and interconnected networks, together with a wide specific surface area, can enhance the results that these ceramics could obtain. Therefore, mimicking the hierarchic structure of biological templates is an ideal option to produce materials with outstanding performance while, at the same time, exploiting natural and affordable waste resources, like woods and fibers.

Table 8 – TMO-ceramics obtained using lignocellulosic-template biomimetic synthesis

Material	**Biotemplate**	**Morphology**	**Property**	**Ref**
Fe_2O_3	Wood (Pine, Fir, Poplar, Beech)	Highly porous	EMI shielding	[218]
Fe_2O_3	Wood (Fir)	Highly porous	/	[219]
Fe_2O_3	Wood (Various)	/	/	[220]
Fe_2O_3	Wood (Various)	/	/	[221]
$C/Fe_2O_3/Fe_3O_4$	Wood (Eucalyptus)	Highly porous	Adsorption and removal of pollutants	[222]
$C/Fe_2O_3/Fe_3O_4$	Wood (Eucalyptus)	Highly porous	Adsorption and removal of pollutants	[223]
$C/Fe_2O_3/Fe_3O_4$	Wood (Eucalyptus)	Highly porous	Adsorption and removal of pollutants	[224]
$BaFe_{12}O_{19}$	Wood (Cedar)	1D pore structured	/	[225]
$BaFe_{12-x}Cr_xO_{19}$	Wood (Spruce)	Highly porous	Microwave absorption capacity	[226]
$SrZnCoFe_{16}O_{27}$	Wood (Pine)	1D pore structured	/	[227]
$Sr_3Co_2Fe_{24}O_{41}$	Wood (Cork)	3-DOM	/	[207]
$Ni_xZn_{1-x}Fe_2O_4$	Wood (Cedar)	3-DOM	/	[228]
Fe_2O_3	Fibers (Scallion root)	Hollow microfiber	/	[229]
Fe_2O_3	Fibers (Cotton)	Hollow microfiber	/	[230]
Fe_2O_3	Fibers (Cotton)	Hollow microfiber	/	[231]
Fe_2O_3	Fibers (Cotton)	Hollow microfiber	Lithium-ion batteries	[232]

Table 8 – Continued

Material	**Biotemplate**	**Morphology**	**Property**	**Ref**
$LiFe_5O_8$	Fibers (Cotton)	Hollow microfiber	Lithium-ion batteries	[232]
$LiFeO_2$	Fibers (Cotton)	Hollow microfiber	Lithium-ion batteries	[232]
Au/Fe_2O_3	Fibers (Cotton)	Hollow microfiber	Conversion of 4-nitrophenol to 4-aminophenol	[233]
Ag/Fe_2O_3	Fibers (Cotton)	Hollow microfiber	Conversion of 4-nitrophenol to 4-aminophenol	[233]
Pd/Fe_2O_3	Fibers (Cotton)	Hollow microfiber	Conversion of 4-nitrophenol to 4-aminophenol	[233]
$LaFeO_3$	Fibers (Cotton)	Hollow microfiber	Gas-sensing	[234]
$LaFeO_3$	Fibers (Sorghum straw)	Hollow microfiber	Gas-sensing	[235]
Fe_2O_3	Pollen	Hollow microsphere	Degradation of pollutants	[236]
Fe_2O_3	Pollen (Sunflower)	Hollow microsphere	/	[237]
Fe_2O_3	Pollen (Pine)	Hollow microsphere	Adsorption and removal of pollutants	[238]
$MgFe_2O_4/Fe_2O_3$	Pollen (Pine)	Hollow microsphere	Adsorption and removal of pollutants	[238]
NiO	Wood (Pine)	Highly porous	/	[239]
NiO	Wood (Pine)	Highly porous	Adsorption and removal of pollutants	[240]
NiO	Fibers (Cotton, Hemp, Flax)	Hollow microfiber	Gas-sensing	[241]
NiO	Fibers (Scallion root)	Hollow microfiber	/	[229]
NiO	Fibers (Cotton)	Hollow microfiber	/	[242]
NiO	Fibers (Cotton)	Hollow microfiber	Lithium-ion batteries	[243]
$NiCo_2O_4$	Fibers (Cotton)	Hollow microfiber	Electrochemical capacitor	[244]
$Zn/NiCo_2O_4$	Fibers (Cotton)	Hollow microfiber	Electrochemical capacitor	[244]
NiO	Pollen (Rape)	Hollow microsphere	Electrochemical capacitor	[245]
Pd/PdO/NiO	Pollen (Lotus)	Hollow microsphere	Gas-sensing	[246]
NiO	Leaves (Spent Tea)	Nanoparticle	Oxygen evolution reaction	[247]

Table 8 – Continued

Material	Biotemplate	Morphology	Property	Ref
Ni-Fe oxides	Leaves (Spent Tea)	Nanoparticle	Oxygen evolution reaction	[247]
Co_3O_4	Fibers (Cotton)	Hollow microfiber	Disel soot oxidation	[170]
Co_3O_4	Fibers (Scallion root)	Hollow microfiber	/	[229]
Co_3O_4	Fibers (Sorghum straw)	Hollow microfiber	Electrochemical capacitor	[248]
Co_3O_4	Fibers (Cotton)	Hollow microfiber	Lithium-ion batteries	[249]
C/Co_3O_4	Fibers (Cotton)	Hollow microfiber	Electrochemical capacitor	[250]
Co_3O_4	Pollen	Hollow microsphere	Degradation of pollutants	[236]
Co_3O_4	Pollen (Lotus)	Hollow microsphere	Photodegradation of pollutant	[199]
Co_3O_4	Leaves (Ginko)	3-DOM	Non-enzymatic sensing	[251]
$LiCoO_2$	Leaves (cherry blossom)	3-DOM	Lithium-ion batteries	[252]
Co_3O_4	Petals (Rose)	Nanosheets	Photodegradation of pollutant	[253]
ZrO_2	Wood (Pine)	Highly porous	/	[116]
ZrO_2	Wood (Oak)	Highly porous	/	[254]
ZrO_2	Wood (Pine and Jelutong)	Highly porous	/	[12]
ZrO_2	Wood (Pine sawdust)	Highly porous	/	[255]
PdO/ZrO_2	Wood shavings	Highly porous	Catalytic application	[256]
Y_2O_3/ZrO_2	Wood (Pine and Rattan)	Highly porous	/	[257]
ZrO_2	Fibers (Jute)	Microfiber	/	[258]
ZrO_2	Fibers (Cotton)	Hollow microfiber	Heat-insulating applications	[259]
ZrO_2	Pollen (Rape)	Hollow microsphere	Adsorption of pollutant	[260]
ZrO_2	Leaves (Various)	/	/	[138]
CuO	Fibers (Cotton)	Hollow microfiber	/	[261]
CuO	Fibers (Syngonium podophyllum root)	Hollow microfiber	/	[262]

Table 8 – Continued

Material	**Biotemplate**	**Morphology**	**Property**	**Ref**
CuO	Fibers (Cotton)	Hollow microfiber	Adsorption and removal of pollutant	[263]
Al_2O_3/CuO	Fibers (Cotton)	Hollow microfiber	Adsorption and removal of pollutant	[263]
CuO	Pollen	Hollow microsphere	Degradation of pollutants	[236]
Mn_2O_3	Wood (Fir, Paulownia)	Highly porous	IR absorption properties	[264]
Mn_2O_3/Mn_3O_4	Wood (Fir, Paulownia)	Highly porous	IR absorption properties	[264]
Mn_3O_4	Wood (Fir, Paulownia)	Highly porous	IR absorption properties	[264]
C/Mn_3O_4	Fibers (Cotton)	Hollow microfiber	Electrochemical capacitor	[217]
MnO_2	Fibers (Cotton)	Hollow microfiber	Electrochemical capacitor	[265]
MnO_2	Fibers (Cotton)	Hollow microfiber	Electrochemical capacitor	[266]
WO_3	Fibers (Cotton)	Hollow microfiber	/	[267]
Bi_2WO_6	Fibers (Cotton)	Hollow microfiber	Photodegradation of pollutant	[268]
WO_3	Pollen (Lotus)	Hollow microsphere	Gas-sensing	[269]
V_2O_5	Fibers (Cotton)	Hollow microfiber	Conversion of 4-nitrophenol to 4-aminophenol	[270]
V_2O_5	Fibers (Cotton)	Hollow microfiber	Electrochemical capacitor	[271]
Cr_2O_3	Wood (Fir, Paulownia)	3-DOM	/	[272]
Eu/Y_2O_3	Wood (Pine)	Monolithic 3-DOM	Photoluminescent properties	[273]

With the energy crisis becoming progressively critical, the rapidly growing demands for portable electronic devices and electric vehicles, electrochemical capacitors (ECs) and lithium-ion batteries (LIBs) have attracted worldwide attention as possible solutions for energy requirements. [274]

ECs can be divided into electrical double-layer capacitors (EDLCs) and pseudocapacitors. Like batteries, EDLCs are based on electrochemical cells composed of two electrodes, an electrolyte and a porous separator membrane which allows the transit of ions. However, in this type of cell, no redox reactions occur, and the electrostatic storage is achieved by the separation of charge in a double layer at the interface between the electrodes and the electrolyte (Figure 34). [275] Pseudocapacitors base their operation on a similar mechanism, but showing larger charge storage capabilities thanks to the involvement of reversible and fast redox reactions (the same, but faster, as that occurring in batteries) at or near the electrode surface. [276, 277]

The most important parameters for testing the performance of supercapacitors are the specific capacitance, the capacitance cycling retention, the energy density and the power density. Despite excellent cycling stability (20k – 1000k recharge cycles) and relatively large power density (10 – 100k $W\cdot kg^{-1}$), electrochemical capacitors suffer from a very low energy density (1 – 15 $W\cdot h\cdot kg^{-1}$), compared to batteries (100 – 265 $W\cdot h\cdot kg^{-1}$), due to the limited specific capacitance of the carbon materials of which they are usually composed. To improve these properties, large surface area and high electrical conduction are features desired in the electrode materials, to increase the ion adsorption and the transport of electrons. [278, 279]

An interesting category of materials for pseudocapacitors is represented by TMOs which could be able to provide the desired characteristics in this field, such as higher energy and power density together with long lifetime.

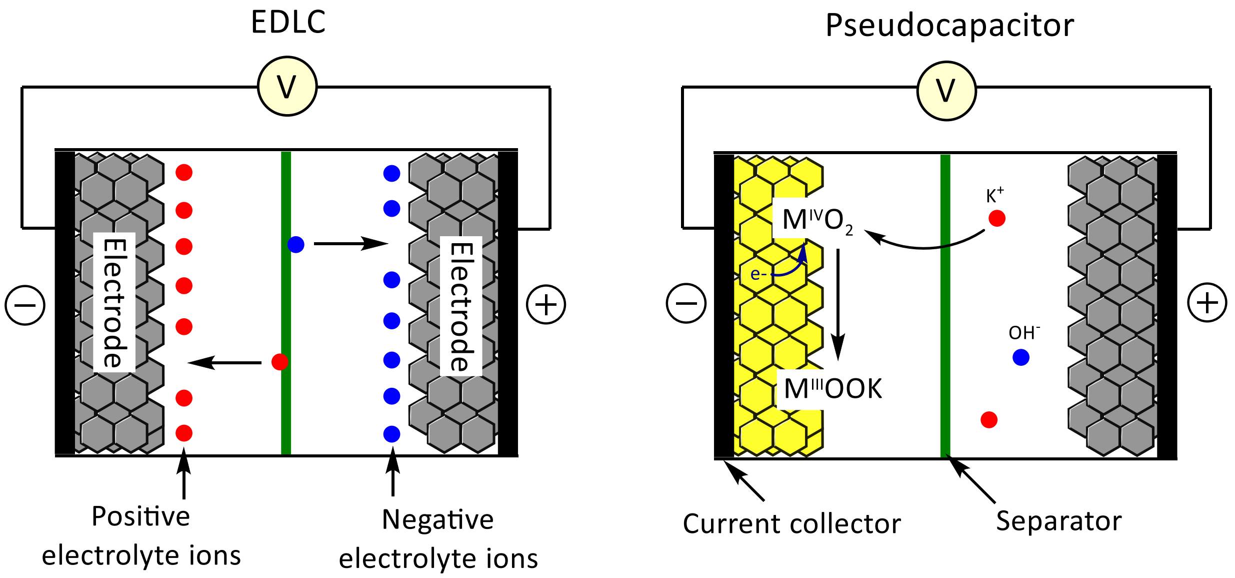

***Figure 34** – Schematic representation of an EDLC and a pseudocapacitor*

Manganese dioxide (MnO_2) is an important transition metal oxide which has already found good applications in dry-cell batteries, such as the zinc-carbon battery and the alkaline battery. [280] MnO_2 possesses excellent energy and power density features, showing at the same time low self-discharge. [281] Its structural flexibility, combined with the possibility to prepare highly porous architectures mimicking natural templates, could lead to the preparation of promising materials for improved electrochemical performances. Yan et al. [266] demonstrated the preparation of MnO_2 microtubes with mesoporous characteristics by using cotton fibers as biotemplates. MnO_2 tubes retained the cylindrical structure of cotton, being composed only of manganese dioxide crystals of 100 nm size. The resulting product showed better electrochemical performance compared to bulk manganese dioxide prepared without the natural sacrificial scaffold. The determined specific capacitance was equal to 128 $F \cdot g^{-1}$ and 32 $F \cdot g^{-1}$ at a current density of 0.5 $A \cdot g^{-1}$ for the biomorphic sample and bulk sample, respectively. This feature was maintained even after 1000 charge-discharge cycles, showing a capacitance loss of only 2.73% (Table 9) The improved electrochemical properties of biomorphic MnO_2 with respect to the non-templated sample can be attributed to the larger surface area (35.55 $m^2 \cdot g^{-1}$ vs 5.78 $m^2 \cdot g^{-1}$) and its unique tubular mesoporous microstructure (Figure 35a, b).

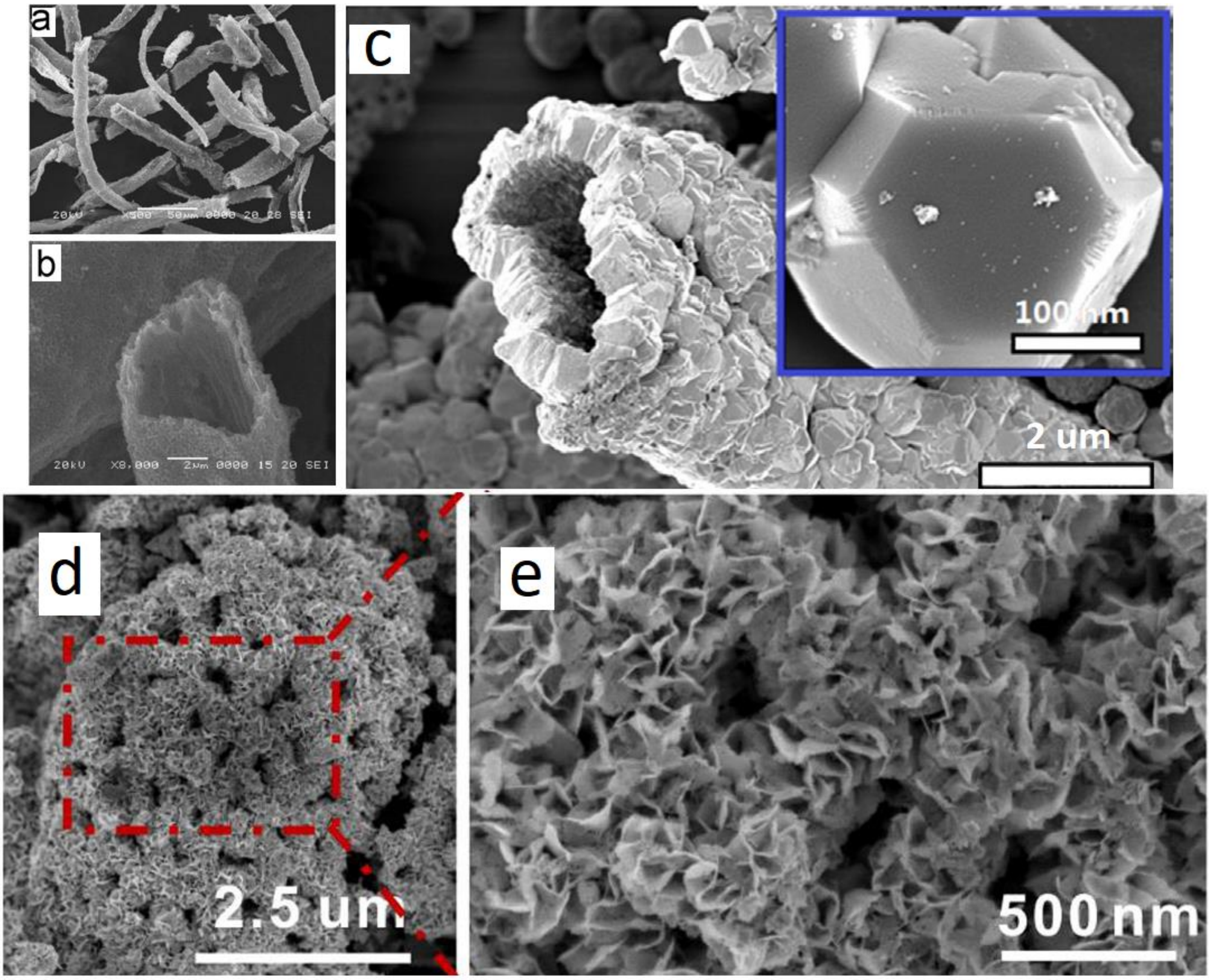

Figure 35 *– SEM micrograph of a, b) cotton-templated MnO_2 microtubes [265], c) cotton-templated Co_3O_4 microtubes obtained after 3h of calcination (inset: octahedral Co_3O_4 nanocrystal) [250], d, e) pollen-templated NiO microstructure [245]*

Co_3O_4 is another transition metal oxide which has been recently investigated as a possible pseudocapacitor electrode material, thanks to its high specific capacitance and low cost. [282] However, despite its ideal properties, pure Co_3O_4 usually shows limited cycling stability after some charge-discharge cycles. [248] To improve cobalt oxide capabilities, Sun et al. [250] prepared biomorphic Co_3O_4/C microtubes which displayed larger specific capacitance and stability, using cotton as template. In the study, the typical substitution process, in which cotton is dipped into a precursor solution and subsequently calcined, is modified with the insertion of a hydrothermal treatment prior to the heating step. Thanks to this additional process, and to the low temperature and time of calcination (400°C for 2h), the total degradation of cotton is prevented, and a porous carbon tube coated by interconnected Co_3O_4 nanocrystals is formed (Figure 35c). An interesting feature that the Co_3O_4 nanocrystals showed was a peculiar octahedral structure (insert Figure 35c). Investigation of electrochemical performance of different shapes of cobalt oxide reported that octahedral crystals might possess enhanced activity in functions involving charge transport, such as catalysis or energy storage and conversion. [283]

From electrochemical analysis, Co_3O_4/C microtubes prepared by Sun et al. presented a specific capacitance almost 5-fold higher than that of pure Co_3O_4 (284.2 $F \cdot g^{-1}$ vs 58.1 $F \cdot g^{-1}$ at 1 $A \cdot g^{-1}$), and a large energy density of 36.13 $W \cdot h \cdot kg^{-1}$ at the power density of 1210 $W \cdot kg^{-1}$. These enhanced results are derived from the peculiar tubular structure and the large specific surface area of the biomorphic Co_3O_4/C ceramic. Indeed, the porous carbon skeleton offered appropriate space for the electrolyte diffusion during the electrochemical processes and, at the same time, reduced the effective path for the electron conduction. Moreover, the high value of specific surface area (67.8 $m^2 \cdot g^{-1}$) provided more active sites where electrochemical reactions could occur. [250]. All these aspects lead to greater stability of the material even in the long term, showing cyclic retention of 90.17% after 2000 charge-discharge cycles at 1 $A \cdot g^{-1}$ (Table 9).

An additional TMO ceramic that showed promising results as material for pseudocapacitor electrodes is pure nickel(II) oxide. NiO is a unique semiconductor which attracts attention due to important properties like great theoretical capacity, high redox activity and chemical stability and low cost. [284]. Recent studies proved that using hollow and porous nanostructures for NiO-based pseudocapacitors could improve the electrochemical performance of the material. [285-287] In fact, as demonstrated also in previously cited works, this morphology allows enhanced electron/ion conductivity, improvement in electrolyte transport and a larger number of electrochemical active sites for the redox reactions. [288]

In Wang et al.'s study [245], the prepared pollen-templated NiO ceramic exhibited high specific capacitance and long cycling life thanks to the peculiar structure at the micro- and nano- level. After the impregnation and calcination process, the material showed a porous and hollow elliptical microstructure (Figure 35d), being composed of numerous nano-sheets of pure NiO (Figure 35e). As seen in other research [244], the formation of nano-sheets greatly improved the performance of the material, leading in Wang et al.'s case to a specific capacitance of 1598 $F \cdot g^{-1}$ at 1 $A \cdot g^{-1}$ and still a high value of 714 $F \cdot g^{-1}$ at 30 $A \cdot g^{-1}$. Moreover, the good electrochemical properties were further confirmed by the high energy density of 66.4 $W \cdot h \cdot kg^{-1}$ at 1136.6 $W \cdot kg^{-1}$ and a long cycling life, which retained 95.7% of specific capacitance even after 5000 cycles at 10 $A \cdot g^{-1}$ (Table 9).

The large specific surface area of 73.78 $m^2 \cdot g^{-1}$ and the highly interconnected porous morphology of the ceramic are the main reasons for the best results among the reported materials obtained through a biotemplating method (Table 9). Also noteworthy is the presence of nano-sheets in both studies that have shown the largest specific capacitance. [244, 245]. This could be a determining factor for the improved electrical conduction and for the applications as pseudocapacitors, thus more investigations should be done in this direction.

No research has been performed using wood templated TMOs as pseudocapacitor electrode materials, and therefore, a greater interest in this area should be taken, especially due to the large specific surface area and hierarchically porous network that these platforms could provide.

Table 9 – Electrochemical performance of various ecoceramics-based pseudocapacitors

Material	**Biotemplate**	**BET ($m^2 \cdot g^{-1}$)**	**Specific capacitance ($F \cdot g^{-1}$) [a]**	**Cyclic retention [a]**	**Energy density ($W \cdot h \cdot kg^{-1}$) [b]**	**Ref**
MnO_2 [c]	Cotton fibers	35.55	128 at 0.5 $A \cdot g^{-1}$	97.27% (1000th at 0.5 $A \cdot g^{-1}$)	/	[266]
MnO_2 [c]	Cotton fibers	/	214 at 0.5 $A \cdot g^{-1}$	/	38.4 at 315 $W \cdot kg^{-1}$	[265]
Mn_3O_4/C	Cotton fibers	51.9	140.8 at 0.25 $A \cdot g^{-1}$	90.34% (5000th at 1 $A \cdot g^{-1}$)	27.13 at 410 $W \cdot kg^{-1}$	[217]
Co_3O_4	Sorghum straw	26.5	100.6 at 1 $A \cdot g^{-1}$	90.1% (9000th at 2 $A \cdot g^{-1}$)	/	[248]
Co_3O_4/C	Cotton fibers	67.8	284.2 at 1 $A \cdot g^{-1}$	90.17% (2000th at 1 $A \cdot g^{-1}$)	36.13 at 1210 $W \cdot kg^{-1}$	[250]
$NiCo_2O_4$ (Zn-doped) [d]	Cotton fibers	57.96	1228 at 2 $A \cdot g^{-1}$	92.6% (3000th at 2 $A \cdot g^{-1}$)	/	[244]
$NiCo_2O_4$ (Zn-doped) [e]	Cotton fibers	65.17	1344 at 2 $A \cdot g^{-1}$	83.7% (3000th at 2 $A \cdot g^{-1}$)	/	[244]
NiO	Rape pollen	73.78	1344 at 2 $A \cdot g^{-1}$ 714 at 30 $A \cdot g^{-1}$	95.7% (5000th at 10 $A \cdot g^{-1}$)	66.4 at 1136.6 $W \cdot kg^{-1}$	[245]
V_2O_5 [f]	Cotton fibers	11.78	680 at 1 $A \cdot g^{-1}$	20% (400th at 3 $A \cdot g^{-1}$)	55.8 at 460 $W \cdot kg^{-1}$	[271]

[a] Measured in a three-electrode system; [b] Measured in a two-electrode system (TMO ‖ Active Carbon); [c] Na_2SO_4 as electrolyte instead of KOH; [d] Molar ratio of elements Ni:0.5, Zn:0.5, Co:2.0; [e] Molar ratio of elements Ni:1.0, Zn:0.5, Co:1.5; [f] $LiNO_3$ as electrolyte instead of KOH

Lithium-ion batteries are another type of electrochemical device that have gained great attention recently thanks to their flexibility, high energy density and long lifecycle. LIBs are rechargeable batteries composed of two conductive electrodes in contact with an electrolyte and separated by a porous membrane separator. The peculiarity that differentiates LIBs from common batteries lies in the materials from which electrodes are made: the cathodes are normally composed of lithium metal oxides ($LiMO_2$), while the anodes are mostly realized with graphite.

In LIBs the charge carriers are lithium ions, which interact with the electrode materials through an insertion/de-insertion mechanism. During the charging process, lithium ions migrate from the lithium-based negative electrode towards the graphite-based positive electrode, by oxidation of the anode and the production of an equivalent number of electrons. Meanwhile, the released electrons travel through an external circuit reaching the positive electrode where reduction of carbon to LiC_6 occurs (Figure 36a).

During the discharging of the battery the entire process is reversed. LiC_6 releases the lithium ions which migrate through the electrolyte and re-join the metal-oxide reforming the initial $LiMO_2$. Meanwhile, electrons re-flow through the external circuit providing electrical energy, and subsequently completing the reduction at the cathode (Figure 36b). [279]

The performances of nowadays commercially available LIBs are limited by the low theoretical capacity of graphite electrodes (~372 $mA \cdot h \cdot g^{-1}$), which reduces the overall efficiency of the batteries. [289, 290] In this context, transition metal oxides have attracted wide attention as potential alternatives to carbon-based anode materials because of their higher theoretical capacities. [291] Among various TMOs, NiO has proven to be one of the most promising anode material thanks to its higher theoretical capacity of 718 $mA \cdot h \cdot g^{-1}$. [292] Unfortunately, nickel oxide suffers from the serious drawback of large volume expansion/contraction during the cycling process, leading to the pulverization of the electrode and a fast capacity decay, which hinders its practical application in LIBs. A possible solution for this problem is the fabrication of hierarchical mesoporous materials which, thanks to their peculiar structure, could provide better accommodation of volume changes thus preventing the collapse of the electrode. [293]

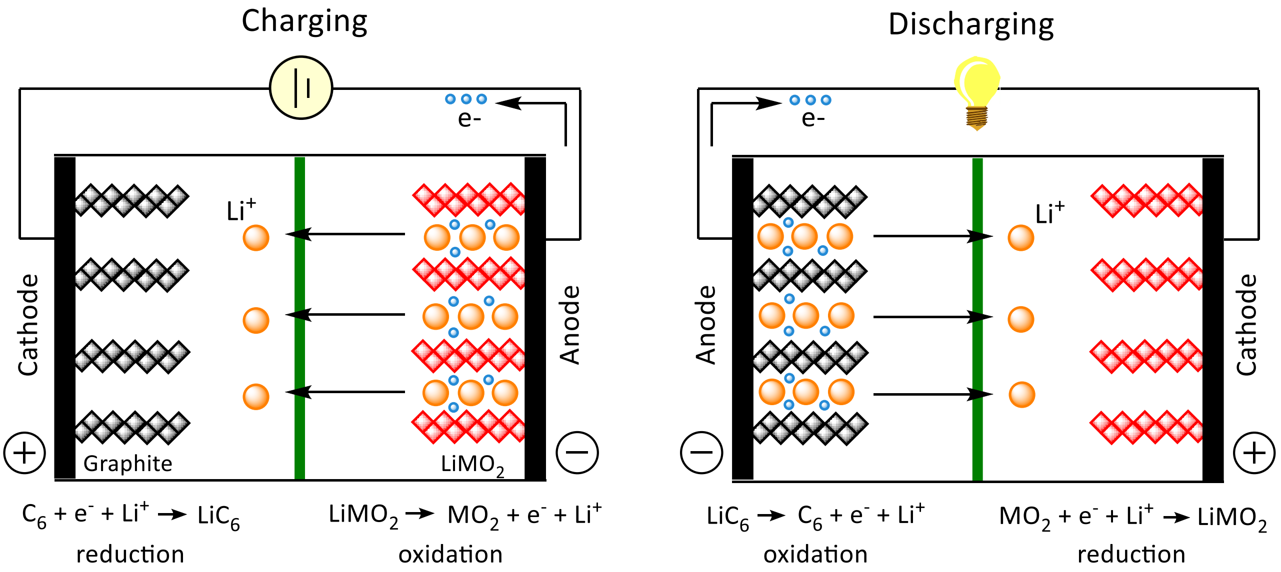

Figure 36 *– Charge-discharge process of a LIBs with graphite and lithium metal oxides electrodes*

In Zheng et al.'s work, [243] NiO microtubes were prepared by templating cotton fibers and applied as an anode material in a full cell lithium-ion battery. The resulting cell displayed high reversible capacity and good cycling performance, suggesting its great potential application as a practical LIB material. Pure NiO hollow microfibers were prepared through impregnation of the cotton fibers in a Ni^{2+} containing aqueous solution and subsequent annealing at 600 °C. The NiO samples retained the fibrous morphology of the original cotton fibers, being composed of nanocrystals with average size of 62.4 nm and of pores with diameter raging between 2.4 nm and 5.8 nm (Figure 37).

Preliminary electrochemical studies were performed using biomorphic NiO material and metallic lithium as electrodes in a typical coin-cell type battery, in the presence of $LiPF_6$ as electrolyte. In this configuration, the charge/discharge cycling performances of the porous NiO microtubule electrode were evaluated at a current density of 1 $A \cdot g^{-1}$ and 3 $A \cdot g^{-1}$. After 500 cycles at the lower current density, the biotemplated NiO electrode provided a stable reversible capacity of as high as 920 $mA \cdot h \cdot g^{-1}$, only reducing at 600 $mA \cdot h \cdot g^{-1}$ when measured at 3 $A \cdot g^{-1}$, but still proving higher capacity and stability compared to other studies. [294-297] Subsequently, to evaluate the practical electrochemical application, a LIB full cell was constructed using the prepared biomorphic NiO material as the anode and commercially available $LiCoO_2$ as a cathode. After 30 charge-discharge cycles at a current density of 200 $mA \cdot g^{-1}$, the reversible capacity was still around 663 $mA \cdot h \cdot g^{-1}$, further demonstrating the ability to light up a LED bulb.

As stated for the previously cited pseudocapacitors, the improved lithium storage performance of cotton-templated NiO was attributed to two main aspects: the nano-sized structure of the crystals and the porous architecture of the microfibers. Indeed, nanocrystals provided larger surface of interaction and a facilitated pathway for the transport of both lithium ions and electrons. Meanwhile, the porous structure acts as a favourable configuration for the accommodation of large volume changes during charging/discharging processes, consequently improving the electrode stability and the cycling performance.

From these promising results a greater investment in the study for biomorphic TMOs to be used electrode materials in LIBs should be pursued. Very few articles have turned their attention in this direction, although the use of lignocellulosic and natural waste materials could lead to the reduction in the costs of battery production together with enhanced performance.

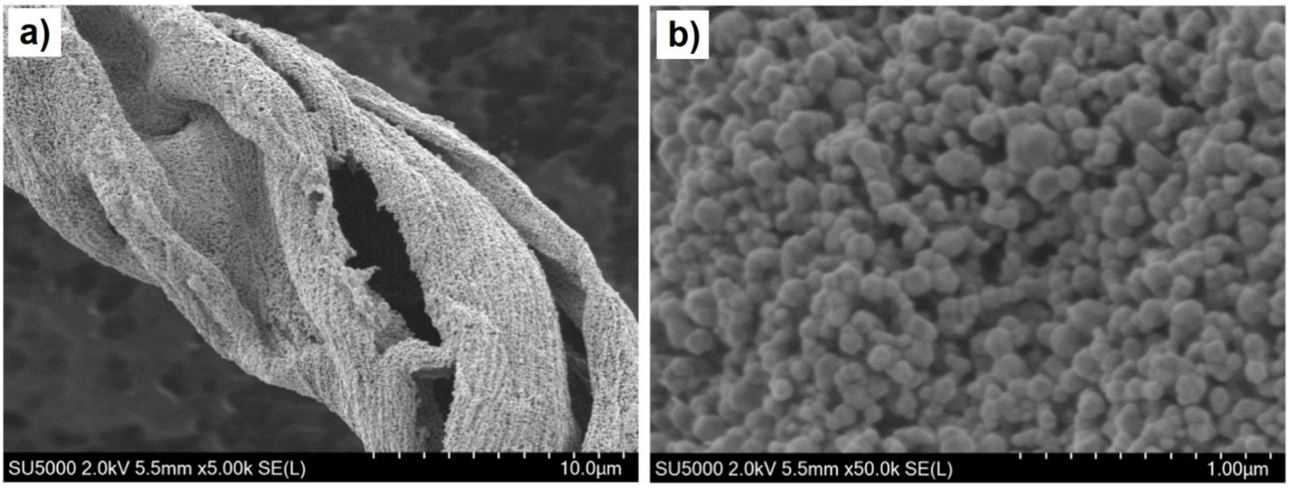

Figure 37 *– SEM images of cotton templated NiO microtubes [243]*

Beside energetic production and conservation, TMOs have found attractive applications also as catalysts for pollutants degradation. An emerging class of contaminants that is receiving attention nowadays is pharmaceuticals, also know as persistent organic pollutants (POPs) or emerging pollutants. [298] The occurrence of drug residues in nature, especially in the aquatic environment, has been found in a large range of concentrations since common wastewater treatments are insufficient for their complete removal. [299] Among pharmaceutical drugs, acetaminophen (also called paracetamol) is one of the most used thanks to its action as a pain reliever and fever reducing drug. As a result, its wide use led to the release of large amount of acetaminophen residues in water, reaching considerable concentrations of 10 $\mu g \cdot L^{-1}$ in natural water [300] and rivers (65 $\mu g \cdot L^{-1}$ in the Tyne River, UK). [301] Acetaminophen's toxicity in organisms is obtained at high dosage, when its toxic metabolic intermediate N-acetyl-p-benzoquinone imine (NAPQI) cannot be readily eliminated by the target organism. [302] Accumulation of paracetamol in the food chain could thus result in a serious environmental problem. Therefore, effective methods for the removal of this pharmaceutical form aqueous solutions are urgently required.

Palas et al. [236] showed two efficient ways to catalytically degrade acetaminophen with the use of three different oxides of *d*-block transition elements such as CuO, Fe_2O_3 and Co_3O_4, prepared using pollen grains as a template material. Biomophous TMOs were obtained following the typical infiltration-calcination procedure, and the resulting product retained the spherical shape of the original pollen for all the oxides prepared (Figure 38). Despite the thermally induced shrinkage, the surface structure of the catalysts was similar to the natural shape of the pollen grains, showing highly porous and interconnected morphology.

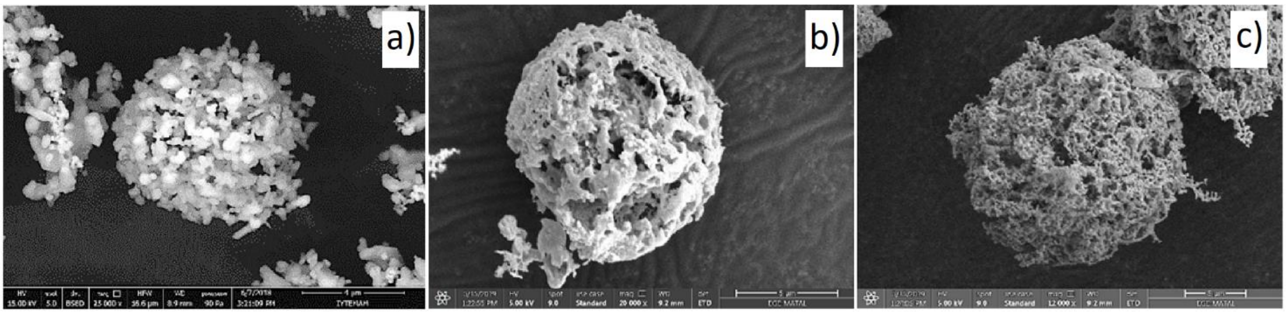

Figure 38 *– SEM micrograph of pollen-templated a) CuO, b)* Fe_2O_3 *and c)* Co_3O_4 *[236]*

Photo Fenton-like oxidation and catalytic wet air oxidation (CWAO) processes were the tested methods for the degradation of acetaminophen. The former method bases its action onto the reaction between the positively charged metal and hydrogen peroxide with the formation of radical species, capable of degrading the pollutant (Scheme 10). [303] The photo Fenton-like oxidation efficiency can be improved through the irradiation of the catalyst with UV-C light. [236] The latter CWAO process consists of the conversion of the hazardous organic compounds into CO_2 and H_2O using O_2 as an oxidant agent and operating under mild temperature and pressure condition, thanks to the presence of the catalyst. [304]

$$\text{metal}^{n+} + H_2O_2 \longrightarrow \text{metal}^{n+1} + HO^{\bullet} + HO^{-}$$

***Scheme 10** – General Fenton reaction*

In Palas et al.’s work, different UV light intensities (6 and 12 Watt), catalyst loadings (0.05 and 0.1 g·L^{-1}) and H_2O_2 concentrations (0.5, 1 and 1.5 mM) were tested for the photo Fenton-like oxidation against a solution of 10 mg·L^{-1} of acetaminophen, while the operating temperatures (150 and 180 °C) and the catalyst loadings (0.25, 0.5 and 1 g·L^{-1}) were varied during CWAO treatment on a 100 mg·L^{-1} solution of paracetamol.

Good results for drug photodegradation were obtained for both Fe_2O_3 and CuO microspheres when the catalyst amount was 0.05 g·L^{-1}, degrading respectively 83.2% and 82.2%, while Co_3O_4 only reached 51.2% degradation. The highest performance was achieved for copper(II) oxide when its concentration was increased up to 0.1 g·L^{-1}, giving a degradation of 86.9%, against 74.6% for iron(III) oxide and 49.1% for Co_3O_4. The decrease in pollutant removal efficiencies for Fe_2O_3 and Co_3O_4 could be due to the reduced light penetration in the solution, caused by an increased darkening of the reaction medium. Above a certain level of catalyst concentration turbidity of the mixture increases and the light cannot penetrate sufficiently into the solution, thus decreasing catalyst activation [305, 306].

The CWAO process showed initially worse results than photo Fenton-like oxidation, even at the highest temperature, reaching pollutant degradation of only 61.2%, 51.7% and 50.2% for CuO, Fe_2O_3 and Co_3O_4, respectively. However, when the catalyst loading was increased from 0.5 g·L^{-1} to 1 g·L^{-1}, the catalytic wet oxidation of paracetamol improved up to 98.3% when biomorphous CuO microspheres were used.

In addition to the degradation studies, to confirm the harmlessness of the final solutions, toxicity tests were carried out measuring the growth of *Lepidium sativum* roots in the medium treated through the CWAO process in the presence of CuO as catalyst. The root growth inhibition was calculated to be 18.5%, which was lower compared to other previous studies that reached 23.7% and 73.7% [307, 308], indicating a relatively low toxicity of the solution. This study demonstrated how the synthesis of different TMOs can be easily performed using pollen as template, obtaining promising materials that can find applications in the field of catalysis usuable at such low levels that they are not significantly harmful to the environment.

Another proof that bio-inspired TMOs materials are promising candidates for green technology applications of wastewater treatment come from the studies of conversion of toxic 4-nitrophenol (4-NPh) to the more useful product 4-aminophenol (4-APh), performed by Alghool et al. [270] and Purbia and Paria. [233] 4-NPh is a phenolic compound used as pH indicator, enzyme detector and as intermediate for the production of other chemicals. Indeed, the reduction of 4-NPh in the presence of $NaBH_4$ leads to the formation of 4-APh, an important precursor of paracetamol. However, the reaction in the presence of sodium boron hydride alone takes long time to complete; therefore, catalysts are required to increase the efficiency.

Alghool et al. [270] synthesized vanadium(V) oxide (V_2O_5) nanoparticles, exploiting cotton as a sacrificial template, for the catalytic conversion of 4-NPh in into 4-APh. V_2O_5 is one of the most important oxides of vanadium with many applications in industrial fields. [309] Moreover, in recent years, promising applications in the fields of solar energy [310], sensing [311] and supercapacitors [271] have been reported, increasing the interest in this transition metal oxide. In Alghool et al.'s study, the fibers of cotton served as guide for the formation of a microtubular structure, composed of spherical/rod-like nanoparticles (∼20 nm sized) of pure V_2O_5.

The catalytic study on 4-nitrophenol reduction proved the long extent of the reaction times and the simple formation of 4-nitrophenolate when only $NaBH_4$ was present in the reaction mixture (Figure 39a). On the contrary, when biomorphous vanadium(V) oxide was added to the solution, the decrease in the absorbance of 4-nitrophenolate (peak at ∼400 nm) and the increase in the absorbance of 4-APh (peak at ∼300 nm) over time proved the catalytic action of the V_2O_5 material (Figure 39b). Nevertheless, the reduction stopped after 18 minutes, still showing the band of 4-nitrophenolate, and a very low degradation constant rate was measured ($3.67 \cdot 10^{-4}$ s^{-1}). These results showed how V_2O_5 could be an interesting compound for catalytic reduction applications, but additional investigations to improve its efficiency are required.

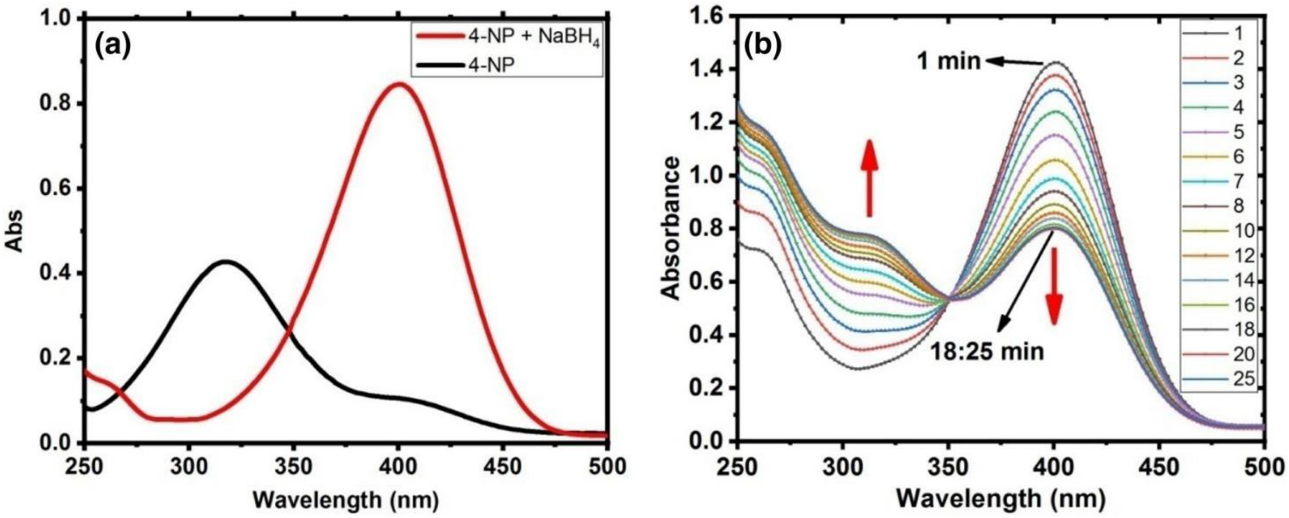

Figure 39 *– a) UV-visible absorption spectra of 4-NPh before and after the addition of $NaBH_4$ (403 nm peak of 4-nitrophenolate) and b) time dependent UV-visible spectra of 4-NPh in presence of $NaBH_4$ and V_2O_5 [270]*

Noble metal nanocrystals, such as Au, Ag and Pd, have been demonstrated to be better performing materials for the catalytic reduction of 4-nitrophenol to 4-aminophenol. [312] However, one of the main drawbacks using these elements as catalysts are the tedious, and sometimes dangerous, separation processes required to recover them. In Purbia and Paria's work [233], noble metal nanoparticles attached to magnetic cotton-templated γ-Fe_2O_3 have been shown to be effective for the conversion of 4-NPh into 4-APh, proving the possibility of obtaining highly efficient catalysts with very good recyclability properties by exploiting common waste materials or by-products. The synthesis procedure is reported in Figure 40 and involved the use of two biological ingredients: cotton fibers and green tea leaf extract. Initially a cotton sample was dipped into a $FeCl_3$ solution. The positively charged Fe^{3+} ions, attracted by the large number of oxygen rich polar groups of cotton, were deposited onto the surface of the template. Subsequently, the addition of a polyphenol-rich green tea extract reduced Fe^{3+} into Fe^{2+}. Polyphenols present in the extract possessed sufficient potential to reduce the ferric ion into the ferrous ion. [313, 314] The oxygen present in the reaction medium rapidly re-oxidized Fe^{2+} into more crystalline iron oxyhydroxides (FeOOH). Eventually, the calcination process at 500 °C led to the formation of pure tubular γ-Fe_2O_3 with a specific surface area of 90 $m^2 \cdot g^{-1}$, a tube diameter of ~5 µm and a wall thickness of ~250 nm. The final deposition of Au/Ag/Pd nanoparticles on the iron oxide tubes was performed by mixing the synthesized γ-Fe_2O_3 samples with a $HAuCl_4$/$AgNO_3$/Na_2PdCl_4 solution, again in presence of the reducing tea extract solution.

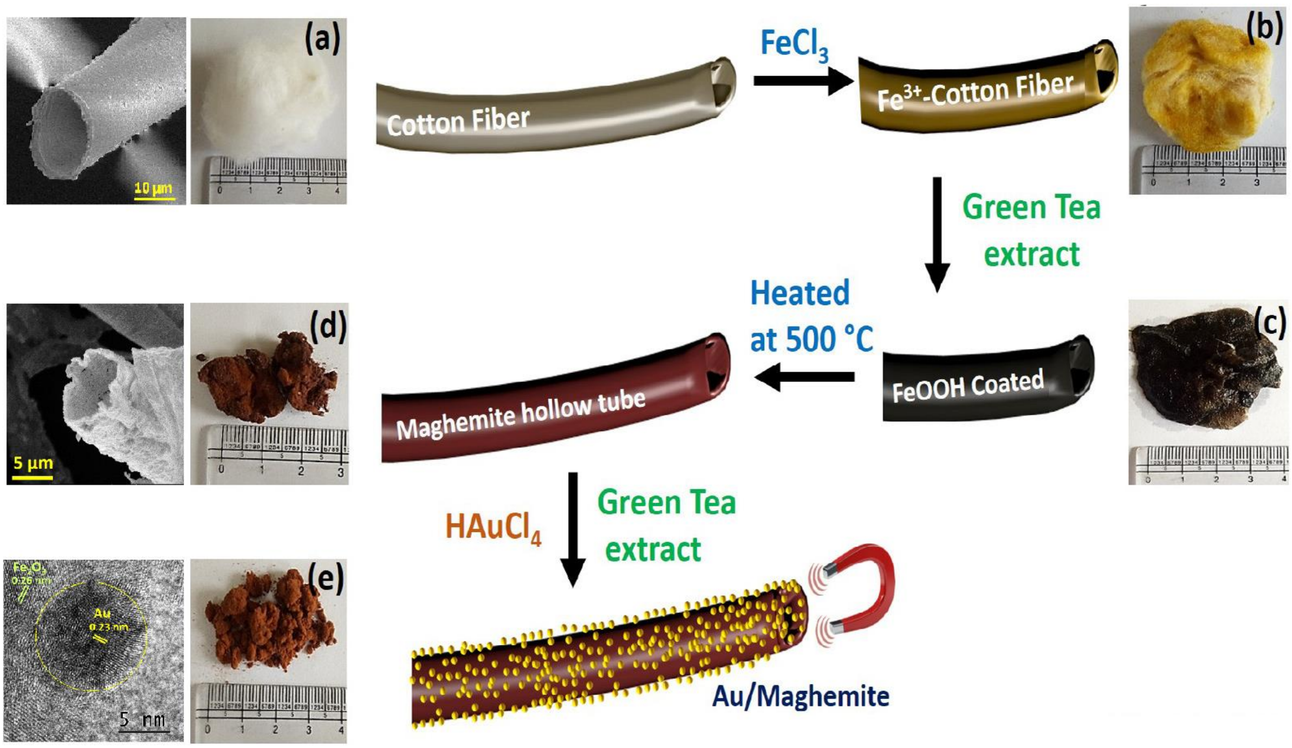

***Figure 40** – Schematic diagram for the synthesis of Au-decorated γ-Fe_2O_3 microtubes. Modified image from ref. [233]*

The attached noble metal NPs possessed a very small size of 2 ± 1 nm, 7 ± 2 nm and 15 ± 2 nm for Pd, Au and Ag, respectively. This difference between the nanoparticle dimensions is one of the reasons for the different results obtained for the catalytic conversion of 4-NPh to 4-APh in the presence of $NaBH_4$. Indeed, the smallest Pd NPs showed the best performance (total conversion in 180 s), followed by Au and Ag (total conversion in 240 s and 330 s, respectively) (Figure 41a-c). Moreover, Pd presented the largest rate constant compared to the other samples (K_{Pd} = 0.0114 s^{-1}, K_{Au} = 0.0047 s^{-1}, K_{Ag} = 0.0030 s^{-1}; Figure 41d). To confirm that the reduction of 4-nitrophenol was caused by the action of noble metal NPs, a catalytic study was performed also only in presence of pure tubular γ-Fe_2O_3. The resulting UV-visible spectra is reported in Figure 42a and it is clearly visible that even after 10 minutes only the characteristic absorption peak of 4-nitrophenolate ions was present, without any sign of conversion.

The presence of the γ-Fe_2O_3 maghemite phase was of extreme importance for the recovery of the catalyst through the use on an external magnet (inset in Figure 42b). The reduction of 4-NPh was repeated for 6 cycles with the use of recycled Au-deposited γ-Fe_2O_3 microtubes, and only a 0.29% decrease in catalytic activity was measured. This study proved the possibility to use sustainable resources, such as cotton fiber and green tea extracts, to prepare iron nanotubes with the important characteristics of large surface area and magnetic behaviour, that can be positively applied as catalyst scaffolds also in other situations.

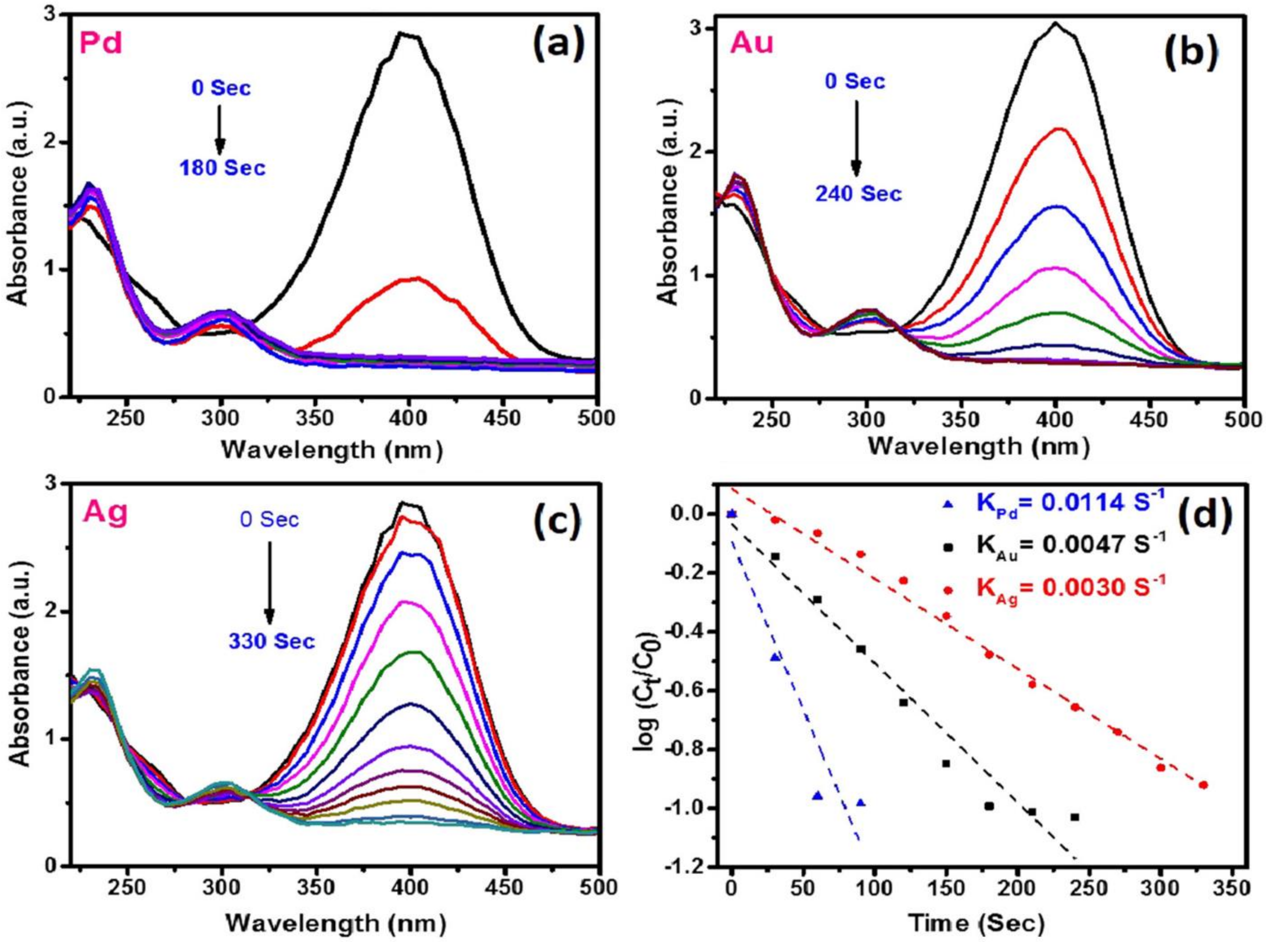

Figure 41 *– UV-visible spectra of catalytic reduction of 4-NPh performed by a) Pd-decorated γ-Fe_2O_3 microtubes, b) Au-decorated γ-Fe_2O_3 microtubes, c) Ag-decorated γ-Fe_2O_3 microtubes; ln(C_t/C_0) against the reaction time for the catalytic hydrogenation of 4-NPh of different [233]*

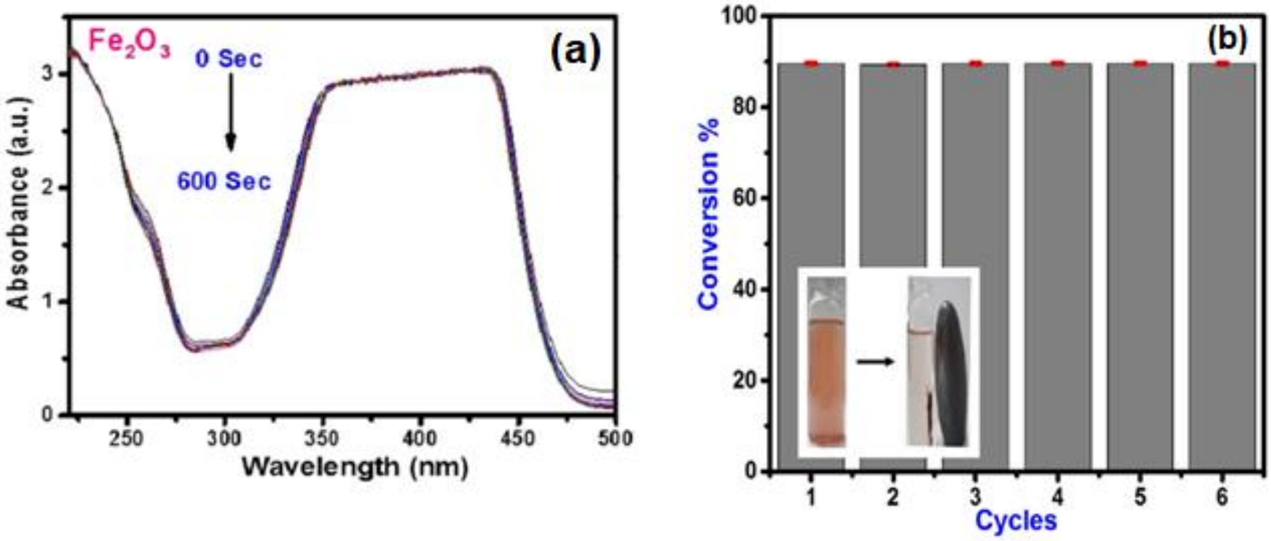

Figure 42 *– a) UV-visible spectra of catalytic reduction of 4-NPh performed by pure γ-*Fe_2O_3 *microtubes; b) conversion of 4-NPh using recycled Au-decorated γ-*Fe_2O_3 *microtubes [233]*

From the research discussed here it is possible to state that the combination of the unique properties of transition metal oxides and the morphology of natural templates can lead to the production of interesting high-performance oxide/ceramic materials in various fields of application. However, until now, very few articles focus their attention on the exploitation of wood and leaves as sacrificial scaffolds, and even fewer investigate their possible use in industrial fields. Wood, with its hierarchical cellular structure, could provide the perfect guide to produce TMO ceramics with large surface area and interconnected pores. Using the proper infiltration and heating procedures, the production of less fragile samples could be possible, easier to handle, and which maintain the complex porous network of natural wood materials.

4.5 Biomorphous oxide ceramics from other post-transition metals (Al, In and Sn)

Post-transition metals are a set of elements whose composition is not yet well defined by the International Union of Pure and Applied Chemistry (IUPAC). In the periodic table, they are located between the transition metals to their left and the metalloids to their right. [315] They show characteristics in between the two groups, presenting mechanical strength, melting and boiling points generally lower than the former, but larger than the latter. Post-transition metals typically completely fill their *d* orbitals and, therefore, base their chemistry on reactions which include *s* and *p* orbitals.

Like the previously listed transition elements, also post-transition metals can give rise to ceramic oxides through reactions with oxygen. In their case, however, very few types of oxide have been prepared using lignocellulosic materials as templates. The only post-transition metal oxides obtained through substitution methods starting from biological templates are aluminium(III) oxide, indium(III) oxide and tin(IV) oxide.

Aluminium(III) oxide, also commonly referred to as alumina, is an oxide form of aluminium with chemical formula Al_2O_3. It is an amphoteric compound which presents electrical insulation characteristics and relatively high thermal conductivity. In bulk form, it generally finds use in refractories, ceramics, polishing and abrasive applications. [316] Moreover, thanks to its bioinert nature, good mechanical properties and excellent resistance to wear, alumina has been used as a material for the production of artificial implants. [317]

When Al_2O_3 is nanosized, a new set of interesting properties and consequent applications appear. Indeed, nanoparticles of alumina have found promising applications as adsorbents of fluoride and metal ions from aqueous solutions [318, 319], stabilizers for optoelectronic applications [320], antimicrobial agents [321] and as catalyst supports [322].

Indium(III) oxide (In_2O_3) is a post-transition metal oxide widely studied as a good transparent conducting oxide material. In_2O_3 is mostly found in the cubic crystal form of the bixbyite structure. The unit cell is composed of 80 atoms, 32 of which are indium while the remaining 48 are oxygen. This crystal configuration could provide the formation of various oxygen vacancies which are considered responsible for the excellent electrical conductivity of indium oxide. [323] When an In_2O_3 ceramic presents high crystallinity, it exhibits very large optical transmittance, becoming highly transparent to visible light. Depending on the degree of crystallinity, thickness of the material, stoichiometry, grain size and presence of impurities, the optical transmittance and the electrical conductivity of indium oxide can be modulated. [324] Thanks to these unique characteristics, In_2O_3 composites find applications as coating materials for photovoltaic devices [325], electrochromic windows [326], sensors [327], and many other electro-optical related applications.

Tin(IV) oxide, also called stannic oxide or tin dioxide (SnO_2), is a light-gray ceramic with peculiar characteristics that make it an important material in high-tech applications. SnO_2 is the most abundant and most thermodynamically stable form of tin oxide. [328] The common crystal configuration of tin dioxide is the tetragonal rutile structure, composed of an Sn^{4+} ion disposed at the center of a distorted octahedra of oxygen ions. [329] SnO_2 is an n-type semiconductor which shows unique optical transparency and high conductivity. These properties make SnO_2 a widely investigated material for the production of electronic devices such as lithium-ion batteries [330], gas sensors [331] and dye-sensitized solar cells (DSSCs). [332]

Table 10 – Post-transition metal oxide ceramics obtained using lignocellulosic-template synthesis

Material	Biotemplate	Morphology	Property	Ref
Al_2O_3	Wood (Rattan and Pine)	Highly porous	/	[40]
Al_2O_3	Wood (Rattan)	Highly porous	/	[333]

Table 10 – Continued

Material	**Biotemplate**	**Morphology**	**Property**	**Ref**
Al_2O_3	Wood (Rattan and Pine)	Highly porous	/	[334]
Al_2O_3	Wood (Pine)	Highly porous	/	[116]
Al_2O_3	Wood (Various)	Highly porous	/	[138]
$Eu/SrAl_2O_4$	Wood (Pine)	3-DOM	Phosphor material	[335]
Al_2O_3	Fibers (Jute)	Hollow microfiber	/	[336]
Al_2O_3	Fibers (Cotton)	Hollow microfiber	/	[337]
Al_2O_3	Fibers (Cotton)	Hollow microfiber	/	[338]
Al_2O_3	Fibers (Cotton)	Hollow microfiber	/	[339]
Ag/Al_2O_3	Fibers (Cotton)	Hollow microfiber	/	[340]
$AlCl_3/Al_2O_3$	Fibers (Cotton)	Hollow microfiber	Catalytic application	[322]
Fe_2O_3/Al_2O_3	Fibers (Cotton)	Hollow microfiber	/	[341]
Al_2O_3	Leaves (Ginko biloba)	Nanosheet	/	[342]
Al_2O_3	Leaves (Liriope)	Highly porous	Adsorption of pollutants	[343]
In_2O_3	Fibers (Cotton)	Hollow microfiber	Gas-sensing	[344]
In_2O_3	Fibers (Cotton)	Hollow microfiber	Gas-sensing	[345]
Indium Tin oxide	Fibers (Cotton)	Flexible monolith	Conductive network	[346]
SnO_2	Fibers (Kapok)	Hollow microfiber	Dye-sensitized solar cells	[347]
SnO_2	Fibers (Cotton)	Hollow microfiber	/	[348]
SnO_2	Fibers (Cotton)	Hollow microfiber	Gas-sensing	[349]
$ZnSnO_3$	Fibers (Cotton)	Hollow microfiber	Gas-sensing	[350]
SnO_2	Pollen (Peltophorum pterocarpum)	Hollow microsphere	/	[351]
SnO_2	Pollen (Rape)	Hollow microsphere	Gas-sensing	[352]
SnO_2	Leaves (Stahlianthus involucratus)	Highly porous	Gas-sensing	[353]

Al_2O_3 ceramics have been prepared using a wide variety of lignocellulosic templates, but only in a few cases the possible practical applications have been tested. In Wang et al.'s work, [343] a biomorphic Al_2O_3 ceramic was prepared exploiting Liriope leaf as the template material, and used for the adsorption of acid fuchsin and methyl orange dyes in aqueous solution. The substitution process led to the precise replica of the biological template microstructure, forming alumina samples which retained the characteristic porous hierarchical architecture of the leaf. The leaf-templated Al_2O_3 ceramic showed optimal adsorption properties toward acid fuchsin dye, reaching a removal of 96% after 4 minutes from a 40 $mg \cdot L^{-1}$ concentrated solution.

Nevertheless, the material did not present good interaction with methyl orange, providing no adsorption activity toward this dye. The reason for this behaviour is based upon the point of zero charge (pH_{ZPC}) of alumina and the chemical structure of the two dyes. Al_2O_3 has a pH_{ZPC} of 7.9; therefore, it is slightly positively charged in a neutral water solution. Acid fuchsin and methyl orange, instead, present negative charges when are dissolved in water. The larger number of negative charged oxygens in acid fuchsin molecule makes it more prone to interact with alumina, managing to be adsorbed even at neutral pH. On the contrary, methyl orange, due to the presence of a single negative charge in its structure, requires a more positively charged surface to be captured.

To enhance the adsorption of methyl orange dye, Wang et al. acid-modified the alumina surface through the immersion of the biotemplated Al_2O_3 ceramic into a HCl solution. This treatment did not alter the microstructure of the sample, leaving its porous hierarchic structure intact, but increased the surface acidity by introducing more H^+ ions onto the alumina surface. Indeed, after the acid-modification, the removal of methyl orange reached the 80% within 2 minutes, together with a rapid decolouration of the contaminated solution.

The widely interconnected network provided by the lignocellulosic template offers an ideal guide to create materials with large surface area for adsorption. From the good adsorption results obtained by Wang et al., further research could be developed into the combination of the absorption capability of alumina with the possibility of its use as a catalyst support, doping it with more photoactive compounds for the subsequent degradation of contaminants.

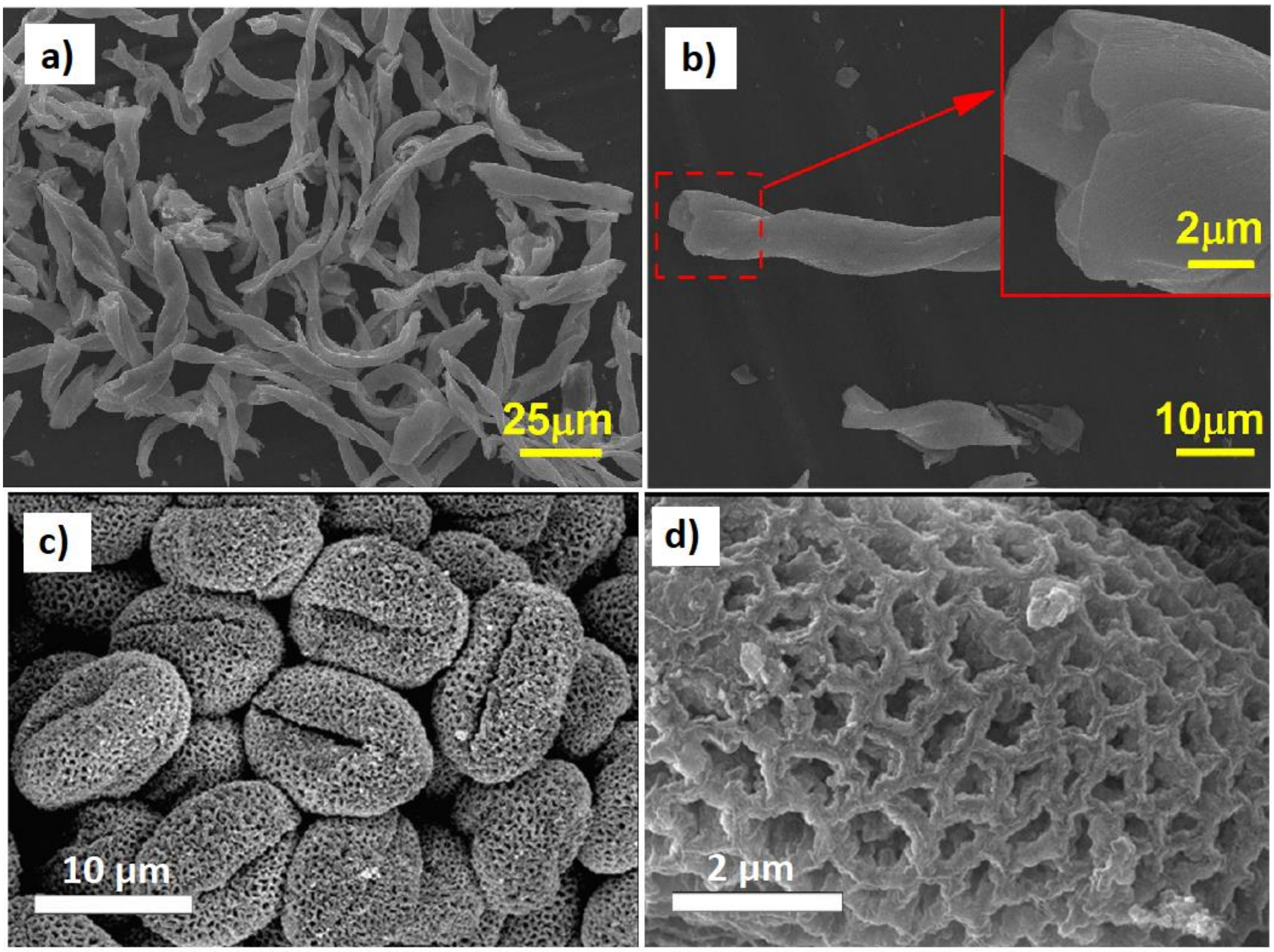

Figure 43 *– SEM images of a, b) cotton-templated* In_2O_3 *microtubes [344] and c, d) pollen-templated* SnO_2 *microspheres [352]*

In_2O_3 and SnO_2 are post transition oxide ceramics that have shown interesting capacities in gas sensing applications. Keeping in mind the principles of gas sensing described in Chapter 4.3, both In_2O_3 and SnO_2 materials present enhanced sensing properties thanks to the possible formation of a large number of oxygen vacancies (V_o) in their crystal structure. Furthermore, biomimicking a natural structure could allow for the creation of materials with large surface area and porous architecture optimal for the percolation and adsorption of gasses. For these reasons, in Ma et al.'s work [344] and Song et al.'s work [352], indium oxide and tin dioxide ecoceramics were respectively prepared using cotton fibers and pollen grains (*Brassica capestris*) as templates, for the detection of harmful gasses. Both the products retained the original features of the lignocellulosic materials, showing in the first case hollow In_2O_3 microtubes of 50–70 µm in length and 5–6 µm in diameter, while in the second case porous SnO_2 ellipsoidal microspheres of 8 µm in length and 12 µm in diameter (Figure 43).

The BET surface area of biomorphic In_2O_3 microtubes was much larger than that of non-templated ceramic (11.65 $m^2 \cdot g^{-1}$ vs 0.55 $m^2 \cdot g^{-1}$). Moreover, the amount of V_o in the former sample was higher than the non-templated ones (24.72% vs 16.11%), thus indicating the presence of more active centers that could be provided for gas adsorption. [354] In case of biomimicking SnO_2 microspheres, the BET surface area was around 94.1 $m^2 \cdot g^{-1}$, which was much larger compared to the non-templated sample that reached only 13.12 $m^2 \cdot g^{-1}$.

Thanks to these improved characteristics and the mesoporous nature of both the bio-templated In_2O_3 and SnO_2 ceramics, the gas sensing testes performed on these materials gave very good results. Biomorphous indium(III) oxide microtubes exhibit an excellent selectivity toward the detection of Cl_2, reaching a sensitivity of around 1050 and a response and recovery time of respectively 10 s and 18 s, when the sensor was exposed to 10 ppm of the gas at the low working temperature of 200 °C. Moreover, the limit of detection, extrapolated from the fitting line obtained from the analysis performed at different gas concentrations, achieved the very small value of 0.323 ppm.

On the other hand, pollen-templated SnO_2 microspheres displayed optimal sensing properties toward NO_2 gas, obtaining a sensitivity value of 219.5 and a response and recovery time of respectively 5 s and 111 s, when they were subjected to 50 ppm of the gas at the working temperature of 330 °C. Moreover, when the gas concentration was decreased down to 10 ppm the sensitivity still presented good results of around 100. These detection results of biomorphic SnO_2 toward NO_2 were superior compared to those obtained from Hamrouni et al.'s work [198] reported in Chapter 4.3. This fact could be due to the larger specific surface area of SnO_2 microspheres, or to the different chemical nature of the sensor which made tin dioxide a material more prone to the adsorption of NO_2 compared to ZnO. More investigations could be performed in this direction.

Another application in which SnO_2 has displayed promising results is the conversion of solar light into electrical energy, when used as dopant in dye-sensitized solar cell (DSSC) devices. DSSCs are innovative devices capable of producing electricity, exploiting the solar energy with high efficiency and low cost. [355] Their working principle is based on the photoexcitation of dye molecules adsorbed on the surface of a thin film of semiconductor material, such as TiO_2, ZnO or SnO_2, which acts as an anode electrode in a photovoltaic cell. [356, 357] The cell is composed of three main parts: a layer of dye-sensitized nanocrystalline semiconducting particles (TiO_2 NPs are the most widely employed) on a conducting substrate, an electrolyte (usually I_3^-/I^-) in organic solvent(s) and a platinum counter electrode (Figure 44). Under solar irradiation, electrons from the lowest unoccupied molecular orbital (LUMO) of the dye are excited into the conduction band of the titania film through a metal-to-ligand charge transfer pathway. Afterwards, the I^- ions reduce the oxidized dye to its original state, oxidizing in turn into I_3^- anions. The final step is the regeneration of I^- ions by the action of platinum counter electrode, thus recreating the conditions for a new cycle. [358]

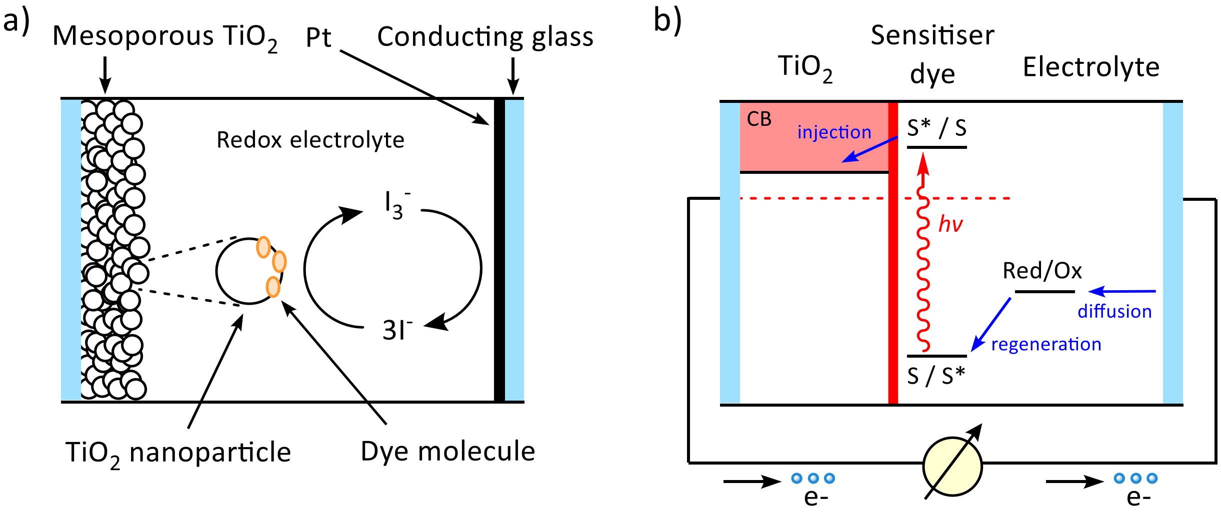

Figure 44*- a) Schematic overview of a dye-sensitized solar cell (DSSC) and b) its energy level diagram*

In Jin et al.'s work, [347] SnO_2 hollow microtubes have been prepared using kapok fibers as a template and applied as additives in the TiO_2 photoelectrode of a DSSC. After the impregnation of the natural fibers into an $SnCl_2$ solution and the formation of an SnO_2 gel layer through hydrolytic reaction in the presence of water, the organic content was removed by calcining the samples at 600 °C. The resulting SnO_2 hollow microfibers retained the original structure of the kapok fibers, showing an inner diameter of ~10 μm and a high crystallinity.

The incorporation of tin dioxide microtubes in the TiO_2 electrode matrix lead to the formation of a larger number of pores on the surface of the material compared to non-templated SnO_2 nanoparticles. Moreover, the biomorphic SnO_2 microtubes placed in the titania photoelectrode preserved the fibrous form even after the electrode preparation. The efficiency (η) of the biotemplated SnO_2/TiO_2-based DSSC showed a maximum solar power conversion of 5.43%, presenting an improvement with respect to the pure TiO_2 photoelectrode based DSSCs (η = 4.89%). Indeed, the presence of tin dioxide acted as an energy barrier and increased the physical separation between injected electrons and oxidized dyes/redox couples, successfully retarding the recombination reactions in the TiO_2-NP photoelectrode. [347] In addition, the hollow structure of SnO_2 microfibers offered a larger specific surface area, improving the absorption capacity for dye molecules, the seepage of electrolyte, the charge transfer and the solar conversion efficiency. [359]

Most work performed on the transformation of lignocellulosic templates into post-transition metal oxide ceramics is based on the use of fibers (mainly cotton) as a sacrificial scaffold. Less effort has been made into the conversion of wood, pollen or leaves, especially regarding indium and tin oxides. The hierarchical porous structure of wood could potentially be an optimal scaffold for the preparation of highly interconnected ceramics suitable in various fields of application and, therefore, more investigation should be performed in this direction. Furthermore, the extensive research carried out in the production of biomorphic Al_2O_3 ceramics has only been slightly accompanied by practical investigations, especially in the biomedical field. Therefore, more in-depth studies for this type of materials could be an interesting pathway to explore.

4.6 Biomorphous oxide ceramics from alkaline earth metals (Ca and Mg)

Alkaline earth metals are those elements composing the second group of the periodic table. Except for beryllium, all alkaline earth elements have very similar chemical properties, much of their chemistry being governed by the tendency to lose two electrons. [360] With the contribution of thermal energy, alkaline earth metals react with oxygen to produce their corresponding oxides, composed of positively charged metal ions (M^{2+}) strongly bonded to negatively charged oxygen ions (O^{2-}) through ionic interaction. Consequently, alkaline earth oxides possess a regular structure of the same type of NaCl, in which single ions in the crystalline network are surrounded by the maximum possible number of ions with the opposite charge. [361] In this form, the atoms on the surface, edges and corners have lower coordination numbers and, therefore, when alkaline earth oxides are nanosized, these positions offer a greater chance to behave as catalytic active sites. This phenomenon caused the alkaline earth oxides in the form of nanoparticles to be heavily investigated as optimal heterogeneous catalysts. [361, 362]

The most abundant alkaline earth metals present on the earth's crust are calcium (Ca) and magnesium (Mg). These two are also the only elements that have been studied for the production of biomorphic oxide ceramics through the use of lignocellulosic biomass. Calcium oxide (CaO), also called quicklime, and magnesium oxide (MgO), also named magnesia, are the oxidized forms of calcium and magnesium, respectively. They are generally produced through the thermal decomposition of the corresponding carbonate or hydroxide compounds at temperatures above 800 °C. Both oxides are environmentally friendly, non-expensive, easy to manufacture and handle, with low solubility and high basicity, that have found interesting applications in various industrial fields.

In recent years, MgO has shown promising applications as an insulating material, pollutant adsorbent and antimicrobial agent, in addition to its more common use in the formation of cements and as an additive in concrete. [361, 363-365] On the other hand, CaO, which had also been used as an important ingredient in cements, has found applications in advanced areas such as heterogeneous catalysis and acid regulation in food. [366] Furthermore, current attention towards CaO have moved to its use as a catalyst for biodiesel production and as promising material for CO_2 capture. [367-370]

Another valuable calcium-based ceramic, which has gained increasing attention since the 1970's, is hydroxyapatite (HA), a naturally occurring phosphate mineral with chemical formula $Ca_{10}(PO_4)_6(OH)_2$. Due to its similar chemical composition to the mineral phase of bone tissues, HA is an important material for artificial bone implants in medical applications. [371] Moreover, in addition to its biological importance, hydroxyapatite is studied for various applications in heterogeneous catalysis, thanks to its ability to form solid solutions and to accept a large number of anionic and cationic substituents. [372]

Such advanced applications of MgO, CaO and hydroxyapatite require the presence of peculiar properties, like large specific surface area and high porosity, to give rise to promising active ceramics. Templating hierarchical porous structures of lignocellulosic samples is an optimal strategy to obtain products with these desired features. So far little research has been performed in this direction, with the production of MgO, CaO and HA ceramics mimicking a small selection of biological templates. Nonetheless, the obtained materials have shown promising results with potential economic advantages, which could lead to greater interest in this type of synthetic technique.

Table 11 – Alkaline earth oxide ceramics obtained using lignocellulosic-template synthesis

Material	**Biotemplate**	**Morphology**	**Property**	**Ref**
CaO	Wood (Spruce)	Highly porous	/	[373]
CaO	Fibers (Cotton)	Hollow microfiber	CO_2 capture	[374]
Al/CaO	Fibers (Cotton)	Hollow microfiber	CO_2 capture	[375]
$CaTiO_3$	Fibers (Cotton)	Hollow microfiber	Adsorption of pollutants	[376]
$CaTiO_3$	Fibers (Sorghum straw)	Highly porous	Adsorption of pollutants	[377]
$Ca_{10}(PO_4)_6(OH)_2$	Wood (Beech)	Highly porous	/	[378]
$Ca_{10}(PO_4)_6(OH)_2$	Wood (Cane and Pine)	Highly porous	/	[379]
$Ca_{10}(PO_4)_6(OH)_2$	Wood (Rattan)	Highly porous	/	[380]
$Ca_{10}(PO_4)_6(OH)_2$	Wood (Pine and Rattan)	Highly porous	/	[381]
$Ca_{10}(PO_4)_6(OH)_2$	Wood (Rattan)	Highly porous	Bioactive scaffold	[382]
$Ca_{10}(PO_4)_6(OH)_2$	Fibers (Cotton)	Microfibers	/	[383]
MgO	Fibers (Cotton)	Hollow microfiber	Catalytic application	[384]
MgO	Leaves (Camphor)	Highly porous	Bacteria removal	[385]

Microbial contamination in medicine has always been a threat for human health, and the research for new, effective and inexpensive solutions to this problem is one of the most explored areas in science. Escherichia coli (E. coli) is a typical Gram-negative bacterium that can exhibit severe harmful consequences to human health, and investigations into new materials for its efficient removal or deactivation are always valuable. [386] Among the various antimicrobial agents researched, MgO could be a potential compound for this purpose. Indeed, magnesium oxide showed excellent physical and chemical removal properties toward negatively charged bacteria thanks to its positively charged nature when immersed in water. [387, 385]

The physical removal of bacteria is enhanced when the structure of the absorbing material displays a highly porous architecture at micro level. To obtain materials with these characteristics, the mimicry of nature is a useful option. In Yang et al.'s work, [385] a hierarchical porous positively-charged MgO ceramic was prepared using camphor leaves as the template material. The MgO ecoceramic was synthsized with the typical impregnation/calcination process, and the obtained product totally maintained the leaf structure at macro and micro scale, resembling a monolithic white leaf (Figure 45). In addition, the template technique led to the formation of a highly porous MgO material with a much larger specific surface area with respect to non-templated samples (57.3 $m^2 \cdot g^{-1}$ vs 6.6 $m^2 \cdot g^{-1}$).

The bacterial adsorption and removal efficiency of the templated and non-templated MgO ceramics were evaluated against a culture of E. Coli bacteria. The capture process was performed via the filtration of a bacterial culture through the material and the subsequent analysis of its growth on Luria broth (LB) agar plates. Leaf-templated MgO ceramic showed an efficient bacterial-removal rate of more than 99%, while non-templated samples and powdered activated carbons reached only 83% and 37%, respectively. The excellent results of the MgO compounds were caused by the advantageous positive charge that magnesium oxide possesses in solution, thanks to its high isoelectric point, compared to carbon. [388] Moreover, the hierarchical porous structure of the leaf-templated MgO sample enhanced the capture capacity compared to the non-templated one, resulting in a quasi-total removal of E. Coli after the filtration process.

The improved capture ability of this biomorphic magnesia ceramic affected in turn its sterilizing capacity. The E. coli sterilization rate of MgO samples was 77% for the ecoceramic compared to only 49% for the non-templated magnesia. The large surface area of the former is indeed a positive factor for the generation and transmission of more antimicrobial chemical species and, therefore, an enhancement for its bactericidal property.

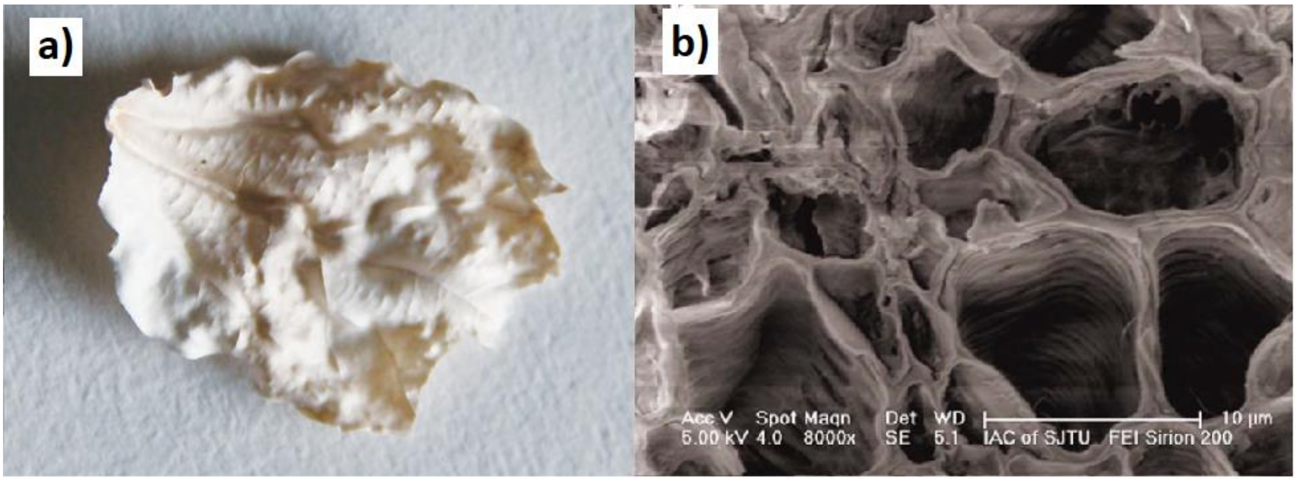

Figure 45 *- a) Photograph of the leaf-templated MgO ceramic and b) SEM image of its microstructure [385]*

Carbon dioxide (CO_2) represents the component of greenhouse gasses that contributes the most to the global worming crisis. In September 2019, the amount of carbon dioxide present in the atmosphere reached a new record level of 408 ppm, showing an increase of around 95 ppm in the past sixty years. [369] A promising solution to fight this issue is the emerging technology of CO_2 capture and sequestration (CCS). CCS technology is ideally composed of three phases: CO_2 capture, transportation and storage. Of the three steps, the first is the most critical, requiring more than 70% of the whole operating costs; therefore, new investigations in this field are urgently required. [370]

The most recent research into CO_2 capture focus attention on the use of solid adsorbents for the entrapment and subsequent controlled release of carbon dioxide. Among the various materials tested for this application, CaO has shown interesting results thanks to its high reactivity with CO_2 and the large availability of low cost and environmental-friendly precursors. [389] The CO_2 capture-release cycle performed by CaO ceramics, also called the calcium looping process (CLP), bases its action on carbonation and calcination reactions of CaO at high temperatures. When CaO interacts with CO_2 at temperatures ranging between 600-800 °C, a carbonation reaction happens and the production of solid $CaCO_3$ occurs (Scheme 11a). However, when the temperature is raised above 800 °C, the calcination of calcium carbonate happens and the regeneration of CaO is achieved through the release of carbon dioxide (Scheme 11b).

The carbonation of CaO is divided into an initial fast chemical reaction-controlled stage, which takes place on the surface of CaO through the nucleation and growth of $CaCO_3$, and a substantially slower diffusion stage, which results in the complete formation of the continuous carbonaceous layer. [370]

At present, one of the main obstacles for the practical application of CLP lies in the sintering process that CaO materials faces after each carbonation−calcination cycle, leading to a dramatic decrease in performance with the increase of cycle number. An effective method to improve the CO_2 capture performance of CaO sorbents is the modification of the microstructure of the ceramics. Increasing the specific surface area and the porosity of the materials provides a larger diffusion area for the gas percolation and, therefore, enhanced CO_2 capture.

$$\text{a) } CaO\,(s) + CO_2\,(g) \longrightarrow CaCO_3\,(s)$$

$$\text{b) } CaCO_3\,(s) \longrightarrow CaO\,(s) + CO_2\,(g)$$

***Scheme 11** – Calcium looping process a) carbonation and b) calcination reactions*

In Wei et al.'s work, [374] CaO ceramics have been prepared through the use of four templates with different origin, shape and size. The templates can be divided in to: natural materials, such as starch (ST, 10−30 μm in length) and cotton fibers (CF, 10−20 μm in diameter and 1000 μm in length), and processed materials, such as carbon nanotubes (CNT, 10−20 nm in diameter and 10−30 μm in length) and carbon nanofibers (CNF, 200−600 nm in diameter and 5−50 μm in length). For all these samples, the CLP performance was evaluated under two different calcination conditions in the cycle: mild calcination conditions (850 °C in the presence of pure N_2) and severe calcination conditions (more similar to industrial conditions, 950 °C in the presence of pure CO_2).

The substitution process led to the production of porous CaO materials which maintained the architecture of the template, but possessing different textural properties. The presence of nano templates led to the formation of samples with smaller crystallite size and slightly larger specific surface area, compared to natural templated CaO composites. Indeed, CNT- and CNF-derived CaO materials showed crystals of 12.91 nm and 14.44 nm in dimension, and with surface areas of 12.17 $m^2{\cdot}g^{-1}$ and 10.87 $m^2{\cdot}g^{-1}$, respectively. In the case of the biotemplated calcium oxide ecoceramics, the crystal sizes and the surface areas were, respectively, 16.25 nm and 9.02 $m^2{\cdot}g^{-1}$ for ST-templated CaO, and 17.71 nm and 8.80 $m^2{\cdot}g^{-1}$ for CF-templated CaO. Moreover, the nano templates produced ceramics with larger pore volume in the range 2-10 nm, while the natural templates led to an increase in the number of wider pores ranging from 10 to 100 nm. These textural diversities were due to the original dimensions of the sacrificial scaffolds, and to the combustion temperatures at which they are degraded. [374]

The best CLP performance under both mild and severe calcination were obtained by CNT-templated CaO ceramics, followed by CNF-templated, ST-templated and CF-templated. After 15 cycles under severe calcination conditions, the CO_2 capture of CNT, CFT, ST, CF-templated CaO ceramics were respectively 0.26 g/g, ∼0.23 g/g, 0.21 g/g and 0.18 g/g. The templated sorbents showed all increased CO_2 sorption performance compared to the non-templated CaO composite, whose CO_2 capture assessed only around 0.13 g/g after 15 cycles under severe calcination conditions. The efficiency trend perfectly followed that of the surface area, demonstrating how this factor is of extreme importance for the calcium looping process.

Moreover, analysis of the relationship between pore volume and CO_2 uptake showed that smaller pores (2-10 nm) are closely related to the carbonation reaction controlled stage, while pores with sizes ranging from 10 to 100 nm are correlated to the diffusion controlled stage.

Although Wei et al.'s biomorphic CaO ecoceramics did not show the best CLP performances among the tested materials, the research proved that the templating method can lead to promising results, thanks to the creation of samples with higher surface areas and porosity than normal synthetic techniques would produce.

In Chi et al.'s work, [375] the templating of lignocellulosic material proved the formation of materials with better CO_2 capture performances compared to non-templated ones. In the cited study, hollow microtubes of Al-doped CaO ceramic were prepared using absorbent cotton as a sacrificial scaffold, demonstrating an improved CLP efficiency, with potentially lower costs compared to the use of pure limestone.

The preparation of Al-doped CaO ecoceramic involved the infiltration of cotton with a homogeneous solution containing Ca^{2+} and Al^{3+} ions (mass ratio of Ca^{2+}/Al^{3+} = 90:10). After a first pyrolytic step under pure N_2, the impregnated cotton was calcined in air at 700 °C to remove the template and leave in its place the synthetic Al-doped CaO sorbent. The X-ray diffraction (XRD) patterns of the resulting material displayed CaO and $Ca_{12}Al_{14}O_{33}$ as the main components. The presence of $Ca_{12}Al_{14}O_{33}$ is known to improve the sintering resistance of the sorbent material and, therefore, increase its cyclic stability. [369, 370] SEM images proved the exact reproduction of the cotton morphology at micro level, showing Al-doped CaO hollow microtubes with diameter ranging from 0.5 to 5 µm, and with a highly porous surface at the nano level (Figure 46).

The calcium looping process was performed under severe calcination conditions (920 °C in 70% CO_2/30% N_2) and demonstrated optimal results, retaining CO_2 capture of approximately 0.41 g/g after 30 cycles and still 0.38 g/g after 50 cycles. Biomorphic Al-doped CaO ceramics exhibited capture performance around 8 times higher than those of limestone under the same conditions and number of cycles. Moreover, these results were better than those obtained by Wei et al. [374], even compared to their best performing nano templated samples. The excellent CO_2 capture performance and sintering resistance of the Chi et al. ecoceramic can be attributed to the combined presence of a hollow microtubular architecture and the presence of the $Ca_{12}Al_{14}O_{33}$ phase.

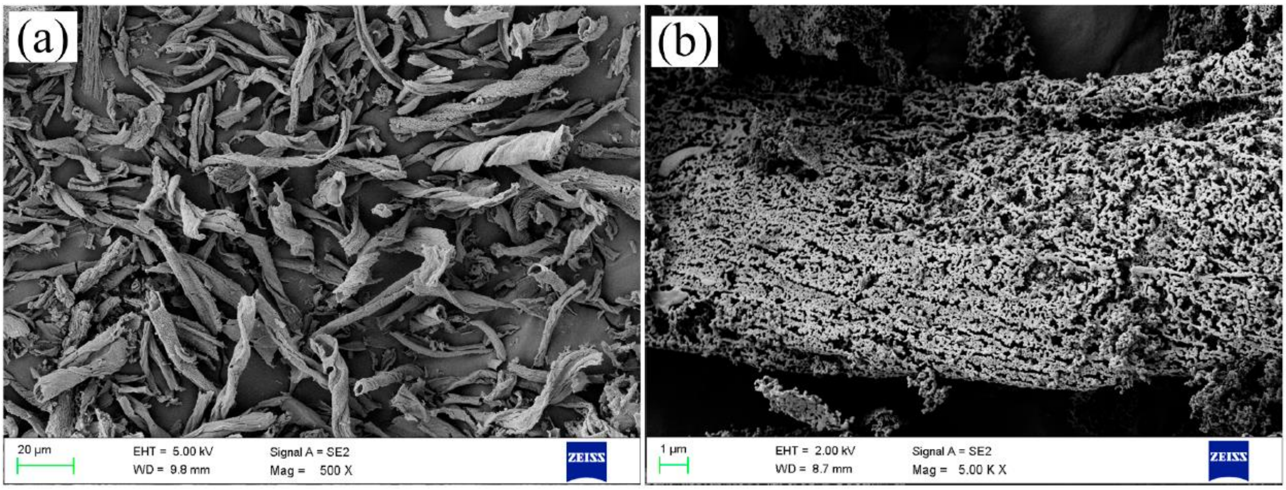

***Figure 46** – SEM images of cotton templated Al-doped CaO ecoceramic [375]*

As mentioned before, hydroxyapatite is an important material which constitutes the mineral phase of bone tissue. For this reason, a lot of research into the synthetic production of bioactive HA to be used in the medical field has been performed. One of the most important features that artificial HA ceramic must possess is hierarchical porosity to allow cell seeding and proliferation when the material is implanted in the target host. This characteristic can be easily found in biological materials which, thanks to their high porosity and structural interconnection, can represent promising templates for the production of bone scaffolds.

In Tampieri et al.'s work [382] bioactive hydroxyapatite (referred as B-HA) has been prepared through the replication of rattan wood pieces via a new synthetic procedure. Initially, the wood sample was pyrolyzed under N_2 to eliminate the organic components and form a porous carbon scaffold. Then, the carbon body was placed to react with metallic Ca granules at high temperature and low-pressure conditions, thus achieving its conversion into pure CaC_2. The resulting product was subsequently heated in air at 900°C to produce CaO, but still maintaining the original porous structure of wood. A carbonation reaction was then performed under supercritical conditions in presence of a flux of CO_2 and H_2O mixture (molar ratio of CO_2/H_2O of ~10) to convert CaO into $CaCO_3$. Finally, the formation of pure hydroxyapatite solid phase was obtained through a hydrothermal ion exchange process that $CaCO_3$ experienced in close contact with a solution of $(NH_4)_2HPO_4$. In addition, to make the HA ecoceramic more chemically similar to natural bones, a conclusive soaking treatment in aqueous solution containing Mg^{2+} and Sr^{2+} ions was carried out.

The procedure performed to produce the HA ceramic was particularly complex, but led to the production of a promising material. The low-temperature supercritical carbonation step allowed the total conversion of CaO into $CaCO_3$ without the occurrence of the pore closure phenomenon which typically takes place with high temperature sintering processes. Moreover, the presence of water in supercritical CO_2 led to the formation of a $Ca(OH)_2$ phase which, in these condition, immediately converted into $CaCO_3$ and allowed the growth of smaller carbonate grains with the consequent increase in the surface area of the sample.

The final biomorphous product showed a hierarchical porous structure, being composed of larger oriented channels with average diameters of ~300 µm and other diffuse smaller pores. At the nano level, the material presented a highly textured surface of hexagonal platelets with thickness of about 20 nm and diameter of ~150 nm. This architecture conferred the ecoceramic an overall porosity of 60% and a specific surface area of 12.30 $m^2 \cdot g^{-1}$.

Tests performed to evaluate the mechanical strength, ion release and *in vitro* cell culture demonstrated that B-HA possessed improved performance compared to a commercial sintered hydroxyapatite sample (referred as S-HA). Increased compression strength and enhanced ion release capacity suggested promising applications of B-HA ceramic as bone replacement with optimal damage-tolerant behaviour and high bio-resorbability. Through a cell viability assay, a very high ratio of viable cells was observed to be adherent to both biomorphic and sintered hydroxyapatite samples, without significant differences. However, the analysis of the gene expression profile of the cells grown on biomorphous B-HA showed an increased expression of genes involved in both early and late stages of osteogenic processes. This fact indicated an improved biocompatibility and activity exerted by the biotemplated HA compared to the commercial S-HA. Final *in vivo* tests demonstrated the excellent osteoinductive ability of the B-HA scaffold, showing well developed bone tissue, formed in an ectopic site 12 weeks after subcutaneous implantation in rabbits. [382]

Until now, little research has been carried out on the production of ecoceramic materials derived from alkaline earth metals. The porous structure that these compounds could acquire by templating the natural architecture of lignocellulosic composites could be of extreme technological interest for many applications. MgO ceramics for thermal insulation or CaO for catalytic biodiesel production could be some of the applications that could be taken in consideration for future investigations. Furthermore, a more detailed study on the CO_2 capture performances of biomorphic CaO exploiting other lignocellulosic materials and different doping elements could give rise to even more efficient materials than those already described.

4.7 Biomorphous SiO_2-ceramics

Silicon oxide (SiO_2), commonly referred as silica, is the most common oxide present on earth, with a mean abundance of about 37 wt%. [390] SiO_2 unit cell possess a tetrahedral conformation, being composed of a central silicon atom covalently bounded to four oxygen atoms. Silica can be found in nature in different crystal structures either crystalline (i.e. quartz, tridymite and cristobalite), cryptocrystalline (i.e. chalcedony) or amorphous (i.e. opals). [391] From the technological point of view, the silica particles extracted from natural resources usually contain metal impurities and, therefore, are not favourable for advanced scientific and industrial applications. [392] For this reason, in recent decades large attention has been given to the production of synthetic silica which can be prepared with various shapes and with different properties, depending on the manufacturing methodologies. Moreover, since the silica surface can be easily functionalized through grafting reactions with numerous organic groups, the multiplicity of silicon-based materials that can be obtained is potentially very large.

The large variety of morphologies that can be achieved for SiO_2 ceramics is reflected in a diversified type of applications. Silica is employed in several fields such as pollutant adsorption, additives in the food industry, catalyst supports, biosensor, drug delivery systems and many others. [393] Among all, drug delivery applications have gained increasing attention thanks to the development of the family of mesoporous silica nanoparticles (MSNs). MSNs are defined as possessing pores ranging between 2 nm to 50 nm. [394]

Such materials can be obtained through the greatly investigated sol-gel processes, and a variety of morphologies including spheres, fibers and hollow structures have already been synthesized. The production of advanced SiO_2 ceramics via sol-gel procedures with hierarchical sophisticated structures is, however, still a challenge. The requirement of surfactants and the complexity in the production of hollow materials with different pore sizes in the same particle make the classic preparation methods a possible obstacle for the production of highly elaborated architectures. To avoid these difficulties, the reproduction of natural lignocellulosic materials could be a valuable solution. Lignocellulosic biomasses indeed present unique hierarchical structure that can provide the optimal guide for the creation of complex morphologies. Moreover, the use of these natural materials, especially those coming from industrial waste, could lead to the reduction in costs and to a lower environmental impact for the synthesis procedure.

Table 12 – SiO_2-ceramics obtained using lignocellulosic-template synthesis

Material	Biotemplate	Morphology	Property	Ref
SiO_2	Wood (Linden)	Highly porous	/	[395]
SiO_2	Wood (Poplar and Pine)	Highly porous	/	[396]
SiO_2	Wood (Poplar and Pine)	Highly porous	/	[397]
SiO_2	Fibers (Cotton)	Hollow microfiber	Adsorption of pollutants	[398]
SiO_2	Pollen (Rape, sweet potato and camellia)	Hollow microsphere	/	[52]
SiO_2	Pollen (Various)	Hollow microsphere	Drug delivery system	[399]
$FePMo_{12}/SiO_2$	Pollen (Camellia)	Hollow microsphere	Photodegradation of pollutant	[400]
Ca/SiO_2	Pollen (Rape)	Hollow microsphere	Drug delivery system	[401]
Co/SiO_2	Leaves (Reeds)	Highly porous	Catalytic activity	[402]

In Zeng et al.'s work [401] hierarchical porous Ca-doped SiO_2 microspheres were prepared through a facile sol–gel replication process using rape pollen grains (*Brassica napus*) as a template, and exploited as a drug delivery device for the release of tetracycline hydrochloride (TCH). After the typical impregnation and calcination treatments, the obtained particles retained the original spherical shape of the pollen grains, showing a shrinkage of ∼50% for both particle diameter and macropore size. Indeed, the average particle diameter and pore size of pollen grains were respectively ∼44 µm and ∼2 µm, while those of Ca/SiO_2 were around 21 µm and 1 µm (Figure 47a). In addition to macropores, Ca/SiO_2 microspheres presented nano pores with average diameter of ∼9.5 nm, derived from the sol-gel procedure and which were not detected on the pollen grains. Furthermore, the templating method resulted in the production of microparticles with larger surface areas compared to non-templated samples, showing BET values respectively of 111.4 $m^2 \cdot g^{-1}$ and 84.2 $m^2 \cdot g^{-1}$.

The improved characteristics of pollen-derived microspheres led to enhanced drug loading and release properties compared to non-templated Ca/SiO_2 samples, and to commercially available bioactive nanoparticles (45S5 Bioglass). The loading efficiency of the biomorphic Ca/SiO_2 microspheres, the non-templated composites and the commercially purchased particles was 84.1%, 71.3% and 22.7%, respectively. The highest loading efficiency of biotemplated ceramics can be attributed to their higher specific surface area, which could provide more sites for drug anchoring. The BET surface area of the 45S5 Bioglass is usually lower than 10 $m^2 \cdot g^{-1}$ [403, 404], and this can explain its lower drug loading ability.

Pollen-derived microspheres exhibited a sustained release behaviour, with a low initial burst release compared with non-templated particles and commercially purchased samples. In the case of sol-gel produced microspheres, the complete release of the drug was achieved within 120h for the non-templated sample and 168h for the templated-one. In case of 45S5 Bioglass, the complete release was reached after only 90h. For both sol-gel synthesized particles, the release pattern happened through two different stages: the first was fast and represented the release of externally adsorbed drug molecules, while the second was slower (after 18h) and related to the release of the entrapped TCH in nano pores.

All these enhanced results for the sol-gel derived NPs can be explained as the wet sol-gel synthesis process offered the formation of more Si-OH groups on the microspheres compared to the 45S5 Bioglass samples. This fact results in the presence of a higher number of superficial $Si\text{-}O^-$ groups when particles were immersed in water, thus giving rise to a greater negative charge and an improved interaction with the positively charged TCH molecules. [401] The larger surface area of the pollen-derived ceramic, moreover, led to the presence of the highest number of silanol groups with respect to the other samples, therefore, producing the highest electrostatic interaction between TCH and the carrier, and the longest release time.

Antimicrobial tests and cytotoxicity tests performed with the pollen-templated Ca/SiO_2 microspheres demonstrated that only when the samples were loaded with TCH molecules did they exhibit bactericidal action against an *E. Coli* strain. When, instead, pristine particles were placed to interact with the bacteria or with Hep G2 cells they did not produce any antimicrobial or cytotoxic action. Finally, an in vitro mineralization test showed the enhanced ability of the biomorphic Ca/SiO_2 microspheres to form hydroxyapatite crystals when immersed in a simulated body fluid (Figure 47b), compared to the non-templated sample. The results of this study show how the hierarchic porous Ca/SiO_2 ecoceramics could be used as promising materials for bone regeneration and for local drug delivery.

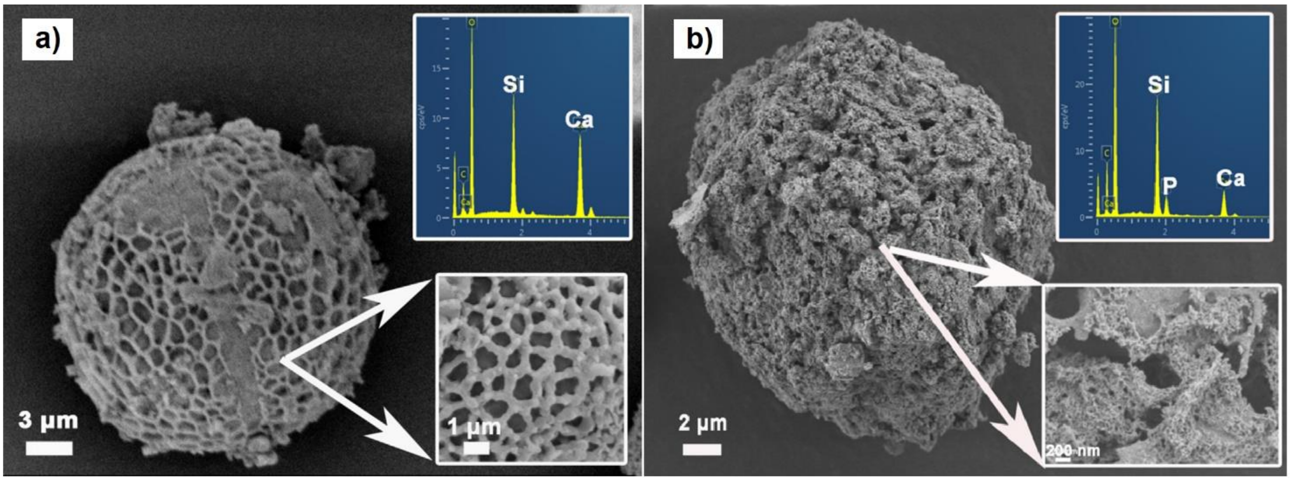

Figure 47 *– SEM images and EDS results of pollen-templated Ca/SiO_2 microsphere a) before and b) after immersion in simulated body fluid for 3 days [401]*

Pure SiO_2 usually does not display catalytic behaviour, but thanks to its chemically inert nature, can represent an optimal scaffold for the incorporation of more active elements. In Li et al.'s study, [402] the incorporation of cobalt into a leaf-templated SiO_2 ceramic led to the formation of a catalytically active material for the allylic oxidation of limonene to carvone. Carvone is an aromatic compound that find wide applications as a food additive, antimicrobial agent, biological building block and biochemical environmental indicator. [405] The classical methods for the synthesis of carvone from limonene are often performed in environmentally unfriendly solvents, producing toxic by-products and with the involvement of complex separation processes. [406] Finding valuable new "green" procedures for the production of carvone from limonene is, hence, a challenge from both an economic and environmental point of view.

In Li et al.'s work [402] the Co-doped silica retained the hierarchical porous structure of the reed leaf template after the typical substitution treatment, showing honeycomb-like pores and vessels with sizes ranging from 10 to 20 µm. The produced ecoceramic possessed a very large surface area of 435 $m^2 \cdot g^{-1}$, a pore volume of 0.52 $cm^3 \cdot g^{-1}$ and an average pore diameter of 4.6 nm. XRD analysis of the sample revealed that the structure of silica was essentially amorphous without any distinct diffraction peaks corresponding to crystalline cobalt. This fact demonstrated that the Co species were well incorporated into the SiO_2 framework, and their presence was confirmed through XPS.

Catalytic allylic oxidation tests showed that leaf-templated Co/SiO_2 ceramic possessed improved performance for the conversion of limonene to carvone compared to other silica-based catalysts (Table 13). The best results for the biomorphic Co/SiO_2 samples were obtained when the Si/Co molar ratio was 60/1, catalyst amount 100 mg, acetic anhydride was used as a solvent, air as the oxidant agent, and with reaction time and temperature respectively of 18h and 75 °C, resulting in a total conversion of limonene and a selectivity toward carvone of 40.2%. Among the other materials tested under the same conditions, leaf-templated pure SiO_2 and MCM-41 (Mobil Composition of Matter No. 41) displayed much lower conversion and selectivity, confirming the need for the presence of cobalt for greater catalytic activity. In the case of Co/MCM-41, Co/SBA-15 (Santa Barbara Amorphous-15) and Co/SBA-3, although presenting similar concentrations of cobalt and a much larger specific surface area, they exhibited lower oxidation activity. This fact could be attributed to the larger diameter and the hierarchic structure of the pores in the biotemplated Co/SiO_2 samples, which could prevent the steric hindrance during catalytic transformation of limonene to products. At the same time, complex porous network could help guest species to overcome the intra-diffusional resistance and allow a rapid diffusion of bulky products through the inorganic networks, ensuring high selectivity of catalytically active sites and avoiding over-oxidation processes. [402] Eventually, recycling experiments proved the stability of the leaf-templated Co/SiO_2 ceramic, still showing 90% of conversion of limonene with a selectivity of carvone around 43% after 3 cycles, without displaying significant variation in the state of the Co active sites.

Table 13 - Comparison of catalytic activities of different catalysts for the oxidation of limonene

Catalyst	BET surface area ($m^2 \cdot g^{-1}$)	Average pore diameter (nm)	Conversion of limonene (%)	Selectivity of carvone (%)
Leaf-templated Co/SiO_2	435	4.6	100	40.2
Leaf-templated SiO_2	/	/	35.7	22.5
MCM-41	/	/	16.7	12.8
Co/MCM-41	945	2.9	47.5	34.6
Co/SBA-15	690	3.2	50.2	21.7
Co/SBA-3	780	4.5	65.1	18.5

Contrary to the great deal of research carried out on silicon carbide, there have been few studies which focus their attention to the conversion of lignocellulosic materials into silicon dioxide, especially for woody and fibrous materials. Moreover, up to now no works have focused their attention on other oxides of metalloid elements, for example GeO_2. Continuing research in this direction could prove the opportunity to produce new materials with more attractive properties while, at the same time, lowering production costs and recycling waste lignocellulosic compounds.

5. Conclusions

Hierarchically porous oxide ceramics derived from lignocellulosic templates have been reviewed in this thesis. This class of materials possesses unique properties that are reflected in a wide range of applications. Thanks to their low density, low weight, low thermal conductivity, high surface area, high gas permeability, and high temperature and chemical stability, porous oxide ceramics have been investigated as optimal photocatalysts, sensors, absorbers, catalyst supports, biomedical implants and many other technologically advanced applications.

The production of such promising materials follows the general process of substitution of the lignocellulosic biomass by the oxide ceramic. This method involves the infiltration of the original template, or a carbonized form of it, with a precursor solution and a successive oxidative reaction at high temperature which gives rise to the final product. Among the various lignocellulosic materials used as templates to prepare porous ceramics, the most researched are woods, fibers, pollens and leaves. All these natural products can be easily collected and, since many of them are industrial waste materials or by-products, they also have a low market cost, making the entire process more economically affordable. Furthermore, the recycling of these compounds can reduce waste and energy production, giving at the same time the opportunity to obtain new materials with different characteristics that could not be achieved throughout other synthetic methods.

Nowadays, the most investigated biomorphic oxide ceramic is titanium dioxide. Biomorphous TiO_2 has been produced starting from a large variety of templates and showed promising results in photocatalytic applications such as photodegradation of pollutants and photocatalytic H_2 production. The excellent results are caused by the peculiar hierarchical structure of the pores derived from the various lignocellulosic templates tested. The graded porous network significantly enhanced light harvesting and light scattering, allowing increasing internal reflections and therefore improving the photocatalytic efficiency.

Unique architectural characteristics and outstanding performance were inherited also by CeO_2 and ZnO ceramics when they were templated from natural scaffolds. Applications such as thermochemical CO production and gas sensing presented better results when biomorphous oxides were employed compared to materials synthesized with common production methods. Indeed, a larger number of adsorbed oxygen species and structural oxygen vacancies were generated in biomorphic oxide ceramics, increasing the interactions between the target gases and the material. Moreover, macro pores minimized gaseous diffusion limitations while micro and meso pores increased the specific surface area of the materials, enhancing the overall internal mass transport and improving the active sites accessibility. The presence of all these features resulted in higher gas conversion or detection for the biotemplated materials.

Hierarchical porous structures not only helped percolation of gases but has also contributed to a better diffusion of liquids. In the case of biomorphic transition metal oxides applied in electrochemical applications, the porous skeleton offered an appropriate space for the electrolyte diffusion during the electrochemical processes and, at the same time, reduced the effective path for electron conduction. In addition, the high values of specific surface area possessed by the ceramics provided more active sites where electrochemical reactions could occur. TMOs derived from lignocellulosic biomass showed consequently better performance with respect to the commercially available active carbon electrodes when employed as electrodes in pseudocapacitors and lithium-ion batteries.

Other interesting applications in which biotemplated TMOs presented promising results were direct catalytic pollutant degradation and as support materials for catalysts. In the first case, the porous architecture and large surface area allowed an improved interaction between the catalyst and the contaminants leading to enhanced removal performances, while in the second case the unique structure and the particular nature of the oxide helped to obtain an optimal catalyst scaffold with magnetic properties excellent for its recycling.

Post-transition metal oxides such as alumina have also been prepared from lignocellulosic biomass and employed for removal of contaminants. Al_2O_3 ecoceramic has shown good absorption results but still required chemical modification to assert the best performance, demonstrating the typically inert nature of pure Al_2O_3. Many studies have been carried out on the conversion of wood and fibers into alumina ceramics, but few practical applications have been investigated. The low reactivity and high chemical stability could be thus exploited to produce materials to be employed in the biomedical field or as supports for more active catalysts.

Unlike alumina, a lower number of studies have been performed for the production of biotemplated post-transition metal oxide ceramics such as In_2O_3 and SnO_2. However, for both materials more advanced applications have been tested. When applied as sensors, very high sensitivity toward Cl_2 detection was achieved by cotton-templated In_2O_3 ceramic while optimal results were obtained by pollen-derived SnO_2 microspheres during exposition to NO_2 gas. The precise reproduction of the various templates allowed the formation of highly porous ceramics with a large number of oxygen vacancies and active sites suitable for the detection of the vapours.

In addition to sensing applications, biomorphic SnO_2 hollow microtubes showed promising efficiency in energetic production when incorporated in an electrode of a dye-sensitized solar cell. The presence of tin dioxide fibers in the titania-based electrode increased the physical separation between injected electrons and oxidized dyes/redox couples, offering furthermore a larger specific surface area. These characteristics successfully retarded the recombination reactions in TiO_2-NP photoelectrode and improved the absorption capacity for the dye, the infiltration of the electrolyte and the charge transfer.

Biomorphous ceramics were produced also from alkaline earth metals like calcium and magnesium. Researchers focused their attention mainly on the conversion of fibers into CaO ang MgO ceramics rather than other lignocellulosic templates. For both materials, interesting applications were tested, such as CO_2 capture and bacterial removal, and encouraging results were obtained. Especially in the case of the calcium looping process, cotton-derived CaO doped with aluminium demonstrated an improved efficiency and lower costs compared to the use of pure limestone.

Wood samples were mostly used for the creation of hydroxyapatite ceramics. This fact was driven by the similar architecture that wood possess with respect to bones. Wood-templated HA ceramics could, therefore, be optimal materials for medical implants, as the cited preliminary studies have revealed.

Contrary to silicon carbide, very little research has been performed for the production of biomorphic silica ceramics, and even less in which practical applications were tested. Thanks to the biocompatible nature and large surface area, however, biotemplated SiO_2 has shown the possibility to be used both as a promising drug delivery device and as an optimal and recyclable catalyst, when combined with other more active elements. Among metalloids, only silicon oxide has been investigated as a possible biomorphic ceramic, but other elements, like boron and germanium, could also give rise to such promising materials.

The global environmental crisis and the need for technologically advanced materials have led researchers to focus their attention on the production hierarchically porous ceramics exploiting wastes and natural resources. An interesting example of promising templating wood biomass that could be employed more is cork, a wood material primarily harvested from cork oak. Cork wood possess a unique 3-DOM structure composed of numerous hexagonal honeycomb cells which make it an optimal thermal, acoustic and vibrational insulator. Moreover, cork is a fully sustainable material since the bark from which it derives is periodically harvested without harming the tree, making cork one of the best examples of a carbon storage plant. These types of materials could satisfy both sustainable and high-tech requests, but further investigations are still required. Nowadays, the vast majority of hierarchically porous ecoceramics are in powder form, and this does not allow them to be used in many practical applications. Future studies should be focused on an improvement of the production techniques which could lead to the production of monolithic samples or continuous films, even on a large scale.

6. References

[1] P. S. Liu, G. F. Chen, Porous Materials: Processing and Applications, Elsevier, **2014**

[2] C. Vakifahmetoglu, D. Zeydanli, P. Colombo, *Mater. Sci. Eng. R,* **2016**, 106, 1

[3] M.-H. Sun, S.-Z. Huang, L.-H. Chen, Y. Li, X.-Y. Yang, Z.-Y. Yuan, B.-L. Su, *Chem. Soc. Rev.*, **2016**, 45, 3479

[4] G. Zan, Q. Wu, *Adv. Mater.*, **2016**, 28, 2099

[5] I. Burgert, E. Cabane, C. Zollfrank, L. Berglund, *Int. Mater. Rev.*, **2015**, 60:8, 431

[6] A. Muthutantri, J. Huang, M. Edirisinghe, *J. R. Soc. Interface,* **2008**, 5, 1459

[7] A. J. Panshin, C. deZeeuw, Textbook of Wood Technology, McGraw-Hill, **1980**

[8] M. Singh, J. Martínez-Fernández, A. R. de Arellano-López, *Curr. Opin. Solid State Mater. Sci.*, **2003**, 7, 247

[9] L. Esposito, D. Sciti, A. Piancastelli, A. Bellosi, *J. Eur. Ceram. Soc.*, **2004**, 24, 533

[10] E. Vogli, H. Sieber, P. Greil, *J. Eur. Ceram. Soc.*, **2002**, 22, 2663

[11] Q. Wang, D. Wang, G. Jin, Y. Wang, X. Guo, *Particuology*, **2009**, 7, 199

[12] M. Singh, B.-M. Yee, *J. Eur. Ceram. Soc.*, **2004**, 24, 209

[13] H. Sieber, *Mater. Sci. Eng. A*, **2005**, 412, 43

[14] P. Greil, *J. Eur. Ceram. Soc.*, **2001**, 21, 105

[15] P. Greil, T. Lifka, A. Kaindl, *J. Eur. Ceram. Soc.*, **1998**, 18, 1961

[16] A.R. de Arellano-López, J. Martínez-Fernández, P. González, C. Domínguez, V. Fernández-Quero, M. Singh, *Int. J. Appl. Ceram. Technol.*, **2004**, 1, 56

[17] J. Ramirez-Rico, J. Martínez-Fernandez, M. Singh, *Int. Mater. Rev.*, **2017**, 62, 465

[18] H. Elias, K. M. Hyie, A. Kalam, N. A. Rahman, *AIP Conf. Proc.*, **2016**, 1774, 060004

[19] L. S. Parfen'eva, T. S. Orlova, B. I. Smirnov, I. A. Smirnov, H. Misiorek, J. Mucha, A. Jezowski, A. Gutierrez-Pardo, J. Ramirez-Rico, *Phys. Solid State*, **2012**, 54, 2132

[20] A. I. Shelykh, B. I. Smirnov, I. A. Smirnov, A. R. de Arellano-Lopez, J. Martinez-Fernandez, F. M. Varela-Feria, *Phys. Solid State*, **2006**, 48, 216

[21] L. S. Parfen'eva, T. S. Orlova, N. F. Kartenko, N. V. Sharenkova, B. I. Smirnov, I. A. Smirnov, H. Misiorek, A. Jezowski, F. M. Varela-Feria, J. Martinez-Fernandez, A. R. de Arellano-Lopez, *Phys. Solid State*, **2005**, 47, 1216

[22] C.R. Rambo, J. Cao, O. Rusina, H. Sieber, *Carbon,* **2005**, 43, 1174

[23] T. Srichumpong, J. Wannasin, S. Niyomwas, *J. Met. Mater. Miner.*, **2008**, 18, 117

[24] T. Ashitani, R. Tomoshige, M. Oyadomari, T. Ueno, K. Sakai, *J. Ceram. Soc. JAPAN,* **2002**, 110, 632

[25] H. Wu, T. Zhang, Y. Li, *Ceram. Int.,* **2015**, 41, 13034

[26] C. E. Wyman, *Biotechnol. Prog.*, **2003**, 19, 254

[27] N. Sipahutar, R. Sipahutar, *Energ. Source Part A*, **2015**, 37, 2710

[28] H. Zhou, T.-X. Fan, D. Zhang, *ChemSusChem*, **2011**, 4, 1344

[29] T.-X. Fan, S.-K. Chow, D. Zhang, *Prog. Mater. Sci.*, **2009**, 54, 542

[30] N. E. Kochkina, A. V. Agafonov, A. V. Vinogradov, N. S. Karasev, N. L. Ovchinnikov, M. F. Butman, *ACS Sustain. Chem. Eng.*, **2017**, 5, 5148

[31] J. F. V. Vincent, Structural Biomaterials, Palgrave Macmillan, **1982**

[32] H. Lange, S. Decina, C. Crestini, *Eur. Polym. J.*, **2013**, 49, 1151

[33] L. T. Mika, E. Cséfalvay, Á. Németh, *Chem. Rev.*, **2018**, 118, 505

[34] J. Cao, Biotemplating of highly porous oxide ceramics, Cuvillier Verlag, **2005**

[35] M. B. Sticklen, *Nat. Rev. Genet.*, **2010**, 11, 308

[36] S. L. Mathews, J. Pawlak, A. M. Grunden, *Appl. Microbiol. Biotechnol.,* **2015**, 99, 2939

[37] J. E. G. van Dam, T. A. Gorshkova, Encyclopedia of Applied Plant Sciences, Elsevier, **2003**

[38] J. Rytioja, K. Hildén, J. Yuzon, A. Hatakka, R. P. de Vries, M. R. Mäkelä, *Microbiol. Mol. Biol. Rev.*, **2014**, 78, 614

[39] M. Borrega, P. Ahvenainen, R. Serimaa, L. Gibson, *Wood Sci. Technol.*, **2015**, 49, 403

[40] J. Cao, C. R. Rambo, H. Sieber, *J. Porous Mater.,* **2004**, 11, 163

[41] https://www.barbequescience.com/wood-types/ - last check May 2020

[42] C. D. Malonzo, R. M. De Smith, S. G. Rudisill, N. D. Petkovich, J. H. Davidson, A. Stein, *J. Phys. Chem. C,* **2014**, 118, 26172

[43] P. J. M. Carrott, M. M. L. Ribeiro Carrott, P. A. M. Mourao, *J. Anal. Appl. Pyrolysis,* **2006**, 75, 120

[44] A. M. A. Pintor, C. I. A. Ferreira, J. C. Pereira, P. Correia, S. P. Silva, V. J. P. Vilar, C. M. S. Botelho, R. A. R. Boaventura, *Water Res.*, **2012**, 46, 3152

[45] H. Pereira, Cork: Biology, Production and Uses, Elsevier, **2007**

[46] S. P. Silva, M. A. Sabino, E. M. Fernandes, V. M. Correlo, L. F. Boesel, R. L. Reis, *Int. Mater. Rev.*, **2005**, 50, 345

[47] L. Gil, *Front. Chem.*, **2014**, 2, 16

[48] R. M. Novais, M. Saeli, A. P. F. Caetano, M. P. Seabra, J. A. Labrincha, K. P. Surendran, R. C. Pullar, *Constr Build Mater.*, **2019**, 229, 116930

[49] R. M. Novais, A. P. F. Caetano, M. P. Seabra, J. A. Labrincha, R. C. Pullar, *J. Clean. Prod.*, **2018**, 197, 1137

[50] R. M. Novais, R. C. Pullar, *J. Eur. Ceram. Soc.*, **2019**, 39, 1287

[51] M. Dochia, C. Sirghie, R. M. Kozlowski, Z. Roskwitalski, Handbook of Natural Fibres, Elsevier, **2012**

[52] Z.-S. Guan, Y. Zhang, C.-H. Lu, Z.-Z. Xu, *Chin. J. Chem.*, **2008**, 26, 467

[53] G. Pasqua, G. Abbate, F. Forni, Botanica Generale e Biodiversità Vegetale, Piccin Editore, **2015**, 239

[54] H. Zhou, X. Li, T. Fan, F. E. Osterloh, J. Ding, E. M. Sabio, D. Zhang, Q. Guo, *Adv. Mater.*, **2010**, 22, 951

[55] V. Menon, M. Rao, *Prog. Energy Combust. Sci.*, **2012**, 38, 522

[56] D. Russo, M. Dassisti, V. Lawlor, A. G. Olabi, *Renew. Sustain. Energ. Rev.*, **2012**, 16, 4056

[57] R. Hatti-Kau, U. Törnvall, L. Gustafsson, P. Börjesson, *Trends Biotechnol.*, **2007**, 25, 119.

[58] D. J. Pollard, J. M. Woodley, *Trends Biotechnol*., **2007**, 25, 66

[59] O. J. Sanchez, C. A. Cardona, *Bioresour. Technol*., **2008**, 99, 5270

[60] H. B. Goyal, D. Seal, R. C. Saxena, *Renew. Sustain. Energ. Rev*., **2008**, 12, 504

[61] P. Mc Kendry, *Bioresour. Technol*., **2002**, 83, 55

[62] C.-Q. Dong, Z.-F. Zhang, Q. Lu, Y.-P. Yang, *Energy Convers. Manag.*, **2012**, 57, 49

[63] C. E. Byrne, D. C. Nagle, *Carbon*, **1997**, 35, 259

[64] P. Greil, *Mater. Chem. Phys*., **1999**, 61, 64

[65] T. X. Fan, T. Hirose, T. Okabe, D. Zhang, *J. Porous Mater.*, **2001**, 8, 211

[66] T. Okabe, K. Saito, K. Hokkirigawa, *J. Porous Mater.*, **1996**, 2, 207

[67] J. Qian, J. Wang, Z. Jin, *Mater. Sci. Eng. A*, **2004**, 371, 229

[68] J.-M. Qian, J.-P. Wang, G.-J. Qiao, Z.-H. Jin, *J. Eur. Ceram. Soc.*, **2004**, 24, 3251

[69] F. M. Varela-Feria, J. Ramirez-Rico, J. Martínez Fernández, A. R. de Arellano Lopez, M. Singh, *Ceram. Trans.*, **2006**, 177, 93

[70] E. Vogli, J. Mukerji, C. Hoffmann, R. Kladny, H. Sieber, P. Greil, *J. Am. Ceram. Soc*., **2001**, 84, 1236

[71] P. Gonzalez, J. Serra, S. Liste, S. Chiussi, B. Leon, M. Perez-Amor, J. Martınez-Fernandez, A.R. de Arellano-Lopez, F.M. Varela-Feria, *Biomaterials*, **2003**, 24, 4827

[72] B. Sun, T. Fan, D. Zhang, T. Okabe, *Carbon*, **2004**, 42, 177

[73] N. Popovska, D. A. Streitwieser, C. Xu, H. Gerhard, *J. Eur. Ceram. Soc*., **2005**, 25, 829.

[74] M. Parashar, V. K. Shukla, R. Singh, *J. Mater. Sci. Mater. Electron.*, **2020**, 31, 3729

[75] S. Mahajan, Encyclopedia of Materials: Science and Technology, Elsevier, **2001**

[76] S. P. Gaikwad, S. R. Dhage, H. S. Potdar, V. Samuel, V. Ravi, *J. Electroceramics*, **2005**, 14, 83

[77] Y. Wang, Z. Liu, B. Han, Z. Sun, J. Du, J. Zhang, T. Jiang, W. Wu, Z. Miao, *Chem. Commun*., **2005**, 2948

[78] L. L. Hench, J. K. West, *Chem. Rev*., **1990**, 90, 33

[79] N. Hüsing, U. Schubert, *Angew. Chem. Int. Ed.*, **1998**, 37, 22

[80] Y. Zhang, Y. Ding, J. Gao, J. Yang, *J. Eur. Ceram. Soc*., **2009**, 29, 1101

[81] J. F. Chen, Y. H. Wang, F. Guo, X. M. Wang, C. Zheng, *Ind. Eng. Chem. Res*., **2000**, 39, 948

[82] M. Zhou, J. Yu, S. Liu, P. Zhai, B. Huang, *Appl. Catal. B*, **2009**, 89, 160

[83] A. Imhof, D. J. Pine, *Adv. Mater*., **1998**, 10, 697

[84] C. J. Brinker, G. W. Scherer, Sol-Gel Science: The Physics and Chemistry of Sol-Gel Processing, Academic Press, **1990**

[85] M. Sharma, M. Pathak, P. N. Kapoor, *Asian J. Chem*, **2018**, 30, 1405

[86] J. Livage, M. Henry, C. Sanchez, *Prog. Solid. State Ch.*, **1988**, 18, 259

[87] A. E. Danks, S. R. Hall, Z. Schnepp, *Mater. Horizons*, **2016**, 3, 91

[88] S. Valencia, J. M. Marín, G. Restrepo, *Open Mater. Sci. J.*, **2010**, 4, 9

[89] H. F. Yu, S. M. Wang, *J Non Cryst Solids*, **2000**, 261, 260

[90] X. Chen, S. S. Mao, *Chem. Rev.*, **2007**, 107, 2891

[91] M. A. Fox, M. T. Dulay, *Chem. Rev.*, **1993**, 93, 341

[92] M. R. Hoffmann, S. T. Martin, W. Choi, *Chem. Rev.*, **1995**, 95, 69

[93] Y. Lee, K. Misook, *Mater. Chem. Phys.*, **2010**, 122, 284

[94] A. Fujishima, K. Honda, *Nature*, **1972**, 238, 37

[95] A. Gabor, A. Somorjai, M. Contreras, M. Montano, R. M. Rioux, *Proc. Natl. Acad. Sci. U.S.A.*, **2006**, 103, 10577

[96] A. Mills, S. L. Hunte, *J. Photochem. Photobiol. A*, **1997**, 108, 1

[97] C. Burda, X. Chen, R. Narayanan, Mostafa A. El-Sayed, *Chem. Rev.*, **2005**, 105, 1025

[98] Y. Zhang, Z. Jiang, J. Huang, L. Y. Lim, W. Li, J. Deng, D. Gong, Y. Tang, Y. Lai, Z. Chen, *RSC Adv*., **2015**, 5, 79479

[99] H. Zhang, J. F. Banfield, *J. Phys. Chem. B*., **2000**, 104, 3481

[100] R. D. Shannon, J. A. Pask, *J. Am. Ceram. Soc*., **1965**, 48, 391

[101] J. F. Banfield, B. L. Bischoff, M. A. Anderson, *Chem. Geol*., **1993**, 110, 211

[102] R. A. Eppler, *J. Am. Ceram. Soc*., **1987**, 70, 4

[103] Y. Iida, S. Ozaki, *J. Am. Ceram. Soc*., **1961**, 44, 120

[104] Y. H. Zhang, A. Reller, *Mater. Sci. Eng. C*, **2002**, 19, 323

[105] K. Okada, N. Yamamoto, Y. Kameshima, A. Yasumori, K. J. D. MacKenzie, *J. Am. Ceram. Soc*., **2001**, 84, 1591

[106] S. Vargas, R. Arroyo, E. Haro, R. Rodriguez, *J. Mater. Res.*, **1999**, 14, 3932

[107] R. Rodriguez-Talavera, S. Vargas, R. Arroyo-Murillo, R. Montiel-Campos, E. Haro-Poniatowski, *J. Mater. Res.*, **1997**, 12, 439

[108] W. Wunderlich, T. Oekermann, L. Miao, N. T. Hued, S. Tanemurac, M. Tanemura, *J. Ceram. Process. Res.*, **2004**, 5, 343

[109] A. Fujishima, T. N. Rao, D. A. Tryk, *J. Photochem. Photobiol. C*, **2000**, 1, 1

[110] Y. Hendrix, A. Lazaro, Q. Yu, J. Bouwers, *WJNSE*, **2015**, 5, 161

[111] J. L. Vivero-Escoto, Y.-D. Chiang, K. C.-W. Wu, Y. Yamauchi, *Sci Technol Adv Mater*, **2012**, 13, 013003

[112] T. Luttrell, S. Halpegamage, J. Tao, A. Kramer, E. Sutter, M. Batzill, *Sci. Rep.*, **2014**, 4, 4043

[113] G. Mattioli, F. Filippone, P. Alippi, A. A. Bonapasta, *Phys. Rev. B*, **2008**, 78, 241201

[114] M. Xu, Y. Gao, E. M. Moreno, M. Kunst, M. Muhler, Y. Wang, H. Idriss, C. Wöll, *Phys. Rev. Lett.*, **2011**, 106, 138302

[115] B. Ohtani, Y. Ogawa, S. I. Nishimoto, *J. Phys. Chem. B*, **1997**, 101, 3746

[116] R. I. Bickley, T. Gonzalez-Carreno, J. S. Lees, L. Palmisano, R. J. Tilley, *J Solid State Chem*, **1991**, 92, 178

[117] D. O. Scanlon, C. W. Dunnill, J. Buckeridge, S. A. Shevlin, A. J. Logsdail, S. M. Woodley, A. A. Sokol, *Nat. Mater.*, **2013**, 12, 798

[118] J. Cao, C.R. Rambo, H. Sieber, *Ceram. Int.*, **2004**, 30, 1967

[119] J. Cao, O. Rusina, H. Sieber, *Ceram. Int.*, **2004**, 30, 1971

[120] M. M. López Guerrero, E. Vereda Alonson, A. Garcíade Torres, M. López Claros, J. M. Cano Pavón, *Ceram. Int.*, **2013**, 39, 7861

[121] T. Ota, M. Imaeda, H. Takase, M. Kobayashi, N. Kinoshita, T. Hirashita, H. Miyazaki, Y. Hikichi, *J. Am. Ceram. Soc.*, **2000**, 83, 1521

[122] L. Qian, R. Li, L. Zhou, Y. Liu, M. Yu, F. Xiong, S. Liu, X. Hao, *Bioresources*, **2015**, 10, 4391

[123] Q. Sun, Y. Lu, J. Tu, D. Yang, J. Cao, J. Li, *Int. J. Photoenergy*, **2013**, 2013, 649540

[124] S. Zhu, D. Zhang, Z. Chen, G. Zhou, H. Jiang, J. Li, *J Nanopart Res*, **2010**, 12, 2445

[125] L. Gao, W. Gan, Z. Qiu, X. Zhan, T. Qiang, J. Li, *Sci. Rep.*, **2017**, 7, 1102

[126] H. Zhou, J. Pan, L. Ding, Y. Tang, J. Ding, Q. Guo, T. Fan, D. Zhang*, Int. J. Hydrog. Energy*, **2014**, 39, 16293

[127] Y. Lu, Q. Sun, T. Liu, D. Yang, Y. Liu, J. Li, *J. Alloys Compd.*, **2013**, 577, 569

[128] M. Patel, B. K. Padhi, *J Mater Sci Lett*, **1993**, 12, 1234

[129] S. Yao, Y. Zhang, Z. Shi, S. Wang, *Russ. J. Phys. Chem. A*, **2013**, 87, 69

[130] J. Qiu, X. Sun, J. Xing, X. Liu, *Russ. J. Phys. Chem. A*, **2014**, 88, 1236

[131] L. Dou, L. Gao, X. Yang, X. Song, *J. Hazard. Mater.*, **2012**, 203, 363

[132] D. A. Erdogan, E. Ozensoy, *Appl. Surf. Sci.*, **2017**, 403, 159

[133] S. R. Hall, V. M. Swinerd, F. N. Newby, A. M. Collins, S. Mann, *Chem. Mater*., **2006**, 18, 598

[134] H. Zuoli, W. Que, Y. He, *Mater. Lett.*, **2013**, 94, 136

[135] Y. Zheng, C. Luo, L. Liu, Z. Yang, S. Ren, Y. Cai, J. Xiong, *Mater. Lett.*, **2016**, 181, 169

[136] D. Bu, H. Zhuang, *Catal Commun*, **2012**, 29, 24

[137] R. Bao, R. Li, C. Chen, H. Wu, J. Xia, C. Long, H. Li, *J Phys Chem Solids*, **2019**, 126, 78

[138] M. Mizutani, H. Takase, N. Adachi, T. Ota, K. Daimon, Y. Hikichi, Sci Technol Adv Mater, **2005**, 6, 76

[139] X. Li, T. Fan, H. Zhou, S.-K. Chow, W. Zhang, D. Zhang, Q. Guo, H. Ogawa, *Adv. Funct. Mater.,* **2009**, 19, 45

[140] A. Chen, J. Qian, Y. Chenc, X. Lu, F. Wang, Z. Tang, *Powder Technol.*, **2013**, 249, 71

[141] B. Li, J. Zhao, J. Liu, X. Shen, S. Mo, H. Tong, *RSC Adv.*, **2015**, 5, 15572

[142] Q. Xu, J. Tang, Y. Shen, L. Jin, X. Hu, *Talanta*, **2015**, 144, 6

[143] O. Anjaneya, S. S. Shrishailnath, K. Guruprasad, A. S. Nayak, S. B. Mashetty, T. B. Karegoudar, *Int. Biodeterior. Biodegradation*, **2013**, 79, 64

[144] S. Pattra, S. Sangyoka, M. Boonmee, A. Reungsang, *Int. J. Hydrog. Energy,* **2008**, 33, 5256

[145] M. Murdoch, G. I. N. Waterhouse, M. A. Nadeem, J. B. Metson, M. A. Keane, R. F. Howe, J. Llorca, H. Idriss, *Nat. Chem.*, **2011**, 3, 489

[146] K. Domen, A. Kudo, M. Shibata, A. Tanaka, K. Maruya, T. Onishi, *J. Chem. Soc, Chem. Commun*., **1986**, 23, 1706

[147] J. Pawley, Handbook of Biological Confocal Microscopy, Springer Science & Business Media, **2010**

[148] H. Zhu, B. Yang, J. Xu, Z. Fu, M. Wen, T. Guo, S. Fu, J. Zuo, S. Zhang, *Appl. Catal. B*, **2009**, 90, 463

[149] J. D. Zhang, Q. J. Chi, S. J. Dong, E. K. Wang, *Bioelectrochem Bioenerg.*, **1996**, 39, 267

[150] X. Q. Liu, H. Q. Feng, J. M. Zhang, R. X. Zhao, X. H. Liu, D. K. Y. Wong, *Biosens. Bioelectron.*, **2012**, 32, 188

[151] F. H. Wu, J. J. Xu, Y. Tian, Z. C. Hu, L. W. Wang, Y. Z. Xian, L. T. Jin, *Biosens. Bioelectron.*, **2008**, 24, 198

[152] M. Viticoli, A. Curulli, A. Cusma, S. Kaciulis, S. Nunziante, L. Pandolfi, F. Valentini, G. Padeletti, Mater. Sci. Eng. C., **2006**, 26, 947

[153] L. Zhang, Q. Zhang, X. Lu, J. Li, *Biosens. Bioelectron*., **2007**, 23, 102

[154] Q. Xie, Y. Y. Zhao, X. Chen, H. M. Liu, D. G. Evans, W. S. Yang, *Biomaterials*, 2011, 32, 6588

[155] Y. Li, J. Li, X. H. Xia, S. Q. Liu, *Talanta*, 2010, 82, 1164

[155] F. Rollin-Genetet, C. Seidel, E. Artells, M. Auffan, A. Thiéry, C. Vidaud, *Chem. Res. Toxicol.*, **2015**, 28, 2304

[156] H. Huang, J. Liu, P. Sun, S. Ye, B. Liu, *RSC Adv.,* **2017**, 7, 7406

[157] J. Qian, W. Zhang, Y. Wang, Z. Chen, F. Chen, C. Liu, X. Lu, P. Li, K. Wanga, A. Chen, *Appl. Surf. Sci.,* **2018**, 444, 118

[158] A. Trovarelli, C. de Leitenburg, M. Boaro, G. Dolcetti, *Catal. Today*, **1999**, 50, 353

[159] P. Jasinski, T. Suzuki, H. Anderson, *Sens. Actuators B Chem.*, **2003**, 95, 73

[160] R. Chockalingam, V. R. W. Amarakoon, H. Giesche, *J. Eur. Ceram. Soc*., **2008**, 28, 959

[161] X. Liu, K. Zhou, L. Wang, B. Wang, Y. Li, *J. Am. Chem. Soc.*, **2009**, 131, 3140

[162] E. Aneggi, M. Boaro, C. de Leitenburg, G. Dolcetti, A. Trovarelli, *J. Alloys Compd.*, **2006**, 408, 1096

[163] S. Chow, T. Fan, J. Ding, D. Zhang, *J. Am. Ceram. Soc*., **2010**, 93, 40

[164] R. C. Pullar, L. Gil, F. A. C. Oliveira, *Ciência & Tecnologia dos Materiais,* **2016**, 28, 23

[165] F. A. C. Oliveira, M. A. Barreiros, S. Abanades, A. P. F. Caetano, R. M. Novais, R. C. Pullar, *J. CO2 Util.,* **2018**, 26, 552

[166] B. Matovic, D. Nikolic, N. Labus, S. Ilic, V. Maksimovic, J. Lukovic, D. Bucevac, *Ceram. Int.*, **2013**, 39, 9645

[167] A. S. Deshpande, I. Burgert, O. Paris, *Small,* **2006**, 2, 994

[168] I. Y. Kaplin, E. S. Lokteva, E. V. Golubina, K. I. Maslakov, N. E. Strokova, S. A. Chernyak, V. V. Lunin, *RSC Adv.,* **2017**, 7, 51359

[169] J.-J. Huang, C.-C. Wang, L.-T. Jin, F. Cheng, Z.-G. Chen, *Trans. Nonferrous Met. Soc. China*, **2017**, 27, 578

[170] M. A. Stegmayer, V. G. Milt, E. E. Miró, *Catal Commun*, **2020**, 139, 105984

[171] Y. Liu, J. Yang, B. Wu, W. Zhang, X. Zhang, C. Shan, Q. Liu, *Colloids Surf. A Physicochem. Eng. Asp.*, **2020**, 586, 124193

[172] J. Qian, Z. Chen, C. Liu, X. Lu, F. Wang, M. Wang, *Mater Sci Semicond Process*, **2014**, 25, 27

[173] C. Liu, H. Sun, J. Qian, Z. Chen, Y. Lv, F. Chen, X. Lu, Z. Wua, Adv Powder Technol, **2017**, 28 2741

[174] D. Zhu, D. Duan, Y. Han, J. He, Y. He, Y. Chen, W. Zhang, Z. Yan, J. Wang, F. Yuan, *Catalysts*, **2016**, 6, 135

[175] J. Qian, F. Chen, X. Zhao, Z. Chen, *J Nanopart Res*, **2011**, 13, 7149

[176] J. R. Scheffe, A. Steinfeld, *Energy Fuels*, **2012**, 26, 1928

[177] W. T. Gibbons, L. J. Venstrom, R. M. De Smith, J. H. Davidson, G. S. Jackson, *Phys. Chem. Chem. Phys..*, **2014**, 16, 14271

[178] T. Tzamkiozis, L. Ntziachristos, Z. Samaras, *Atmos. Environ*., **2010**, 44, 909

[179] S. Bensaid, N. Russo, D. Fino, *Catal. Today*, **2013**, 216, 57

[180] H. Wang, S. Luo, M. Zhang, W. Liu, X. Wu, S. Liu, *J Catal*, **2018**, 368, 365

[181] Z. Chen, L. Chen, M. Jiang, X. Gao, M. Huang, Y. Li, L. Ren, Y. Yang, Z. Yang, *Appl. Surf. Sci.*, **2020**, 510, 145401

[182] K. Qi, B. Cheng, J. Yu, W. Ho, *J. Alloys Compd.*, **2017**, 727, 792

[183] V. S. Bhati, M. Hojamberdiev, M. Kumar, *Energy Rep.*, **2020**, 6, 46

[184] K. M. Lee, C. W. Lai, K. S. Ngai, J. C. Juan, *Water Res*., **2016**, 88, 428

[185] N. Tiwale, *Mater. Sci. Technol.*, **2015**, 31, 1681

[186] A. Kołodziejczak-Radzimska, T. Jesionowski, *Materials,* **2014**, 7, 2833

[187] Z. Liu, T. Fan, J. Ding, D. Zhang, Q. Guo, H. Ogawa, *Ceram. Int.*, **2008**, 34, 69

[188] Z. Liu, T. Fan, D. Zhang, X. Gong, J. Xu, *Sens. Actuators B Chem.*, **2009**, 136, 499

[189] A. Quarta, R. M. Novais, S. Bettini, M. Iafisco, R. C. Pullar, C. Piccirillo, *J. Environ. Chem. Eng., **2019**,* 7, 102936

[190] M. Zhou, D. Zang, X. Zhai, Z. Gao, W. Zhang, C. Wang, *Ceram. Int.*, **2016**, 42, 10704

[191] B. Abarna, T. Preethi, A. Karunanithi, G.R. Rajarajeswari, *Mater Sci Semicond Process,* **2016**, 56, 243

[192] B. T. Su, K. Wang, X. W. Zuo, H. M. Mu, N. Dong, Y. C. Tong, J. Bai, Z. Q. Lei, *Bull. Mater. Sci.*, **2007**, 30, 571

[193] B. Su, K. Wang, N. Dong, H. Mu, Z. Lei, Y. Tong, J. Bai, *J Mater Process Technol*, **2009**, 209, 4088

[194] A. Sivakumar, B. Murugesan, A. Loganathan, P. Sivakumar, *J Taiwan Inst Chem Eng,* **2017**, 78, 462

[195] H. Wang, H. Li, S. Li, L. Liu, L. Wang, X. Guo, *J. Mater. Sci. Mater. Electron.,* **2017**, 28, 958

[196] S. Yan, S. Ma, X. Xu, Y. Lu, H. Bian, X. Liang, W. Jin, H. Yang, *Mater. Lett.*, **2016**, 165, 9

[197] S. Zhu, Q. Chen, C. Yang, Y. Zhang, L. Hou, G. Pang, X. He, X. Zhang, C. Yuan, *Int. J. Hydrog. Energy*, **2017**, 42, 14154

[198] H. Hamrouni, I. Jaouali, M. F. Nsib, E. Fazio, F. Neri, A. Bonavita, S. G. Leonardi, G. Neri, *J. Mater. Sci. Mater. Electron.,* **2018,** 29, 11096

[199] Y. Liu, X. Zhang, B. Wu, H. Zhao, W. Zhang, C. Shan, J. Yang, Q. Liu, *ChemistrySelect,* **2019**, 4, 12445

[200] N. M. Black, D. S. Ciota, E. G. Gillan, *Inorganics*, **2018**, 6, 103

[201] A. Cai, A. Guo, L. Du, Y. Qi, X. Wang, *Mater. Res. Bull*., **2018**, 103, 225

[202] Q.-R. Zeng, J.-T. Feng, X.-C. Lin, Y. Zhao, H. Liu, S.-Z. Wang, Z.-J. Dong, W. Feng, *J. Alloys Compd.,* **2020***,* 815, 150550

[203] H. Zhou, T. Fan, X. Li, D. Zhang, Q. Guo, H. Ogawa, *J. Mater. Chem. A*, **2009**, 19, 2695–2703

[204] S. Sharma, M. Madou, *Philos. Trans. R. Soc. A Math. Phys. Eng. Sci.*, **2012**, 370, 2448

[205] J. Wang, R. Chen, L. Xiang, S. Komarneni, *Ceram. Int.*, **2018**, 44, 7357

[206] H. Ning, X. Wu, L. Chai, H. Liu, Y. Chen, *Sens. Actuators B Chem.,* **2010**, 150, 230

[207] R. C. Pullar, P. Marques, J. Amaral, J. A. Labrincha, *Mater. Des.,* **2015**, 82, 297

[208] D. V. Dao, M. van den Bremt, Z. Koeller, T. K. Le, *Powder Technol.,* **2016**, 288, 366

[209] J. D. L. Andrade, A. G. Oliveira, V. V. G. Mariucci, A. C. Bento, M. V. Companhoni, C. V. Nakamura, S. M. Lima, L. H. D. C. Andrade, J. C. G. Morares, A. A. W. Hechenleitner, E. A. G. Pineda, D. M. F. de Oliveira, *J. Alloys Compd.*, **2017**, 729, 978

[210] M. Samadi, M. Zirak, A. Naseri, E. Khorashadizade, A. Z. Moshfegh, *Thin Solid Films,* **2016**, 605, 2

[211] G. M. Reda, H. Fan, H. Tian, *Adv Powder Technol*, **2017**, 28, 953

[212] S. Kumar, R. Sharma, V. Sharma, G. Harith, V. Sivakumar, V. Krishnan, *Beilstein J. Nanotechnol.*, **2016**, 7, 1684

[213] A. Kumar, K. L. Reddy, S. Kumar, A. Kumar, V. Sharma, V. Krishnan, *ACS Appl. Mater. Interfaces*., **2018**, 10, 15565

[214] IUPAC, Compendium of Chemical Terminology, **1997** - Online corrected version: (2006–) "transition element"

[215] F. Cotton, G. Wilkinson, C. Murillo, M. Bochmann, Advanced inorganic chemistry, John Wiley & Sons **1999**

[216] C. N. R. Rao, *Annu Rev Phys Chem*, **1989**, 40, 291

[217] D. Sun, L. He, Y. Lai, J. Lian, J. Sun, A. Xie, B. Lin, *Materials*, **2018**, 11, 1987

[218] G. Bantsis, M. Betsiou, A. Bourliva, T. Yioultsis, C. Sikalidis, *Ceram. Int.*, **2012**, 38, 721

[219] J. Ding, T. Fan, D. Zhang, K. Saito, Q. Guo, *Solid State Commun*, **2011**, 151, 802

[220] Z. Liu, T. Fan, W. Zhang, D. Zhang, *Microporous Mesoporous Mater.,* **2005**, 85, 82

[221] Z. Liu, T. Fan, J. Gu, D. Zhang, X. Gong, Q. Guo, J. Xu, *Mater Trans*, **2007**, 48, 878

[222] Y. Zhu, Z. Zhu, Y. Chen, F. Yang, H. Qin, L. Xie, *Water Air Soil Pollut.,* **2013**, 224, 1589

[223] Z. Zhu, H. Zeng, Y. Zhu, F. Yang, H. Zhu, H. Qin, W. Wei, *Sep. Purif. Technol.*, **2013**, 117, 124

[224] Z. Q. Zhu, Y. N. Zhu, H. Qin, Y. H. Li, Y. P. Liang, H. Deng, H. L. Liu, *Mater. Manuf. Process*., 2015, 30, 285

[225] N. Adachi, M. Kuwahara, C. K. Sia, T. Ota, *Materials,* **2009**, 2, 1923

[226] R. Li, Z. Shu, L. Qian, L. Zhou, Y. Liu, S. Liu, *Bioresources*, **2016**, 11, 3937

[227] Y. Pu, H. Zo, J.-X. Wang, J. Zhai, N. R. Foster, J.-F. Chen, *Mater. Lett*., **2011**, 65, 2213

[228] C. K. Sia, Y. Sasaki, N. Adachi, T. Ota, *J. Ceram. Soc. JAPAN*, **2009**, 117, 958

[229] M. Zhang, X.-F. Zhang, Z.-P. Deng, L.-H. Huo, S. Gao, *Mater. Lett*., **2018**, 223, 61

[230] C. Chang, C. Zhang, W. Wang, Q. Li, *Rare Metals*, **2010**, 29, 501

[231] V. I. Mikhailov, E. F. Krivoshapkina, Y. I. Ryabkov, P. V. Krivoshapkin, *Glass Phys. Chem.*, **2016**, 42, 582

[232] K. Li, H. Chen, F. Shua, D. Xue, X. Guo, *RSC Adv.*, **2014**, 4, 36507

[233] R. Purbia, S. Paria, *J. Colloid Interface Sci.*, **2018**, 511, 463

[234] P. Song, Q. Wang, Z. Zhang, Z. Yang, *Sens. Actuators B Chem.,* **2010**, 147, 248

[235] P. Song, H. Zhang, D. Han, J. Li, Z. Yang, Q. Wang, *Sens. Actuators B Chem.,* **2014**, 196,140

[236] B. Palas, G. Ersöz, S. Atalay, *Ecotoxicol. Environ. Saf.*, **2019**, 182, 109367

[237] W. B. Goodwin, I. J. Gomez, Y. Fang, J. C. Meredith, K. H. Sandhage, *Chem. Mater.,* **2013**, 25, 4529

[238] L. Lu, J. Li, J. Yu, P. Song, D. H. L. Ng, *Chem. Eng. J.*, 2016, 283, 524

[239] Z. Liu, T. Fan, D. Zhang, *J. Am. Ceram. Soc.*, **2006**, 89, 662

[240] R. Wang, Q. Li, D. Xie, H. Xiao, H. Lu, *Appl. Surf. Sci.,* **2013**, 279, 129

[241] M. Airimioaei, V. A. Lukacs, I. Lisiecki, P. Beaunier, J. Blanchard, D. Lutic, S. Tascu, P. Postolache, C. E. Ciomaga, M. Olariu, L. Mitoseriu, *J. Alloys Compd.,* **2020**, 816, 152543

[242] L. J. Xie, W. Chu, Y. Y. Huang, D. G. Tong, *Mater. Lett.*, **2011**, 65, 153

[243] Y. Zheng, Y. Li, J. Yao, Y. Huang, S. Xiao, *Ceram. Int.*, **2018**, 44, 2568

[244] K. Gao, S.-D. Li, *J. Alloys Compd.,* 2020, 832, 154927

[245] S. Wang, W. Li, L. Xin, M. Wu, W. Sun, X. Lou, *Chem. Eng. J.,* **2017**, 321, 546

[246] K. Tian, X.-X. Wang, H.-Y. Li, R. Nadimicherla, X. Guo, *Sens. Actuators B Chem.,* **2016**, 227, 554

[247] M. Yu, G. Moon, E. Bill, H. Tüysüz, *ACS Appl. Energy Mater*., **2019**, 2, 1199

[248] Y. Liu, B. Lv, P. Li, Y. Chen, B. Gao, B. Lin, *Mater. Lett.*, **2018**, 210, 231

[249] D. Yan, Y. Zhang, X. Zhang, Z. Yu, Y. Zhao, G. Zhu, G. Chen, C. Ma, H. Xu, A. Yu, *Ceram. Int.*, **2017**, 43 9235

[250] D. Sun, L. He, R. Chen, Y. Liu, B. Lv, S. Lin, B. Lin, *Appl. Surf. Sci.,* **2019**, 465, 232

[251] L. Han, D.-P. Yang, A. Liu, *Biosens. Bioelectron.*, **2015**, 63, 145

[252] M. J. K. Reddy, S. H. Ryu, A.M. Shanmugharaj, *Electrochim. Acta,* **2016**, 189, 237

[253] J. Yang, M. Wang, S. Zhao, Y. Liu, W. Zhang, B. Wu, Q. Liu, *Int. J. Hydrog. Energy*, **2019**, 44, 870

[254] C. B. Ojeda, F. S. Rojas, J. M. C. Pavón, *J. Wood Chem. Technol.*, **2010**, 30, 140

[255] A. O. Turakulova, N. V. Zaletova, G. P. Murav'eva, M. V. Burova, V. V. Lunin, *Russ. J. Phys. Chem. A*, **2008**, 82, 1403

[256] T. P. Otroshchenko, A. O. Turakulova, E. S. Lokteva, E. V. Golubina, V. V. Lunin, *Russ. J. Phys. Chem. A*, **2015**, 89, 1163

[257] C. R. Rambo, J. Cao, H. Sieber, *Mater. Chem. Phys.,* **2004**, 87, 345

[258] M. Biswas, S. Bandyopadhyay, *Mater. Lett.*, **2013**, 101, 13

[259] T. Wang, Q. Yu, J. Kong, *Int. J. Appl. Ceram. Technol.,* **2018**, 15, 472

[260] J. Zhao, S. Ge, L. Liu, Q. Shao, X. Mai, C. X. Zhao, L. Hao, T. Wu, Z. Yu, Z. Guo, *Ind. Eng. Chem. Res.,* **2018**, 57, 231

[261] Y. Bo, B. Huang, Y. Zhang, J. Wang, W. M. Lau, Z. Zheng, *Powder Technol.,* **2014**, 264, 396

[262] G. Chen, X. Yang, K. Miao, M. Long, W. Deng, *Mater. Lett.*, **2017**, 194, 193

[263] N. Duan, Q. Li, J. Liu, H. Xiao, *Can. J. Chem. Eng.,* **2015**, 93, 2015

[264] X. Li, T. Fan, Z. Liu, J. Ding, Q. Guo, D. Zhang, *J. Eur. Ceram. Soc.,* **2006**, 26, 3657

[265] H. Peng, H. Fan, L. Ning, W. Wang, J. Sui, *J. Electroanal. Chem.,* **2019**, 843, 54

[266] D. Yan, S. Li, G. Zhu, Z. Wang, H. Xu, A. Yu, *Mater. Lett.*, **2013**, 95, 164

[267] L. Meng, Z. Zhao, M. Zhang, X. Zhu, X. Geng, J. Liu, Y. Xia, Z. Wang, *Ceram. Int.*, **2017**, 43, 7048

[268] Z. Cui, J. Liu, D. Zeng, H. Liu, C. Xie, *J. Am. Ceram. Soc.*, **2010**, 93, 1479

[269] X.-X. Wang, K. Tian, H.-Y. Li, Z.-X. Cai, X. Guo, *RSC Adv.*, **2015**, 5, 29428

[270] S. Alghool, H. F. A. El-Halim, A. M. Mostafa, *J Inorg Organomet Polym Mater,* **2019**, 29, 1324

[271] H. Zhang, X. Han, R. Gan, Z. Guo, Y. Ni, L. Zhang, *Appl. Surf. Sci.*, **2020**, 511, 145527

[272] T. Fanw, X. Li, Z. Liu, J. Gu, D. Zhang, *J. Am. Ceram. Soc.*, **2006**, 89, 3511

[273] D. Van Opdenbosch, M. H. Kostova, S. Gruber, S. Krolikowski, P. Greil, C. Zollfrank, *Wood Sci. Technol.,* **2010**, 44, 547

[274] P. Simon, Y. Gogotsi, Nat. Mater., **2008**, 7, 845

[275] K. Zaghib, A. Mauger, C. M. Julien, Rechargeable Lithium Batteries from Fundamentals to Applications, Elsevier, **2015**

[276] M. Forghani, S.W. Donne, *J. Electrochem. Soc.,* **2018**, 165, A664

[277] L. Zhou, C. Li, X. Liu, Y. Zhu, Y. Wu, T. van Ree, Metal Oxides in Energy Technologies, Elsevier, **2018**

[278] B. K. Kim, S. Sy, A. Yu, J. Zhang, Handbook of Clean Energy Systems, John Wiley & Sons, **2015**

[279] U. Gulzar, S. Goriparti, E. Miele, T. Li, G. Maidecchi, A. Toma, F. De Angelis, C. Capiglia, R. Proietti Zaccaria, *J. Mater. Chem. A*, **2016**, 4, 16771

[280] N. N. Greenwood, A. Earnshaw, Chemistry of the Elements, Oxford: Pergamon Press., **1984**

[281] D. F. Untereker, C. l. Schmidt, G.Jain, P. A. Tamirisa, J. Hossick-Schott, M. Viste, Clinical Cardiac Pacing, Defibrillation and Resynchronization Therapy, Elsevier, **2017**

[282] L. Hou, C. Yuan, L. Yang, L. Shen, F. Zhang, X. Zhang, *RSC Adv.,* **2011**, 1, 1521

[283] X. Xiao, X. Liu, H. Zhao, D. Chen, F. Liu, J. Xiang, Z. Hu, Y. Li, *Adv. Mater.,* **2012**, 24, 5762

[284] L. Feng, Y. Zhu, H. Ding, C. Ni, *J. Power Sources,* **2014**, 267, 430

[285] L. Yu, L. Zhang, H.B. Wu, X.W.D. Lou, *Angew. Chem. Int. Ed.*, **2014**, 53, 3711

[286] C. Zhang, L. Qian, K. Zhang, S. Yuan, J. Xiao, S. Wang, *J. Mater. Chem. A*, **2015**, 3, 10519

[287] X. Sun, G. Wang, J.-Y. Hwangb, J. Lian, *J. Mater. Chem.*, **2011**, 21, 16581

[288] W. Ji, J. Ji, X. Cui, J. Chen, D. Liu, H. Deng, Q. Fu, ChemComm, **2015**, 51, 7669

[289] Q. Wang, D.-A. Zhang, Q. Wang, J. Sun, L.-L. Xing, X.-Y. Xue, *Electrochim. Acta*, **2014**, 146, 411

[290] W.-M. Zhang, X.-L. Wu, J.-S. Hu, Y.-G. Guo, L.-J. Wan, *Adv. Funct. Mater.,* **2008**, 18, 3941

[291] S. Ni, X. Lv, J. Ma, X. Yang, L. Zhang, *J. Power Sources,* **2014**, 270, 564

[292] X. H. Huang, J. P. Tu, B. Zhang, C. Q. Zhang, Y. Li, Y. F. Yuan, H. M. Wu, *J. Power Sources*, **2006**, 161, 541

[293] H. Liu, G. Wang, J. Liu, S. Qiao, H. Ahn, *J. Mater. Chem.*, **2011**, 21, 3046

[294] X. Yan, X. Tong, J. Wang, C. Gong, M. Zhang, L. Liang, *J. Alloys Compd.,* **2013**, 556, 56

[295] F. Cao, G. X. Pan, P. S. Tang, H. F. Chen, *Mater. Res. Bull.,* **2013**, 48, 1178

[296] V. Aravindan, P. S. Kumar, J. Sundaramurthy, W. C. Ling, S. Ramakrishna, S. Madhavi, *J. Power Sources,* **2013**, 227, 284

[297] Y. B. Mollamahale, Z. Liu, Y. Zhen, Z. Q. Tian, D. Hosseini, L. Chen, P. K. Shen, *Int. J. Hydrog. Energy,* **2017**, 42, 7202

[298] M. Winker, D. Faika, H. Gulyas, R. Otterpohl, *Sci. Total Environ*., **2008**, 399, 96

[299] A. Sangion, P. Gramatica, *Environ. Int.*, **2016**, 95, 131

[300] D. W. Kolpin, E. T. Furlong, M. T. Meyer, E. M. Thurman, S. D. Zaugg, L. B. Barber, H. T. Buxton, *Environ. Sci. Technol.*, **2002**, 36, 1202

[301] P. H. Roberts, K. V. Thomas, *Sci. Total Environ.*, **2006**, 356, 143

[302] J. J. Xu, B. S. Hendriks, J. Zhao, D. Graaf, *FEBS Lett.*, **2008**, 582, 1276

[303] F. Regoli, M. E. Giuliani, *Mar. Environ. Res.*, **2014**, 93, 106

[304] L. Hua, H. Ma, L. Zhang, *Chemosphere*, **2013**, 90, 143

[305] M. Mittal, M. Sharma, O. P. Pandey, *Sol Energy*, **2014**, 110, 386

[306] A. Nezamzadeh-Ejhieh, M. Amiri, *Powder Technol.*, **2013**, 235, 279

[307] B. Palas, G. Ersöz, S. Atalay, *Chemosphere*, **2018**, 209, 823

[308] L.A. Ioannou, D. Fatta-Kassinos, *J. Environ. Chem. Eng.*, **2013**, 1, 703

[309] G. Bauer, V. Güther, H. Hess, A. Otto, O. Roidl, H. Roller, S. Sattelberger, Ullmann's Encyclopedia of Industrial Chemistry, Wiley-VCH, **2005**

[310] D. Li, C. Tong, W. Ji, Z. Fu, Z. Wan, Q. Huang, Y. Ming, A. Mei, Y. Hu, Y. Rong, H. Han, *ACS Sustain. Chem. Eng.*, **2018**, 7, 2619

[311] A. K. Prasad, S. Dhara, S. Dash, *Sens. Lett.*, **2017**, 15, 552

[312] T. Aditya, A. Pal, T. Pal, *Chem. Commun.,* **2015**, 51, 9410

[313] M. N. Nadagouda, A. B. Castle, R. C. Murdock, M. Hussain, R. S. Varma, *Green Chem.,* **2010***,* 12, 114

[314] M. N. Nadagouda, R. S. Varma, *Green Chem.*, **2008**, 10, 859

[315] https://en.wikipedia.org/wiki/Post-transition_metal - Last update July 2020

[316] S.-J. Park, M.-K. Seo, Interface Science and Technology, Elsevier, **2011**

[317] K. Ishikawa, S. Matsuya, Y. Miyamoto, K. Kawate, Comprehensive Structural Integrity, Elsevier, **2003**

[318] Y. Liu, S. Wang, Q. Fan, Y. Liu, W. Zhou, *Desalination Water Treat.*, **2017**, 100, 67

[319] S. R. Balaji, B. K. Mandal, *Asian J Chem*, **2017**, 29, 2459

[320] Y. L. Botero, J. E. López-Rendón, D. Ramírez, D. M. Zapata, F. Jaramillo, *Minerals*, **2020**, 118

[321] P. Sikora, A. Augustyniak, K. Cendrowski, P. Nawrotek, E. Mijowska, *Nanomaterials*, **2018**, 212

[322] G. Ma, Z. Ma, Z. Zhang, Z. Yang, Z. Lei, *J. Porous Mater.,* **2012**, 19, 597

[323] S. H. Babu, S. Kaleemulla, N. M. Rao, C. Krishnamoorthi, *J. Magn. Magn. Mater.*, **2016**, 416, 66

[324] O. Bierwagen, *Semicond Sci Technol,* **2015***,* 30, 024001

[325] E. Fortunato, D. Ginley, H. Hosono, D.C. Paine, *MRS Bulletin*., **2007**, 32, 242

[326] H. Ohno, *Nat. Mater*., **2010**, 9, 952

[327] C. Li, D. Zhang, X. Liu, S. Han, T. Tang, J. Han, C. Zhou, *Appl. Phys. Lett.*, **2003**, 82, 1613

[328] M. Batzill, U. Diebold, *Prog. Surf. Sci.,* **2005**, 79, 47

[329] J. Savioli, A. L. Gavin, A. K. Lucid, G. W. Watson, Tin Oxide Materials, Elsevier, **2020**

[330] J. Lin, Z. Peng, C. Xiang, G. Ruan, Z. Yan, D. Natelson, J. M. Tour, *ACS Nano,* **2013**, 7, 6001

[331] S. Das, V. Jayaraman, *Prog. Mater. Sci.*, **2014**, 66, 112

[332] Q. Wali, A. Fakharuddin, R. Jose, *J. Power Sources*, **2015**, 293, 1039

[333] C.R. Rambo, H. Sieber, *Adv. Mater*., **2005**, 17, 1088

[334] C. R. Rambo, T. Andrade, T. Fey, H. Sieber, A. E. Martinelli, P. Greil, *J. Am. Ceram. Soc*., **2008**, 91, 852

[335] M. H. Kostova, C. Zollfrank, M. Batentschuk, F. Goetz-Neunhoeffer, A. Winnacker, P. Greil, *Adv. Funct. Mater.*, **2009**, 19, 599

[336] M. Patel, B. K. Padhi, *J. Mater. Sci.*, **1990**, 25, 1335

[337] T. Delbrücke, R. A. Gouvêa, M. L. Moreira, C. W. Raubach, J. A. Varela, E. Longo, M. R. F. Goncalves, S. Cava, *J. Eur. Ceram. Soc.,* **2013**, 33, 1087

[338] T. Fan, B. Sun, J. Gu, D. Zhang, L. W. M. Lau, *Scr. Mater.,* **2005**, 53, 893

[339] T. Zhang, Y. Zhou, X. Bu, Y. Wang, M. Zhang, J. Hu, *Ceram. Int.*, **2014**, 40, 13703

[340] T. Fan, X. Li, J. Ding, D. Zhang, Q. Guo, *Microporous Mesoporous Mater.,* **2008**, 108, 204

[341] V. I. Mikhailov, E. F. Krivoshapkina, V. A. Demina, E. M. Tropnikov, P. V. Krivoshapkin, *Russ. J. Gen. Chem.*, **2016**, 86, 213

[342] T. Zhang, Y. Zhou, M. He, X. Bu, Y. Wang, C. Zhang, *J. Eur. Ceram. Soc.,* **2015**, 35, 1337

[343] Y. Wang, Q. Wei, Y. Huang, *Mater. Lett.*, **2015**, 157, 67

[344] J. Ma, H. Fan, H. Tian, X. Ren, C. Wang, S. Gao, W. Wang, *Sens. Actuators B Chem.*, **2018**, 262, 17

[345] P. Song, Q. Wang, Z. Yang, *Sens. Actuators B Chem.,* **2012**, 168, 421

[346] P. Hu, H. Wang, Q. Zhang, Y. Li, *J. Phys. Chem. C*, **2012**, 116, 10708

[347] E. M. Jin, J.-Y. Park, H.-B. Gu, S. M. Jeong, *Mater. Lett.*, **2015**, 159, 321

[348] B. Sun, T. Fan, J. Xu, D. Zhang, *Mater. Lett.*, **2005**, 59, 2325

[349] S. Zhu, D. Zhang, J. Gu, J. Xu, J. Dong, J. Li, *J Nanopart Res,* **2010**, 12, 1389

[350] P. Song, Q. Wang, Z. Yang, *Sens. Actuators B Chem.,* **2011**, 156, 983

[351] A. Ahamed Fazil, J. Udaya Bhanu, A. Amutha, S. Joicy, N. Ponpandian, S. Amirthapandian, B. K. Panigrahi, P. Thangadurai, *Microporous Mesoporous Mater.,* **2015**, 212, 91

[352] F. Song, H. Su, J. Han, W. M. Lau, W.-J. Moon, D. Zhang, *J. Phys. Chem. C*, **2012**, 116, 10274

[353] G. Xu, X. Zhang, H. Cui, Z. Chen, J. Ding, X. Zhan, *Powder Technol.,* **2016**, 302, 283

[354] M. Ahn, K. Park, J. Heo, J. Park, D. Kim, K. J. Choi, J. Lee, S. Hong, *Appl. Phys. Lett*., **2008**, 26, 263103

[355] O. Regan, M. Grätzel, *Nature*, **1991**, 353, 737

[356] M. Lv, D. Zheng, M. Ye, J. Xiao, W. Guo, Y. Lai, L. Sun, C. Lin, J. Zuo, *Energy Environ. Sci.,* **2013**, 6, 1615

[357] M. Ye, J. Gong, Y. Lai, C. Lin, Z. Lin, *J. Am. Chem. Soc*., **2012**, 134, 15720

[358] P. Roy, D. Kim, K. Lee, E. Spiecker, P. Schmuki, *Nanoscale*, **2010**, 2, 45

[359] K. J. Hwang, D. C. Kang, S. Lee, C. H. Hwang, C. Kim, N. Kim, S. Jin, I. H. Lee, J. Y. Park, *Mater. Lett.,* **2014**, 115, 265

[360] G.L Miessler, D.A. Tarr, Chimica Inorganica, Quarta edizione, Piccin, **2011**

[361] A. A. Pilarska, Ł. Klapiszewski, T. Jesionowski, *Powder Technol.,* **2017**, 319, 373

[362] H. Hattori, Y. Ono, Metal Oxides in Heterogeneous Catalysis, Elsevier, **2018**

[363] L. Sharma, R. Kakkar, *CrystEngComm*, **2017**, 19, 6913

[364] C. G. Kumar, S. Pombala, Y. Poornachandra, S. V. Agarwal, Nanobiomaterials in Antimicrobial Therapy: Applications of Nanobiomaterials, Elsevier, **2016**

[365] A. Al-Tabbaa, Woodhead Publishing Series in Civil and Structural Engineering, Elsevier, **2013**

[366] M. Kenny, T. Oates, Ullmann's Encyclopedia of Industrial Chemistry, Wiley, **2007**

[367] I. B. Banković–Ilić, M. R. Miladinović, O. S. Stamenković, V. B. Veljković, *Renew. Sust. Energ. Rev*., 2017, 72, 746

[368] D. M. Marinković, M. V. Stanković, A. V. Veličković, J. M. Avramović, M. R. Miladinović, O. O. Stamenković, V. B. Veljković, D. M. Jovanović, *Renew. Sust. Energ. Rev*., **2016**, 56, 1387

[369] Y. Hu, H. Lu, Wenqiang Liu, Y. Yang, H. Li, *Chem. Eng. J.,* **2020**, 396, 125253

[370] H. Sun, C. Wu, B. Shen, X. Zhang, Y. Zhang, J. Huang, *Mater. Today Sustain.,* **2018**, 1, 1

[371] D. Dvorsky, J. Kubasek, D. Vojtěch, *Manuf Technol*, **2015**, 15, 969

[372] A. Fihri, C. Len, R. S. Varma, A. Solhy, *Coord Chem Rev,* **2017**, 347, 48

[373] S. Klaithong, D. Van Opdenbosch, C. Zollfrank, J. Plank, *Z. Naturforsch*., **2013**, 68, 533

[374] S. Wei, R. Han, Y. Su, J. Gao, G. Zhao, Y. Qin, *Energy Fuels*, **2019**, 33, 5398

[375] C. Chi, Y. Li, W. Zhang, Z. Wang, *Appl. Energy,* **2019**, 251, 113382

[376] D. Zhang, M. Wang, G.-J. Ren, E.-J. Song, *Mater. Sci. Eng. C,* **2013**, 33, 4677

[377] D. Zhang, S.-Y. Liu, X. Song, Z.-Y. Xu, B. Yang, L.-Y. Chen, Y.-C. Tan, F.-J. Li, *J. Adv. Oxid. Technol.,* **2016***,* 19, 9

[378] G.-Y. Hou, Z.-H. Jin, J.-M. Qian, G.-Q. Zheng, *Mater. Sci. Forum,* **2012**, 724, 378

[379] J. Qian, Y. Kang, W. Zhang, Z. Li, *J Mater Sci Mater Med,* **2008**, 19, 3373

[380] A. Ruffini, S. Sprio, A. Tampieri, *Chem. Eng. J.,* **2013**, 217, 150

[381] A. Tampieri, S. Sprio, A. Ruffini, G. Celotti, I. G. Lesci, N. Roveri, *J. Mater. Chem.*, **2009**, 19, 4973

[382] A. Tampieri, A. Ruffini, A. Ballardini, M. Montesi, S. Panseri, F. Salamanna, M. Fini, S. Sprio, *Biomater. Sci.*, **2019**, 7, 307

[383] C. Xing, S. Ge, B. Huang, Y. Bo, D. Zhang, Z. Zheng, *Mater. Res. Bull.,* **2012**, 47, 1572

[384] R.-Q. Sun, L.-B. Sun, Y. Chun, Q.-H. Xu, H. Wu, *Microporous Mesoporous Mater.,* **2008**, 111, 314

[385] D. Yang, T. Fan, D. Zhang, J. Zhu, Y. Wang, B. Du, Y. Yan, *Chem. -Eur. J.*, **2013**, 19, 4742

[386] S. Ishii, M. J. Sadowsky, *Microbes Environ.*, **2008**, 23, 101

[387] L. Huang, D. Li, D. Evans, *Eur. Phys. J. D*, **2005**, 34, 321

[388] B. Wang, X. Xiong, H. Renab, Z. Y. Huang, *RSC Adv.*, **2017**, 7, 43464

[389] W. Liu, H. An, C. Qin, J. Yin, G. Wang, B. Feng, M. Xu, *Energy Fuels*, **2012**, 26, 2751

[390] B. Mysen, P. Richet, Silicate Glasses and Melts, Elsevier, **2019**

[391] F. W. Clarke, H. S. Washington, United States geological survey, **1924**, 127

[392] I. A. Rahman, V. Padavettan, *J. Nanomater.,* **2012**, 2012, 132424

[393] P. G. Jeelani, P. Mulay, R. Venkat, C. Ramalingam, *Silicon*, **2020**, 12, 1337

[394] Y. Feng, N. Panwar, D. J. H. Tng, S. C. Tjin, K. Wang, K.-T. Yong, *Coord Chem Rev,* **2016**, 319, 86

[395] B. Matovic, B. Babic, A. Egelja, A. Radosavljevic-Mihajlovic, V. Logar, A. Saponjic, S. Boskovic, *Mater. Manuf. Process.*, **2009**, 24, 1109

[396] Y. Shin, J. Liu, J. H. Chang, Z. Nie, G. J. Exarhos, *Adv. Mater.*, **2001**, 13, 728

[397] Y. Shin, G. J. Exarhos, *Cellulose*, **2007**, 14, 269

[398] Q. Lu, Z. Chen, F. Chen, X. Huang, Z. Wu, *Asian J Chem*, **2014**, 26, 1394

[399] S. R. Hall, H. Bolger, S. Mann, *Chem. Commun.*, **2003**, 2784

[400] L. Yue, J. Guo, Q. Yang, X. Luo, J. Lian, J. Yang, L. Wang, *Mater. Lett.*, **2015**, 157, 225

[401] K. Zheng, J. A. Bortuzzo, Y. Liu, W. Li, M. Pischetsrieder, J. Roether, M. Lu, A. R. Boccaccini, *Colloids Surf. B*, **2015**, 135, 825

[402] J. Li, Z. Li, G. Zi, Z. Yao, Z. Luo, Y. Wang, D. Xue, B. Wang, J. Wang, *Catal Commun,* **2015**, 59, 233

[403] M. S. Bahniuk, H. Pirayesh, H. D. Singh, J. A. Nychka, L. D. Unsworth, *Biointerphases,* **2012**, 7, 41

[404] S. Romeis, A. Hoppe, C. Eisermann, N. Schneider, A. R. Boccaccini, J. Schmidt, W.Peukert, *J. Am. Ceram. Soc.*, **2014**, 97, 150

[405] C. C. C. R. de Carvalho, M. M. R. da Fonseca, *Food Chem.*, **2006**, 95, 3, 413

[406] P. A. Robles-Dutenhefner, B. B. N. S. Brandão, L. F. de Sousa, E. V. Gusevskaya, *Appl. Catal. A Gen.*, **2011**, 399, 172